



ESCOLA DE ENGENHARIA
DEPARTAMENTO DE ENGENHARIA NUCLEAR
PROGRAMA DE PÓS-GRADUAÇÃO EM CIÊNCIAS E TÉCNICAS
NUCLEARES
UNIVERSIDADE FEDERAL DE MINAS GERAIS

Baljeet Seniwal

Dosimetry of Brachytherapy using Radioactive Nanoparticles: *In silico*

Belo Horizonte
May 2021

BALJEET SENIWAL

Dosimetry of Brachytherapy using Radioactive Nanoparticles:
In silico

Thesis presented to the Postgraduate Course in Nuclear Sciences and Techniques at the School of Engineering of the Federal University of Minas Gerais, as a partial requirement to obtain the title of Doctor in Nuclear Sciences and Techniques

Concentration area: Radiation Sciences

Promoter: Prof. Telma C. F. Fonseca, PhD

Co-Promoter: Prof. Jan Schuemann, PhD

Line of Research: Applications of Radiation to Biomedical Sciences

Belo Horizonte

2021

S477d Seniwal, Baljeet.
Dosimetry of brachytherapy using radioactive nanoparticles [recurso eletrônico] : in silico / Baljeet Seniwal. - 2021.
1 recurso online (xxiv, 143 f. : il., color.) : pdf.

Orientadora: Telma C. F. Fonseca.
Coorientador: Jan Schuemann.

Tese (doutorado) - Universidade Federal de Minas Gerais,
Escola de Engenharia.

Anexos: f. 112-143.

Bibliografia: f. 104-111.
Exigências do sistema: Adobe Acrobat Reader.

1. Engenharia nuclear - Teses. 2. Braquiterapia - Teses. 3. Método de Monte Carlo - Teses. I. Fonseca, Telma Cristina Ferreira. II. Schuemann, Jan. III. Universidade Federal de Minas Gerais. Escola de Engenharia. IV. Título.

CDU: 621.039(043)



UNIVERSIDADE FEDERAL DE MINAS GERAIS
PROGRAMA DE PÓS-GRADUAÇÃO EM CIÊNCIAS E TÉCNICAS NUCLEARES



FOLHA DE APROVAÇÃO

Dosimetry of Brachytherapy using Radioactive Nanoparticles: In silico

BALJEET SENIWAL

Tese submetida à Banca Examinadora designada pelo Colegiado do Programa de Pós-Graduação em CIÊNCIAS E TÉCNICAS NUCLEARES, como requisito parcial para obtenção do grau de Doutor em CIÊNCIAS E TÉCNICAS NUCLEARES, área de concentração CIÊNCIAS DAS RADIAÇÕES.

Profa. Telma Cristina Ferreira Fonseca - Orientadora (Departamento de Engenharia Nuclear - UFMG)

Dr. Jan Schuemann – Coorientador (Massachusetts General Hospital)

Prof. Tarcísio Passos Ribeiro de Campos (Departamento de Engenharia Nuclear - UFMG)

Dr. Ralph Santos Oliveira (Instituto de Engenharia Nuclear)

Dr. Bruno Melo Mendes (CDTN/CNEN)

Dr. Lucas Freitas de Freitas (Instituto de Pesquisas Energéticas e Nucleares - I)

Dr. Luc Beaulieu (Laval University)

Belo Horizonte, 10 de maio de 2021.

To my Family and my Supervisor

Acknowledgements

I am indebted to many people who helped me through this journey of Ph.D. research. Without their help, this work would never see light.

First and foremost, I would like to thank my research advisor Dr. Telma C.F. Fonseca. I would like to express my sincere gratitude for her support, advice, help, and constant encouragement that has always kept me motivated in my research work and made my Ph.D. experience productive and stimulating. Apart from work she treated me like a friend. I have no idea and no word which can express my thankfulness and the feelings of my heart for warm reception at the airport and hospitality during my stay in Brazil. She went above and beyond, and I am touched and grateful. I also appreciate that she gave me the opportunity to work on the project that I like. She is a dream PhD advisor.

I am also thankful to my research co-advisor Prof. Jan Schuemann from Massachusetts General Hospital & Harvard Medical School for giving me opportunity to work with him. Also, providing me constant guidance and feedback, which helped me to improve my research skills.

At the personal level, I would like to thank my father Laxman Seniwai, mother Savitri Seniwai, aunt Bimla, brothers Sumit, Manish, sisters Rekha and Sulekha. I am grateful to them for their endless support, encouragement, and trust. I am very grateful to my uncle Ram Chander who was always proud of me and encouraged me to pursue Ph.D. before he passed away. He wished me to get Ph.D. one day, and I hope to fulfill his wish. I am also grateful to my Brazilian family, who accepted me happily as a family member: Goreti Pereira (My mother) and Felipe Henrique (brother). I would like to express my sincere gratitude for making my stay in Brazil comfortable. This helped me to focus more on research more than other day to day problems.

Apart from research I have earned some good friends: Bruno, Jhonny, Lucas, Mazer, Lucas de Freitas, Prof. Ademar and Peter. I would like to express my sincere gratitude for their full-time availability, suggestions and positive criticism and guidance, whenever I was in need.

I am also thankful to a lot of other friends: Bruno, Mario, Mabel, Carlos, Metheus, Aline, Thales, Joao, and many more for their help and support. I am thankful for everyone who was a part of my journey from the first day of my academic study till my graduation.

I would like to thank the Coordination for the Improvement of Higher Education Personnel (CAPES) and the National Council for Scientific and Technological Development (CNPq), for financial support for my doctoral studies.

Baljeet Seniwai

"I asked him where he had it made, he said he made it himself, & when I asked him where he got his tools said he made them himself & laughing added if I had said for other people to make tools & things for me, I had never made anything....."

Sir Isaac Newton

Resumo/Abstract

Nanopartículas radioativas (radio-NPs) funcionalizadas com biomoléculas específicas do tumor, injetadas de forma intratumoral, têm sido relatadas como uma alternativa à braquiterapia à base de sementes (LDR) de baixa taxa de dose (LDR). Em tratamentos de câncer à base de radiação a estimativa precisa da dose absorvida é crucial para o controle adequado da doença e para minimizar o risco de efeitos colaterais induzidos por radiação. Atualmente, o formalismo da Dose de Radiação Interna Médica (MIRD) usado para fins de dosimetria interna não considera o impacto da absorção e lavagem de radiofarmacêuticos na fração de sobrevivência celular (FS) e estimativa de dose absorvida. A dosimetria celular única (SCD), baseada no formalismo MIRD, é geralmente usada para avaliar as características dosimétricas dos radionuclídeos para aplicações teranósticas. No entanto, existem discrepâncias nos métodos gráficos e na distribuição de energia radial, utilizadas para estimar a distribuição da dose. Além disso, a modelagem precisa do transporte de radiação no meio pelos códigos de Monte Carlo (MC) desempenha um papel fundamental na estimativa da dose absorvida. O núcleo de ponto de dose (DPK) é usado para: (i) testar a precisão de diferentes códigos de Monte Carlo (MC), realizando comparação em termos de DPK; e (ii) estimam a dose absorvida por 3D na medicina nuclear. No entanto, pelo que sabemos, não foram investigadas as diferenças de impacto na DPK na dose absorvida. Este projeto de doutorado tem como objetivo realizar a dosimetria de aplicações LDR BT, utilizando radio-NPs, e preencher as lacunas acima mencionadas na literatura usando métodos de Monte Carlo (MC). Os cálculos dosimétricos foram realizados utilizando-se dois códigos MC amplamente utilizados: Geant4-DNA e EGSnrc. Inicialmente, a comparação em termos de DPK para elétrons na faixa de energia de 1 keV a 3 MeV foram realizadas para testar a precisão de ambos os códigos. Após a validação, utilizou-se a abordagem SCD para avaliar as características dosimétricas de emissão dos radionuclídeos de 12 alfa/beta/augeter para aplicações teranósticas. Também foi proposto o conceito de função de dose radial para representação gráfica da distribuição de doses. Além disso, as curvas de sobrevivência celular publicadas na literatura foram replicadas utilizando-se o modelo matemático proposto por Sefl et al. 2016. O nosso trabalho apresenta que, tanto o Geant4-DNA quanto o EGSnrc podem simular com precisão o transporte de elétrons de baixa energia em relação a outros códigos MC. Além disso, as maiores diferenças entre as DPKs foram encontradas para energias eletrônicas abaixo de 10 keV, o que resultou na distribuição de dose homogênea em micrômetros e sem impacto em voxels em tamanhos milimétricos. Os emissores alfas foram encontrados para depositar a dose mais alta absorvida em comparação com os emissores augeter e beta. Além disso, replicamos efetivamente as curvas de sobrevivência celular publicadas na literatura sobre o uso de radio-NPs para aplicações LDR BT. Concluiu-se que a precisão dos códigos MC e parâmetros MC deve ser validada e referenciada antes de usá-los para fins de dosimetria. Além disso, o conhecimento preciso da taxa de absorção, taxa de lavagem de NPs, radio-sensibilidade e taxa de repopulação de tumores é importante para o cálculo das curvas de sobrevivência celular.

Keywords: Braquiterapia LDR, nanopartículas radioativas, núcleos de ponto de dose, métodos de Monte Carlo.

Resumo/Abstract

Radioactive nanoparticles (radio-NPs) functionalized with tumor specific biomolecules, injected intratumorally, have been reported as an alternative to low dose rate (LDR) seed based brachytherapy (BT). In radiation based cancer treatments accurate estimation of absorbed dose is crucial for proper disease control and to minimize the risk of radiation induced side effects. Currently, used Medical Internal Radiation Dose (MIRD) formalism for internal dosimetry purposes do not consider the impact of uptake and washout of radiopharmaceutical on the cell survival fraction (SF) and absorbed dose estimation. The single cell dosimetry (SCD), based on MIRD formalism, is generally used to evaluate the dosimetric characteristics of radionuclides for theranostic applications. However, there exists discrepancies in the graphical methods and radial energy distribution, used to estimate the dose distribution. Moreover, precise modeling of radiation transport in the medium by Monte Carlo (MC) codes plays a pivotal role in the estimation of absorbed dose. The dose point kernel (DPK) are used to: (i) test the accuracy of different Monte Carlo (MC) codes, by performing comparison in terms of DPK; and (ii) estimate 3D-absorbed dose in nuclear medicine. However, as per our knowledge the impact differences in DPK on absorbed dose was not investigated. This PhD project aims to perform dosimetry of LDR BT applications, using radio-NPs, and fill the above mentioned gaps in literature using MC methods. The dosimetric calculations were performed using two widely used MC codes: Geant4-DNA and EGSnrc. Initially, the comparison in terms of DPK for electrons in energy range of 1 keV to 3 MeV was made to test the accuracy of both codes. After validation, SCD approach was used to evaluate the dosimetric characteristics of 12 alpha/beta/auget emitting radionuclides for theranostic applications. The concept of radial dose function was also proposed for graphical representation of dose distribution. Further, the cell survival curves published in literature were replicated using the mathematical model proposed by Seftl et al. 2016. Our findings show that, both Geant4-DNA and EGSnrc can accurately simulate the transport of low energy electrons with respect to other MC codes. Moreover, the largest differences between DPKs were found for electron energies below 10 keV, which resulted in inhomogeneous dose distribution in micrometer and no impact on millimeter sized voxels. The alpha emitters were found to deposit highest absorbed dose in comparison to auger and beta emitters. Furthermore, we effectively replicated the cell survival curves published in literature on the use of radio-NPs for LDR BT applications. It was concluded that the accuracy of the MC codes and MC parameters must be validated and benchmarked before using them for dosimetry purposes. Also, the accurate knowledge of uptake rate, washout rate of NPs, radio-sensitivity and tumour repopulation rate is important for the calculation of cell survival curves.

Keywords: LDR brachytherapy, Radioactive nanoparticles, Dose point kernels, Monte Carlo methods.

List of Figures

1.1	The schematic representation of the basic principles on delivery the radio-pharmaceutical in the tumor volume in TRT applications. Source: Author.	2
1.2	Comparison between: (i) Radioactive Brachytherapy seeds and (ii) Au-198 radioactive nanoparticles (NPs) functionalized with Mangiferin (MGF) in terms of tumor penetration and distribution within the tumor. Source: Katti et al. Journal of Radioanalytical and Nuclear Chemistry 318.3 (2018): 1737-1747.	4
1.3	(A) Dose point kernels estimated using several Monte Carlo codes for 10 keV monoenergetic electron source by Champion et al. 2014. (B) Radial energy deposition curve for radioactivity (I-123) uniformly distributed within the nucleus for single cell dosimetry by Fourie et al. 2015 (C) Tumor volume follow-up for in- <i>vivo</i> study performed for treatment of PC3 xenograft tumors using Pd-103 radioactive nanoparticles by L-Pelletier et al. 2017.	8
2.1	A) Water shells immersed in a water sphere, the scoring was done within the shells. The maximum radius of the water spheres was set to $1.5R_{CSDA}$. B) Zoom view of the center of the water shells; S1, S2, S3, S4... Si are the numbers of the shells; T is the shell thickness ($T = 0.025R_{CSDA}$); R is the outer radius of a shell ($R = Si \cdot (0.025R_{CSDA})$); r is the inner radius of a shell ($r = (Si - 1) \cdot (0.025R_{CSDA})$); r_m is the mean radius of a shell ($r_m = ((R+r)/2)$). C) MCNP Visited view of the isotropic, point and mono-energetic 50 keV electron source tracks.	19
2.2	Water-equivalent phantom for 3D dosimetry at microscopic scale by kernel convolution. Active voxels (uniformly activated) are highlighted. YZ 2D slice (top) and XY centered z-plot (bottom) are presented.	22
2.3	Activity distribution transverse (left) and longitudinal (right) slices within the calibration phantom used for 3D dosimetry at macroscopic scale by kernel convolution.	23

2.4	In-water range (R) (A) for different energies as calculated by EGSnrc, FLUKA, GEANT4-DNA, MCNP6 and PENELOPE(2014), along with NIST reference values. Figure (B) reports the range relative to NIST for all MC codes.	27
2.5	In-water R_{50} (A, B) R_{90} (C, D) and Ratio (with respect to PENELOPE) for different electron energies calculated using EGSnrc, FLUKA, GEANT-DNA, MCNP6 and PENELOPE.	29
2.6	1 keV (A), 5 keV(B), 10 keV (C) and 25 keV(D) in-water sDPK obtained with different PENELOPE, GEANT4-DNA, EGSnrc, FLUKA and MCNP6 Monte Carlo codes.	31
2.7	50 keV in-water sDPK obtained with PENELOPE, GEANT4-DNA, EGSnrc, FLUKA and MCNP6 MC codes.	32
2.8	Representative example of voxelized 3D kernel \mathbf{K} as obtained in terms of 50 keV sDPK for PENELOPE code.	33
2.9	Absorbed dose rate profiles obtained by the different MC codes for 5 (A), 10 (B), 25 (C) and 50 keV (D).	33
2.10	Absorbed dose rate profiles obtained by the different MC codes for 50, 25, 10 and 5 keV.	34
3.1	Geometric model for the simulation. A water sphere composed of multiple shells, varying in radius, where DPK is calculated.	41
3.2	DPK curves for monoenergetic electron point sources of: a) 0.05, b) 0.1; c) 0.5; d) 1 and e) 3 MeV. The gray area comprises $\pm 3\%$ of the EGSnrc curves.	46
3.3	Fluence curves for monoenergetic electron point sources of: a) 0.05 MeV; b) 0.1 MeV; c) 0.5 MeV; d) 1 MeV; and e) 3 MeV	48
3.4	DPK curves obtained with different codes for 6 radionuclides: a) Lu-177, b) I-131, c) Sm-153, d) Sr-89, e) Ho-166 and f) Y-90.	49
4.1	Cell geometry used for S-value and radial energy profile calculations, where the cell and nucleus radii are $5.0\mu m$ and $4.0\mu m$, respectively.	60
4.2	Energy deposited per decay (keV) along the radius of cell (μm), when I-123 radionuclide is sampled uniformly in nucleus (Red) and cytoplasm (Blue) compared with Fourie et al. 2015	66

4.3	Energy deposited per decay along the radius of the cell, normalized to the square of radius, when (a) Auger emitting radioisotope (I-123, In-111 and Ga-67); (b) Low energy β -emitting radioisotope (Er-169 and Lu-177); (c) Medium energy β -emitting radioisotope (Re-186, Sm-153) and (d) High energy β -emitting radioisotope (Y-90, Sr-89) are sampled uniformly within the nucleus or cytoplasm.	67
5.1	Main approaches for cancer treatment using nanomaterials and radiation. Nanomaterials, i.e. polymer nanoparticles, mycelles, carbon nanotubes, metal nanoparticles, and liposomes can be radiolabeled or made radioactive and act as therapeutic or diagnostic tools in radio-immunotherapy and in nanobrachytherapy, it can also enhance the effects of radiation via radiosensitization.	72
5.2	Comparison between calculated (A) tumor volume and L-Pelletier et al., 2018, (B) cell survival curve and Wang et al., 2020, (C) tumor volume and Katti et al., 2018, (D) expected cell survival curve for Katti et al., 2018. . .	83
5.3	Comparison of radiation therapeutic efficiency of Pd-103, Sm-153, and Au-198 NPs (A, B, C) considers constant tumor volume of 0.3cc and administered radioactivity of 20, 40, 60MBq.	86
5.4	Comparison of radiation therapeutic efficiency of Pd-103 considering administered radioactivity of (A) 60MBq to tumor volume, PC-3 cell lines, of 0.3, 0.6 and 1.0 cc (B) 600 MBq to constant tumor volume of 0.6cc of two different cell lines PC-3 and B16F10.	87
B.1	$G(e_{aq}^{-1})$ and $G(H^{\bullet})$ as a function of time generated first 10 keV of 1 MeV electron source in water with [GSH] of 0, 1, 10 mM.	134
B.2	$G(HO_2^{\bullet} + O_2^{-})$ as a function of partial pressure of O_2 in air as a function of time generated from first 10 keV of 1 MeV electron source in water: (A) at 1 μs , (B) at 10 μs , and (C) at 10 μs with [GSH] = 1 mM.	135
B.3	$G(H_2O_2)$ in the gamma-radiolysis of water (1 MeV electron source (simulating first 10 keV)) as function of the scavenging capacity of MeOH for $[NO_3^-]$ = 0.25, 2.5, 25 mM, and 0.25 M	136
B.4	$G(H_2O_2)$ in the gamma-radiolysis of water (1 MeV electron source (simulating first 10 keV)) as function of the scavenging capacity of MeOH for $[SeO_4^{2-}]$ = 2.5, 25 mM, and 0.25 M	138

- B.5 $G(\text{H}_2\text{O}_2)$ in the gamma-radiolysis of water (1 MeV electron source (simulating first 10 keV)) as function of the scavenging capacity of MeOH for $[\text{SeO}_4^{2-}] = [\text{NO}_3^-] = 250 \text{ mM}$ and $[\text{SeO}_4^{2-}] = 250 \text{ mM}$ and $[\text{NO}_3^-] = 25 \text{ mM}$. 139

List of Tables

1.1	Titles of chapters 2 to 5 that cover the work of computational modeling and validation carried out in this thesis and the journals in which they were published or presented.	10
2.1	In-water R_{CSDA} values obtained from the ESTAR database, energy cut-off used, the computational time (CTM) in hours required, and the number of particles by different general-purpose Monte Carlo codes.	20
2.2	Electron range R calculated using EGSnrc, FLUKA, GEANT4-DNA, MCNP6 and PENELOPE for mono-energetic electron sources with initial energy 1-15 keV. R values for 1 keV electron source were not calculated using EGSnrc and FLUKA.	28
2.3	Percentage of passing voxels according to 3D γ -test obtained when comparing the absorbed dose rate distribution at microscopic scale corresponding to different general-purpose Monte Carlo codes using PENELOPE as reference and fixing tolerance to $\Delta\dot{D} = 1\%$ and $\delta\ell = R_{CSDA}(E)/40$	34
2.4	Percentage of passing voxels according to 3D gamma index γ obtained when comparing the absorbed dose rate distribution at macroscopic scale corresponding to different MC codes using PENELOPE as reference and fixing tolerance to $\Delta\dot{D} = 1\%$ and $\delta\ell = 1\text{ mm}$	35
3.1	Energy, R_{CSDA} and, shell thickness for the cases simulated in this work. . .	42
4.1	Comparison of S-values calculated using GEANT4-DNA and EGSnrc for different source target combinations with respect to Sefl et al. 2015 using emission spectrum published by Howell et al. 1992 for Tc-99m and In-111.	62
4.2	S-values calculated using <i>egs_radionuclide_source</i> library of EGSnrc Monte Carlo software and Radioactive decay module of GEANT4 toolkit for various source-target combinations of cellular compartments.	65

5.1	Summary of calculations performed in this study.	75
5.2	Comparison of the cellular S-values (Gy/Bq/s) obtained with EGSnrc for Au-198, I-131, Pd-103, Sm-153 radionuclides with respect to MIRDcell. Five different source-target combinations were considered: ($C \leftarrow C$), ($C \leftarrow CS$), ($N \leftarrow N$), ($N \leftarrow CY$) and ($N \leftarrow CS$) (Table 5.1).	80
5.3	Effective NP washout rate ($k[day^{-1}]$), uptake rate ($m[day^{-1}]$), tumor growth rate ($\lambda[day^{-1}]$), S-value [Gy/Bq/day], ID_0 were calculated using the method explained in section 2 and Table 5.1. Also, critical time (t_c [day]), critical dose rate ($D(t_c)$ [Gy/hr]) and minimum survival fraction ($SF_{min}(t_c)$) were calculated considering $\alpha = 0.059 Gy^{-1}$ for Pd-103 and Au-198, and for Sm-153 $\alpha = 0.0068 Gy^{-1}$	81
5.4	Comparison of calculated S-values (Gy/Bq/s) for different sizes of tumor using EGSnrc with respect to MIRDcell.	84
5.5	The critical time (t_c) [days], critical dose rate ($D(t_c)$) [Gy/hr] and $SF_{min}(t_c)$ calculated for variable tumor size (cc), type, administered activity [MBq] and radionuclide.	85
B.1	List of chemical reactions, for radiolysis of deaerated water, and their reaction rate constants (k) used in this work	131
C.1	Monte Carlo methods table: EGSnrc.	141
C.2	Monte Carlo methods table: Geant4-DNA.	142
C.3	Monte Carlo methods table: EGSnrc.	142
C.4	Monte Carlo methods table: EGSnrc.	143
C.5	Monte Carlo methods table: Geant4-DNA.	144
C.6	Monte Carlo methods table: EGSnrc.	145
C.7	MIRDcell dosimetry tool settings.	145

Nomenclature

Acronyms / Abbreviations

$\Delta\ell$ differences in distance to agreement

δD Dose difference

$\dot{D}(\vec{r}; t)$ Dose rate at position r at time t

K 3 D kernel

E_0 Initial energy

R_{50} Depth at which 50% of initial kinetic energy of electron is lost

R_{90} Depth at which 90% of initial kinetic energy of electron is lost

R_{CSDA} Electron range calculated in the Continuum slowing down approximation

r_{E90} Radius of the sphere in which 90% of the energy of the spectrum electrons would be deposited

AE Auger electron

AEIT Approximate Efficiency Improvement Technique

AuNPs Gold Nanoparticles

BCA Boundary Crossing Algorithm

BSBT Beta-emitting seeds brachytherapy

BT Brachytherapy

CHM Condensed-history method

CK Coster Kronig

CSDA Continuous Slowing Down Approximation

CT Computed Tomography

DPK Dose Point Kernel

DSB Double Strand Break

DTA Distance To Agreement

ENSDF Evaluated Nuclear Structure Data Files

FFT Fast Fourier Transform

G-factor Lea-Catcheside time factor

IMRT Intensity Modulated Radiotherapy

LDR Low Dose Rate

LET Linear Energy Transfer

LINACs Linear accelerators

LQ model Linear Quadratic model

MC Monte Carlo

MGF Mangiferin

MIRD Medical Internal Radiation Dose

NPS Number of particles/histories

NPs Nanoparticles

PDF Probability Density Function

radio-NPs Radioactive Nanoparticles

RBE Relative Biological Effectiveness

RIT Radioimmunotherapy

RT Radiation therapy/Radiotherapy

RV Reference Value

sDPK scaled Dose Point Kernel

SE Single Event

SS Single Scattering

TRT Targeted radionuclide therapy

VRT Variance Reduction Technique

Contents

List of Figures	xv
List of Tables	xix
Nomenclature	xxi
1 General Introduction	1
1.1 Background	1
1.2 Problem statement	6
1.3 Purpose statement	9
1.4 Organization of the Thesis	10
1.5 Declaration	11
1.6 PhD Journey and Achievements	12
2 Monte Carlo Assessment of Low Energy Electron Range in Liquid Water and Dosimetry Effects	15
2.1 Introduction	16
2.2 Materials and Methods	18
2.2.1 Electron range	18
2.2.2 Application to scaled dose point kernel calculation	19
2.2.3 3D dosimetry by kernel convolution	20
2.2.4 General-purpose Monte Carlo codes	24
2.3 Results and Discussions	27
2.3.1 In-water electron range	27
2.3.2 Scaled Dose point kernel calculation	30
2.3.3 Applications to 3D dosimetry	32
2.4 Conclusions	35
2.5 Acknowledgments	36
2.6 Addendum	36

3	Calculation of dose point kernel values for monoenergetic electrons and beta emitting radionuclides: intercomparison of Monte Carlo codes	37
3.1	Introduction	39
3.2	Materials and methods	40
3.2.1	DPK calculation model	40
3.2.2	Monte Carlo codes	42
3.2.3	Code comparison and data analysis	44
3.3	Results and Discussion	44
3.4	Conclusion	51
3.5	Acknowledgement	52
3.6	Addendum	52
4	Microdosimetric calculations for radionuclides emitting β and α particles and Auger electrons	53
4.1	Introduction	54
4.2	Material and Methods	58
4.2.1	GEANT4-DNA	58
4.2.2	EGSnrc	58
4.2.3	The MIRD formalism for S-value estimation	59
4.2.4	Cell geometry and Random point sampling	60
4.2.5	Calculation of S-value and Radial Energy Profile	61
4.3	Results and Discussion	61
4.4	Conclusion	67
4.5	Acknowledgments	68
5	<i>In silico</i> dosimetry of low-dose rate brachytherapy using radioactive nanoparticles	69
5.1	Introduction	70
5.2	Methods	74
5.2.1	Cellular S-values	74
5.2.2	Calculation of surviving fraction	76
5.2.3	Radio-therapeutic efficiency of Pd-103, Sm-153 and Au-198 NPs	77
5.2.4	MIRDcell dosimetry tool	78
5.3	Results and Discussion	79
5.3.1	Cellular S-values	79
5.3.2	Surviving fraction and Tumor volume	80

5.3.3	Comparison of radiotherapeutic efficiency of Pd-103, Sm-153 and Au-198 NPs	83
5.4	Conclusion	88
5.5	Acknowledgments	88
6	Conclusion and Future Directions	91
6.1	Conclusion:	91
6.2	Future Directions	94
	Bibliography	97
	Appendix A Other Publications, Book Chapter and Events	115
A.1	Publications	115
A.2	Events	118
	Appendix B Validation of IRT based extension to TOPAS in terms of impact of variable concentration of scavengers on radiochemistry of water	127
B.1	Introduction	128
B.2	Material and Methods	129
B.2.1	Monte Carlo code: TOPAS	129
B.2.2	Simulation of radiolysis of water and simulation setup:	130
B.2.3	Scavengers and their reaction kinetics	131
B.2.4	Analytical approach	133
B.3	Results	133
B.4	Conclusion	139
	Appendix C Monte Carlo settings used	141
C.1	Chapter 2: Monte Carlo Assessment of Low Energy Electron Range in Liquid Water and Dosimetry Effects	141
C.1.1	EGSnrc	141
C.1.2	Geant4-DNA	142
C.2	Chapter 3: Calculation of dose point kernel values for monoenergetic electrons and beta emitting radionuclides: intercomparison of Monte Carlo codes	142
C.2.1	EGSnrc	142
C.3	Chapter 4: Microdosimetric calculations for radionuclides emitting β and α particles and Auger electrons	143
C.3.1	EGSnrc	143
C.3.2	Geant4-DNA	144

C.4	Chapter 5: <i>In silico</i> dosimetry of low-dose rate brachytherapy using radioactive nanoparticles	145
C.4.1	EGSnrc	145
C.4.2	MIRDcell dosimetry tool	145

Chapter 1

General Introduction

1.1 Background

Radiotherapy is used as one of the main mode of treatment for the patients with inoperable, limited clinical options for surgical resection, solid tumors [1]. Brachytherapy is a cancer treatment technique in which radiotherapy is performed by placing the radiation device or radiation source within and/or near the tumor site [2]. The two main types of brachytherapy techniques are: (i) intracavitary - the radiation source is placed in the body cavities adjacent to the tumor site and, (ii) interstitial - the radiation sources are implanted within the tumor volume. Interstitial brachytherapy has been reported as one of the most suitable method for the treatment of well localized solid tumors from prostate, breast or within brain [3, 4]. Both, low energy e.g. Pd-103 and I-125 and high energy e.g. Au-198/199 radioisotopes have been employed, usually for permanent implant, in brachytherapy [5–7]. I-125 is most widely used radionuclide in these type of applications. One example of application of low dose rate (LDR) brachytherapy (BT) is permanent placement of radioactive seeds, embedded with I-125 or Pd-103, into the prostate gland. In these LDR BT applications low dose of radiation is delivered over a period of several months [8].

The logistical and operational complications associated with the placement of the brachytherapy seed have hindered the successful application of this therapeutic technique. For example, in patients having prostate tumor the radioactive seeds are placed by transrectal ultrasound (TRUS) based implantation technique (indirect visualization) and the implantation of seeds causes trauma and edema within the prostate gland. This may result in inaccurate placement or placement of seeds outside the target volume [9]. This inaccurate or off-target placement of radioactive seeds may result in unwanted radiation exposure to normal tissues (such as: urinary bladder, rectum, etc.), and inaccuracy in seed placement may result in non-uniform dose distributions and may also result in mild to severe clinical side-effects. Some of the

commonly observed side effects and post treatment symptoms are: (a) reduced urine flow, (b) pelvic pain, (c) urinary retention, (d) loose and frequent stools, (e) increased urgency and frequency of urination [10, 11].

Targeted radionuclide therapy (TRT) employs high-affinity molecules as carriers to deliver radionuclides to the tumor cells [12]. The radiopharmaceuticals in TRT are injected intravenously. The injected radiopharmaceutical enters the blood stream (see Fig. 1.1) and after entering, eventually reaches to the target sites.

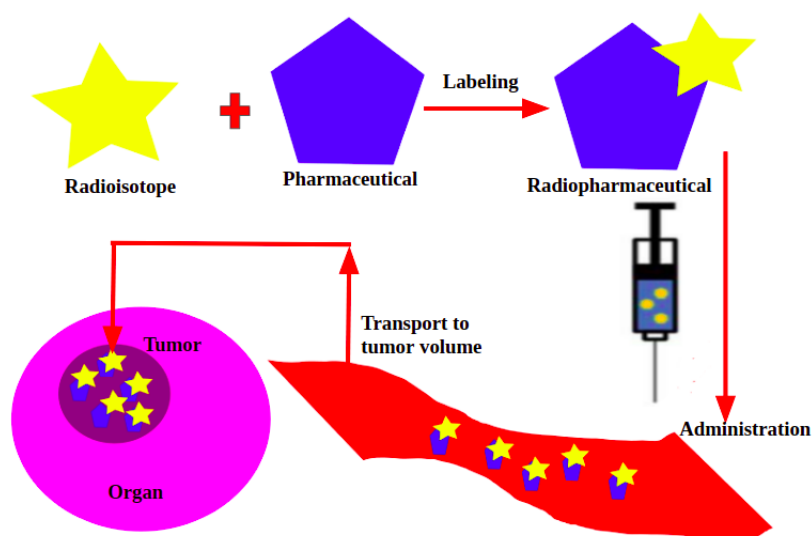


Figure 1.1 The schematic representation of the basic principles on delivery the radiopharmaceutical in the tumor volume in TRT applications. Source: Author.

The two main approaches used to deliver radiopharmaceuticals to the target site in TRT applications are: (i) passive targeting, and (ii) active targeting [13]. In passive targeting technique the radiopharmaceuticals are prepared such that it do not get removed by body mechanisms such as excretion, metabolism, phagocytosis by macrophages or opsonization. The radiopharmaceutical is transported to the target site through blood stream using enhanced permeability and retention (EPR) effect. In solid tumors the blood vessels are highly disordered and swollen, with ample pores and scattered swollen gap junctions between the endothelial cells and compromised lymphatic drainage. These attributes are called EPR effect. Due to EPR effect the radiopharmaceuticals with molecular weight greater than 50 kDa are selectively transported to the tumor interstitium [13, 14]. Whereas, in the case of active targeting the radionuclides are labeled with carrier molecules like antibodies, peptides, nanoparticles etc. to target the antigens overexpressed by the tumor cells [15]. The successful targeting of radiotherapeutic compounds is paramount for the decrease of systemic toxicity,

as an enhanced accumulation in the target tissue prevents toxic actions in healthy cells. This toxic effect is strongly dependent of the concentration of nanomaterials administered, the elements are made out of, the morphology of the nanoparticles, and the surface characteristics (i.e. surface charge and functionalization) [16, 17].

The main objective of TRT is to deliver higher doses of radiation to the tumor cells without causing any damage to the normal tissue [18]. Indeed, the ideal case is not feasible, because there is always a possibility of irradiation to normal tissue during transportation of radiopharmaceutical or catabolism of radiopharmaceutical accompanied by release of the radionuclide [19]. For development of pharmaceuticals with high therapeutic efficacy and prolonged accumulation within the tumor volume, careful selection of radionuclide and carrier molecule is important [20]. TRT is generally used for the treatment of radiosensitive tumors, such as lymphomas and leukemias [21]. There is limited application of TRT for the treatment of solid tumors. It is because the solid tumors present interstitial barriers, have morphological heterogeneity and limited blood supply. Hence, the tumor cells present at the parenchyma are exposed to hypoxic condition and limits the production of the reactive oxygen species (ROS). It makes the tumor cells radio-resistant. The limited blood supply, creates significant challenges in delivery of optimum payloads of radiopharmaceutical, used for TRT applications, at the tumor site [22]. Due to the poor blood supply, the maximum accumulation of the diagnostic/therapeutic agent occurs on the periphery of the tumor wall [23]. Resulting in limited uptake and significant leakage of radioactivity away from the target volume. Such clinical limitations have resulted in reduced efficacy and lower tumoricidal activity of these radiotherapy agents for the treatment of solid tumors [23–25].

For effective treatment of cancer the therapeutic agent must interact at the cellular level by exposing therapeutic payloads to whole tumor volume. Destroying of the cells from the tumor periphery will leave the overall tumor machinery unaffected and partial peripheral therapy may make the tumors resistant to the therapeutic methods [9]. Recently, with the advancements in nanotechnology, some research groups have reported preclinical studies, on both mice and canine models, using radioactive nanoparticles [26–30]. Fig. 1.2 reports the comparison between the radioactive: (i) brachytherapy seeds, and (ii) Au-198 nanoparticles functionalized with Mangiferin, in terms of tumor penetration and distribution. The key features of these nanoparticles (NPs) reported in literature are: (i) it can be retained within the tumor volume for longer duration in comparison to the fast excretion nature of the radiopharmaceuticals, used for TRT applications, (ii) can load more or multiple radioisotopes onto/within the single particle, (iii) tumor specific-targeting can be achieved by surface

functionalization of these particles with suitable biomolecules, (iv) are expected to diffuse uniformly within the tumor volume and deliver uniform dose. Intratumorally injected radioactive NPs, size in the range of 15-30 nm (hydrodynamic size of 30-85 nm), are expected to penetrate the tumor vasculature and deliver optimum payloads to the tumor volume for complete remission of the primary tumor cells [9, 31–33].

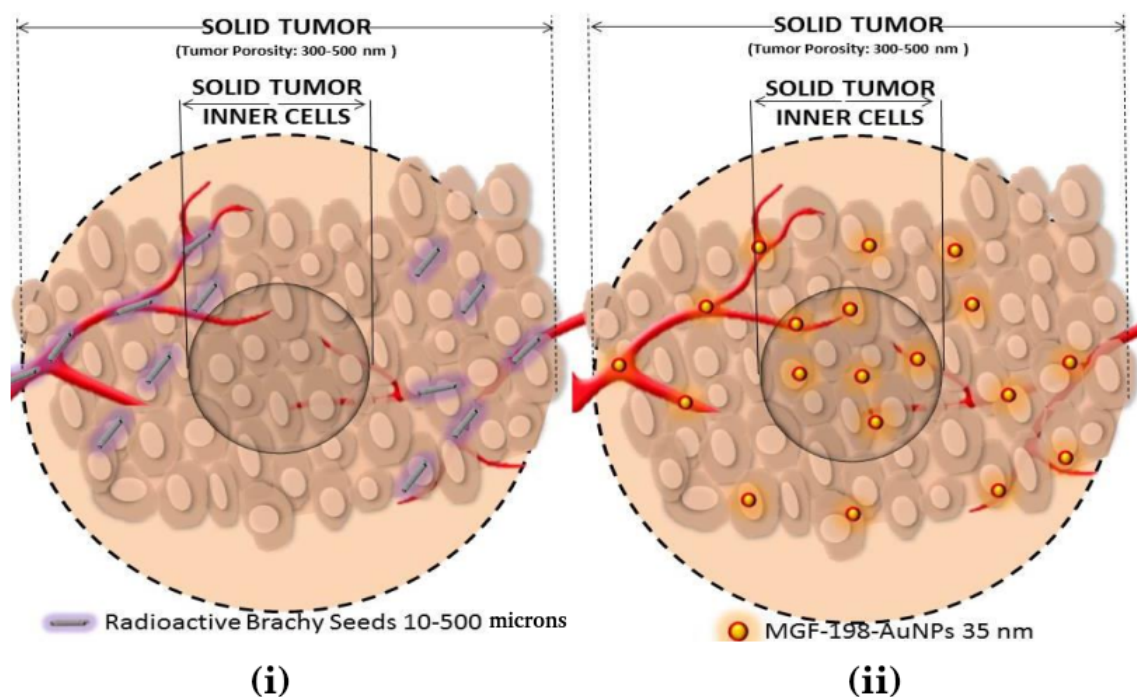


Figure 1.2 Comparison between: (i) Radioactive Brachytherapy seeds and (ii) Au-198 radioactive nanoparticles (NPs) functionalized with Mangiferin (MGF) in terms of tumor penetration and distribution within the tumor. Source: Katti et al. *Journal of Radioanalytical and Nuclear Chemistry* 318.3 (2018): 1737-1747.

The information of the absorbed dose is vital for prediction and evaluation of biological effects. The therapeutic efficacy of different modalities can also be compared using the absorbed dose information. Hence, it is important to quantitatively measure the delivered radiation dose. The use of Monte Carlo (MC) methods is considered as the most accurate way of predicting the dose distributions. The advantages of using MC techniques are: i) efficiency, considering that several cases can be simulated quickly; ii) versatility, since changes in the geometries of the problem they can be performed practically without cost; iii) precision, because the number of particles can be adjusted depending on the error; and iv) simulations involving ionizing radiation do not result in occupational exposures and thus do not require

radiological protection care. Several electron transport models have been developed along the years by the Monte Carlo (MC) code developers, such as Geant4 [34], MCNP6 [35], PENELOPE [36, 37], TOPAS [38], EGSnrc [39].

This PhD thesis aims to perform dosimetry of low dose rate (LDR) brachytherapy applications using radioactive nanoparticle, with the help of Monte Carlo (MC) techniques. Geant4 and EGSnrc are open source MC codes and are widely used for radiation dosimetry. It is expected that both of them are capable of making the required dosimetric calculations. Particularly for the dosimetry of alpha emitters and auger emitters require track structure nature and capability to transport alpha emitters. Further EGSnrc provides user friendly interface to design MC simulation quickly without programming in C++, unlike Geant4. It makes EGSnrc handy tool for initial testing and validation for the cases where experimental data is not available. Hence, Geant4-DNA, and EGSnrc MC codes were used in this work. The used Monte Carlo code version and parameters are documented in Appendix C of this thesis.

Geant4-DNA is a open-source Monte Carlo toolkit, developed to simulate early biological damages caused by ionizing radiation at DNA level. It is an extension of Geant4, a general purpose Monte Carlo toolkit. It is provided within Geant4 and it uses the transport of particles such as electrons, protons, heavy ions, etc. simulating step by step within liquid water or constituents of DNA down to approximately 10 eV. All information about the physics processes, physics models and particles' properties are included in physics constructor. The "G4EmDNAPhysics_option2" ("option2"), "G4EmDNA Physics_option4" ("option4"), and "G4EmDNAPhysics_option6" ("option6") are the three physics constructors recommended by Geant4-DNA to simulate the transport of particles within liquid water [40]. These models handle the photon transport identically. However, they use different physics model to simulate the transport of electrons, protons, heavy ions etc. "Option2" [41] was released publicly with Geant4 version 9.1 in 2007. It is the first combination of discrete physics models included in Geant4 for simulation of electron transport up to eV energies in liquid water. "Option2" uses complex dielectric response function to numerically estimate inelastic cross sections for ionization and excitation. The "option2" has been reported to have deficiencies in the default inelastic models. "Option4", implemented by Kyriakou et al. [42], offers an alternative set of discrete physics models for electron transport in liquid water in the 10 eV-10 keV energy range. It was released with Geant4 version 10.2 in 2016 and provides updated cross sections for ionization and excitation of the water molecules, an alternative elastic scattering model is also present. "Option6", released in 2017 with Geant4 version 10.4, is yet another alternative

combination of discrete physics models for electron transport in liquid water in the 11 eV to 256 keV energy range. It implements the interaction cross sections of the CPA100 track structure code to Geant4-DNA [43]. More details on the type of interactions and processes it supports can be found in [40, 41, 44, 45].

EGSnrc is a general purpose Monte Carlo code capable of simulating the transport of electrons, photons and positrons in energy range of 1 keV to 1 GeV. It is specialized to simulate experiments related to radiation therapy and medical physics. It is divided into several modules to handle problems related to linear accelerators, voxelized cubical phantoms, brachytherapy etc. [46–49]. The electron-electron interaction are simulated using Moller cross sections and Bhabha cross sections are used to simulate electron-positron interactions [50]. The transport of electrons is simulated using mixed approach. Random sampling methods are used to simulate hard bremsstrahlung, hard inelastic collisions and annihilation interactions, where by the loss of energy is above the threshold value. Interactions where energy loss is lesser than threshold value are subjected to grouping. The concept of boundary crossing algorithm (BCA) is used to simulate the electron transport near the interfaces and heterogeneous mediums. Electrons crossing the boundaries are simulated using the single scattering (SS) mode. The distance at which BCA activates SS mode is resolved by "Skin depth for BCA" parameter.

1.2 Problem statement

There is limited literature available on the dosimetry of LDR brachytherapy applications using radioactive nanoparticles (radio-NPs). Al-Yasiri et al. (2019) [51], used MCNP6 Monte Carlo code to simulate the dose distribution within the prostate tumor and normal organs at risk. This study used a simple spherical model of prostate, bladder and rectum and the dose distribution due to Au-198 or Au-199 radio-NPs, injected into prostate tumor volume, was estimated. Furthermore, L-Pelletier et al. (2018) [33], performed a microdosimetry study using MC methods to understand the relationship between the intracellular and interstitial distribution of radio-NPs and its impact on dose distribution. The authors used NPs with radioactive core of Pd-103 and outer covering of gold (Au), aiming to use the radiosensitization effect of Au. According to authors most of the injected NPs were found confined around the vesicles and limited NPs managed to reach close to the nucleus. The authors suggested that the main mechanism involved in tumor volume control is the production of

reactive oxygen species. The remaining other studies are mainly *in-vivo* studies on mice or canine models [26–30], where outcomes are mainly expressed in cells of cell survival curves or tumor volume curve function of time.

The three variables in dosimetry, using MC methods, for LDR BT applications using radio-NPs, to consider are: (i) Accuracy of the Monte Carlo code; (ii) Selection of radionuclides and radioactivity to be administered for such applications; (iii) Taking into account the affect of uptake rate, washout rate of NPs and, growth rate and radiosensitivity of tumor cells on absorbed dose and cell survival curves. The gaps present in literature, and considered in this PhD thesis, are discussed briefly below:

1. In performing dosimetry using Monte Carlo codes, the most important part is to validate the code and test its accuracy. Dose point kernel (DPK) comparison is generally used to test the accuracy of electron transport model of the MC codes. For example, Champion et al. 2014 [52], Botta et al. 2011 [53] and several other authors performed intercomparison of MC codes in terms of DPK. Most of these studies use old versions of code which are no more used and none of them investigate the impact of discrepancies in DPK on the absorbed dose, both at cellular and tumor level. As it can be appreciated from Figure 1.3(A), the DPK calculated for 10 keV electron source using several MC codes deviate from each other. Hence, it is important to investigate the impact of differences in DPK on the electron range and absorbed dose. How much the electron penetration depth calculated by MC code differ from the continuous slowing down approximation range (CSDA) range? Is there any range parameter that can be defined as a characteristic to electron source with particular energy? Like different range parameters defined for high energy electrons in AAPM report TG 25 [54].
2. How much MC calculated DPK differ in energy range of 50 keV to 3 MeV, energy range covering the majority of radionuclides, used in nuclear medicine, energy spectra? If difference exists, what is causing this difference? What happens if the emission spectrum is used instead of monoenergetic source to compute DPK and test the accuracy of MC code?

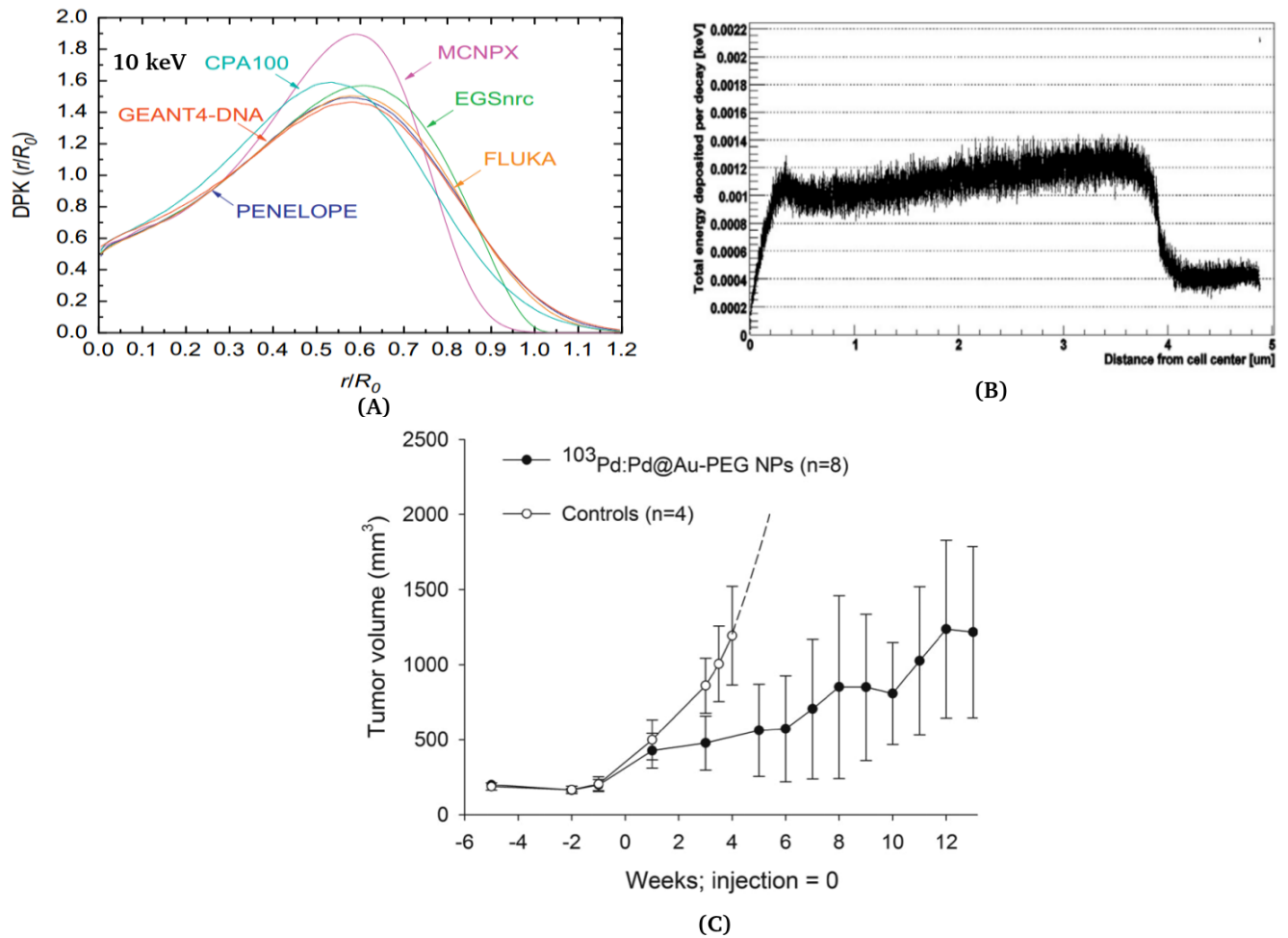


Figure 1.3 (A) Dose point kernels estimated using several Monte Carlo codes for 10 keV monoenergetic electron source by Champion et al. 2014. (B) Radial energy deposition curve for radioactivity (I-123) uniformly distributed within the nucleus for single cell dosimetry by Fourie et al. 2015 (C) Tumor volume follow-up for in-vivo study performed for treatment of PC3 xenograft tumors using Pd-103 radioactive nanoparticles by L-Pelletier et al. 2017.

3. The therapeutic efficacy of radionuclides used for theranostic applications is tested using single cell study [55–58]. No single study compares the therapeutic efficacy of all alpha, low-, medium-, and high energy beta emitters and auger emitters together. Can the localized energy deposition property of auger emitters and cross fire effect of beta emitters be shown graphically? Fourie et al. 2015 [56], has shown something like radial energy profiles (See Figure 1.3(B)), why there is a hump near the center of the cell? Do this hump affect the mean dose deposited?
4. How to include the affect of uptake rate, washout rate of NPs and, growth rate and radiosensitivity of tumor cells in dose estimation and cell survival curves? The thera-

peutic efficacy of radio-NPs for LDR BT treatments have been widely investigated by *in-vitro* and *in-vivo* studies [9, 59, 60, 31, 33]. For example, L-Pelletier et al. 2017 [31] investigated the therapeutic efficacy of Pd-103 radioactive nanoparticles by performing *in-vivo* study to treat PC3 xenograft (See Figure 1.3(C)). The tumor cell survival fraction starts increasing after first week of radioactive injection. This displays the need of mathematical model or MC calculations, which can be used to guide, to design better preclinical studies, the selection of radionuclides and administration activity based on volume, growth rate and radiosensitivity of tumor, washout and uptake rate of nanocarriers.

1.3 Purpose statement

The purpose of this doctorate project was to fill the gaps mentioned in the above section. The key objectives were:

1. To: (i) validate EGSnrc and Geant4-DNA MC codes, (ii) test accuracy of their electron transport models in terms of DPK comparison, for electrons with initial energy 1 keV to 50 keV, (iii) investigate the impact of discrepancies in DPK on the absorbed dose, both at cellular and tumor level, (iv) analyze the impact of differences in DPK on the calculated electron range and compare it with CSDA ranges reported in literature, (v) search for range parameter that can be defined as a characteristic to monoenergetic electron source.
2. To perform a intercomparison between MC codes in terms of DPK for electrons with initial energy: 50 keV to 3 MeV. If difference in DPK exists, quantifying the differences and finding the cause of the differences. Additionally, comparing DPK computed using the emission spectrum of the radionuclide as input.
3. To: (i) perform a therapeutic efficacy study for radionuclides emitting alpha, beta (low, medium and high energy emitters), and auger emitters using single cell dosimetry approach, (ii) showing the localized energy deposition property of auger emitters and cross fire effect of beta emitters graphically, (iii) searching the cause of hump near the center of the cell, reported by Fourie et al. 2015 [56], and (iv) find if it has any impact on the mean absorbed dose.
4. Replicating the cell survival curves reported in preclinical studies using radio-NPs as brachytherapeutic agent. Extracting the uptake rate and washout rate of NPs from the pharmacokinetic data and, growth rate of tumor cells from the cell survival curve

of the control group and using them to estimate the cell survival curves. This study is expected to act as a guide, to design better preclinical studies, by helping in the selection of radionuclides and activity to be administered based on volume, growth rate and radiosensitivity of tumor, washout and uptake rate of the nanocarriers.

1.4 Organization of the Thesis

The present thesis contains six chapters and three appendices. First chapter provides brief background on obstacles involved in the application of interstitial or intratumoral brachytherapy or targeted radionuclide therapy for the treatment of solid tumors. The gaps present in the literature and the main objectives of the research work performed in this thesis are also briefly discussed.

Table 1.1 Titles of chapters 2 to 5 that cover the work of computational modeling and validation carried out in this thesis and the journals in which they were published or presented.

Chapter #	Title	Place of Publication/Presentation
2	Monte Carlo Assessment of Low Energy Electron Range in Liquid Water and Dosimetry Effects	Published in European Journal of Medical Physics (Physica Medica)
3	Calculation of dose point kernel values for monoenergetic electrons and beta emitting radionuclides: intercomparison of Monte Carlo codes	Published Radiation Physics and Chemistry Journal
4	Microdosimetric calculations for radionuclides emitting β and α particles and Auger electrons	Published in Applied Radiation and Isotope Journal. 166 (2020): 109302. Also presented in ISSSD2019, Mexico
5	<i>In silico</i> dosimetry of targeted anti-tumor therapy using radioactive nanoparticles	Published in Physics in Medicine and Biology Journal

Chapters 2 to 5 can be considered self-contained and can be read separately or in sequence. The introduction of each chapter comprises of detailed literature review. Chapter 2 reports intercomparison between 5 MC codes: MCNP6, EGSnrc, GEANT4-DNA, PENELOPE and FLUKA, in terms of electron penetration depth and DPK, for electrons in the energy range of 1-50 keV. Further, as an application of DPK, the 3D-voxelized dosimetry both at microscopic and macroscopic scale was performed. The third chapter additionally reports intercomparison

of 4 Monte Carlo codes: TOPAS, PENELOPE, EGSnrc and MCNP6, in terms of DPK, with different physics parameter settings. It aims to test the the computational accuracy of the MC codes with different physics settings for 50 keV to 3 MeV monoenergetic electron sources and several beta emitting radionuclides. In chapter 4 the therapeutic efficacy of Auger, alpha and beta emitting radionuclides is evaluated using the single cell dosimetry approach. The calculations were performed for spherical cell model, nucleus radius of 4 μm and cell radius of 5 μm , using EGSnrc and GEANT4-DNA. For single cell dosimetry, the source and target region combinations were: C \leftarrow C, C \leftarrow CS, N \leftarrow Cy, N \leftarrow N, and N \leftarrow CS, where C: Whole Cell, N: Nucleus, Cy: Cytoplasm and CS: Cell Surface. The effect of difference in emission spectra on the calculation of S-values is also reported. In fifth chapter the therapeutic efficiency of nanoparticles labeled with Au-198, Pd-103 and Sm-153 is reported. The study was performed in three stages. At first step single cell dosimetry was performed using the model described in chapter 4 for Au-198, Pd-103 and Sm-153 using EGSnrc MC code. Secondly the cell survival curves were calculated using the mathematical formalism and curves were compared with experimental data published in literature. At third step, the therapeutic efficiency of the radionuclides was tested by calculating cell survival curves for variable radioactivity administered, tumor size and radiosensitivity of tumor cells. Chapter 6 provides the conclusion to this work and future directions. The first appendix (Appendix A) section the brief introduction to other published articles is includes. Further, the information related to the participation of the author in different events is included. Appendix B includes the unpublished article and the information on the Monte Carlo settings used in the studies reported as chapter 2-5 of this thesis is tabulated in Appendix C.

1.5 Declaration

It should be noted that first two research works:

1. Chapter 2: Monte Carlo Assessment of Low Energy Electron Range in Liquid Water and Dosimetry Effects
2. Chapter 3: Calculation of dose point kernel values for monoenergetic electrons and beta emitting radionuclides: intercomparison of Monte Carlo codes

were performed in collaboration with other research groups.

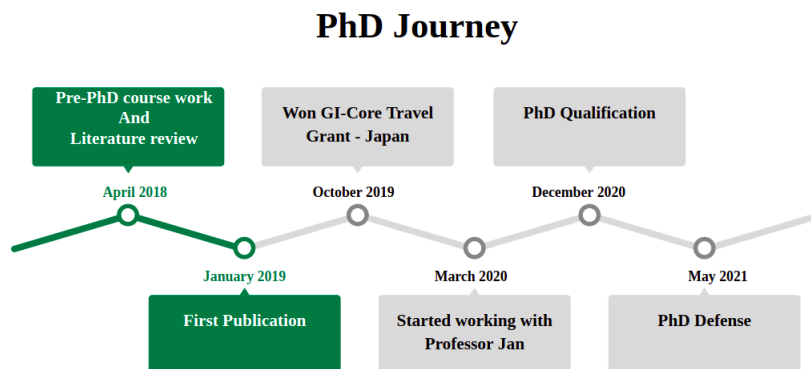
The MCMEG international group coordinate by Prof. Telma C. F. Fonseca, my promoter, is an expert network specialized in MC radiation transport modelling and simulation applied to the radiation protection and dosimetry research fields (<https://groups.google.com/g/mcmeg>)

and the intercomparison exercise demonstrated its relevance by showing the influence of different modelling approaches and different MC codes, achieving interesting analysis.

In chapter 2, (i) the initial idea, (ii) implementation, (iii) EGSnrc and Geant4-DNA calculations, (iv) data analysis (v) writing original manuscript and (vi) reply to reviewer's comments were done by me. Whereas, in case of chapter 3, my role was limited to: (i) performing EGSnrc calculations, and (ii) writing and reviewing original manuscript. These chapters were added in this thesis because the reported research work was performed and published during the PhD. Further, due to the unavailability of the experimental data (particularly for low energy electrons) the accuracy of electron transport models implemented in the MC codes is tested/validated/benchmarked by performing intercomparisons in terms of DPK. Additionally, one of the main objective of this thesis (achieved through these publications) was to test the accuracy of electron transport algorithms implemented in Geant4-DNA and EGSnrc.

The remaining work published and reported in this thesis was done by me.

1.6 PhD Journey and Achievements



Research Production and Achievements

1. B. Seniwal, T.C.F. Fonseca *et al.* " Microdosimetric calculations for radionuclides emitting β - particles, Auger electrons, and α -particles." *Applied Radiation and Isotopes* 166 (2020): 109302.
2. B. Seniwal, T.C.F. Fonseca *et al.* "Monte Carlo Assessment of Low Energy Electron Range in Liquid Water and Dosimetry Effects." *Physica Medica* 80 (2020): 363-372.
3. B. M. Mendes, B. Seniwal, T.C.F. Fonseca *et al.* "Calculation of dose point kernel values for monoenergetic electrons and beta emitting radionuclides: Intercomparison of Monte Carlo codes." *Radiation Physics and Chemistry* 181 (2021): 109327.
4. B. Seniwal, T.C.F. Fonseca *et al.* "In silico dosimetry of low-dose rate brachytherapy using radioactive nanoparticles." *Physics in Medicine & Biology* 66.4 (2021): 045016.
5. B. Seniwal, T.C.F. Fonseca *et al.* "Monte-Carlo Modelling For Evaluation Of Two Different Calculation Algorithms." *Brazilian Journal of Radiation Sciences* 7.1 (2019).
6. T.C.F. Fonseca, B. Seniwal *et al.* "MCMEG: Intercomparison Exercise On Prostate Radiotherapy Dose Assessment". *Radiation Physics and Chemistry* 167 (2019): 108295.
7. B. Seniwal, T.C.F. Fonseca *et al.* "Comparison Of Dosimetric Accuracy Of Acuros Xb And Analytical Anisotropic Algorithm Against Monte Carlo Technique." *Biomedical Physics & Engineering Express* 6.1 (2020): 015035.
8. H. Donya, B. Seniwal, T.C.F. Fonseca. "Prospective Monte Carlo simulation for choosing high efficient detectors for small field dosimetry." *Theory and Applications of Monte Carlo Simulations* (ISBN 978-1-78985-546-3)(DOI: 10.5772/intechopen.89150)(2019).
9. B. Seniwal, T.C.F. Fonseca, J. Schuemann *et al.* "Validation of IRT based extension to TOPAS in terms of impact of variable concentration of scavengers on radiochemistry of water" (to be submitted)

Chapter 2

Monte Carlo Assessment of Low Energy Electron Range in Liquid Water and Dosimetry Effects

Baljeet Seniwal¹, Bruno M. Mendes², Francisco Malano³, Pedro Pérez⁴, Mauro Valente^{4,5}, Telma C.F. Fonseca^{1,*}

¹Departamento de Engenharia Nuclear (DEN/UFMG) & Programa de Pós-graduação em Ciências e Técnicas Nucleares (PCTN) - Universidade Federal de Minas Gerais (UFMG), Av. Antônio Carlos, 6627, Pampulha, 31270-901, Belo Horizonte, MG, Brazil

² Centro de Desenvolvimento da Tecnologia Nuclear - CDTN/CNEN, Belo Horizonte, MG, Brasil

³Departamento de Ciencias Físicas & Centro de Física e Ingeniería en Medicina (CFIM), Univesidad de La Frontera, Temuco, Chile.

⁴ Instituto de Física E. Gaviola, CONICET & Laboratorio de Investigación e Instrumentación en Física Aplicada a la Medicina e Imágenes por Rayos X (LIIFAMIR^x), Facultad de Matemática, Astronomía, Física y Computación, Universidad Nacional de Córdoba, Medina Allende esq. Haya de la Torre, Córdoba, Argentina.

⁵Centro de Física e Ingeniería en Medicina (CFIM) & Departamento de Ciencias Físicas, Univesidad de La Frontera, Temuco, Chile.

Corresponding author: Telma C.F. Fonseca (telmafonseca@nuclear.ufmg.br)

Journal name: European Journal of Medical Physics.

Citation: Seniwal, B., Mendes, B. M., Malano, F., Pérez, P., Valente, M., & Fonseca, T. C. (2020). Monte Carlo assessment of low energy electron range in liquid water and dosimetry effects. *Physica Medica*, 80, 363-372.

Abstract

The effects of low energy electrons in biological tissues have proved to lead to severe damages at the cellular and sub-cellular level. It is due to increase in the relative biological effectiveness (RBE) of these electrons with decrease in their penetration range. That is, lower the range higher will be its RBE. Therefore, accurate determination of low energy electron range becomes a key issue for radiation dosimetry. This work reports on in-water electron tracks evaluated at low kinetic energy (1-50 keV) using isotropic mono-energetic point source approach suitably implemented by different general-purpose Monte Carlo codes. For this aim, simulations were performed using PENELOPE, EGSnrc, MCNP6, FLUKA and Geant4-DNA Monte Carlo codes to obtain the particle range, R , R_{90} , R_{50} . Finally, evaluation of dose point kernel (DPK), as used for internal dosimetry, was carried out as an application example. Scaled dose point kernels (sDPK) were estimated for a range of mono-energetic low energy electron sources. The non-negligible differences among the calculated sDPK using different codes were obtained for energy electrons up to 5 keV. It was also observed that differences of in-water range for low-energy electrons, due to the different general-purpose Monte Carlo codes, affected the DPKs used for dosimetry by convolution approach. Finally, the 3D dosimetry was found to be almost not affected at a macroscopic clinical scale, whereas non-negligible differences appeared at the microscopic level. Hence, a thorough validation of the used sDPKs have to be performed before they could be used in applications to derive any conclusions.

Keywords: Dosimetry, Microdosimetry, DPKs, Low energy electrons, MC codes.

2.1 Introduction

High energy ionizing radiations, such as γ -rays, X-rays etc., interact with matter resulting in the production of low energy electrons [61]. These low energy electrons also are known as secondary electrons may lead to severe damages at the cellular and sub-cellular level causing biological effects in the human body [62, 63]. Interactions of electrons with water molecules are popular and important phenomena in nature [64]. Many researchers have studied the slowing down and energy deposition of electrons in liquid water for different clinical applications [65, 40, 66–70]. The most important among these applications, since

liquid water is considered to be a good tissue-like medium, is related to its relevance to the physics of ion-beam cancer therapy and radiation protection in space [40]. Ion-beam cancer therapy has become an powerful operative treatment tool, based on theoretical and computational methods of basic science [71]. In nuclear medicine, the targeted radionuclide therapy is increasingly growing demanding advanced and fast methodologies, among others the voxel-based dosimetry, to estimate radiopharmaceutical dosimetry [72].

According to AAPM Task Group 25 [54] on clinical electron-beam dosimetry different range definitions are introduced to measure the quality of electron beam. These definitions lose their meaning for low energy electrons. Track structure codes are generally used to simulate the track of electrons [40, 66]. Several other research groups have been studying and proposing new approaches to include exchange and correlation effects for electron scattering at low energies [67, 73]. Meesungnoen and co-workers reported a comparison between the experimentally measured and computationally estimated penetration ranges of electrons with energy ranging from 0.2 eV to 150 keV [68]. El-Ghossain et al. [70], calculated stopping power and range of electrons with energy of 10 keV up to 1 GeV using Bethe-Bloch formulation for skin, water, adipose tissue, muscle tissue and bone using ESTAR [74] and MATLAB [75] codes.

The dose point kernel (DPK) is used in nuclear medicine dosimetry to describe the energy deposited at a particular distance from a point isotropic radiation source [76]. Uusijärvi et al. [77], compared DPK calculated with PENELOPE (v. 2006) [78], mixed Monte Carlo code, with those generated using ETRAN [79], GEANT4 [80] and MCNPx [81], condensed history based Monte Carlo (MC) codes. The authors calculated the S-values from the DPK obtained to investigate the change in difference when dose point kernels are used for absorbed dose calculations, the S-values were also compared to the Medical Internal Radiation Dose (MIRD) cellular S-values [82]. The authors concluded that the choice of MC code is not crucial when calculating S-values from the dose point kernels. Champion et al. [52], reported the comparison of the DPKs obtained by GEANT4-DNA [41], EGSnrc [50], PENELOPE, CPA100 [83], FLUKA [84, 85] and MCNPx for electron energies ranging from 10 to 100 keV. It was reported that the differences in the DPK relied on the different physics models used in different MC codes to simulate the electron transport. Botta et al.[53], calculated dose point kernels for both in water and compact bone using FLUKA Monte Carlo code for mono-energetic electron sources and β -emitting radionuclides. The computed DPK was compared against PENELOPE, ETRAN, GEANT4 and MCNPx. In water 12% maximum difference between the DPK calculated with FLUKA in comparison to PENELOPE for

electrons with energy 10 and 20 keV was reported. Whereas for higher energy electrons the DPK values were reported in agreement within 7%.

Therapeutic nuclear medicine practices administer radiopharmaceuticals to patients aimed at reaching the prescribed tumour dose while limiting dose delivered to surrounding healthy tissues within tolerance levels[86, 87]. Patient-specific radioimmunotherapy efficacy is mainly based on an accurate assessment of the absorbed dose distribution [88, 89]. Following radiolabeled agent/antibody uptake, the activity biodistribution heterogeneity at both microscopic and macroscopic levels strongly limit the accuracy of the MIRD S-factors model [90], therefore, requiring more sophisticated models for patient-specific 3D dosimetry. In order to overcome this, dose-point kernel convolution technique may be implemented to estimate 3D absorbed dose rate distributions [89] on a voxelized framework. Here, a theoretical study was performed, as a collaborative work distributed in four groups to assess the differences/similarities among the general purpose MC codes for in-water low energy electron range and further applications to scaled dose point kernels. In this regard, Group1 performed simulations using PENELOPE(2014) [91], Group2 used FLUKA [84, 85], Group3 used EGSnrc [50], and Geant4-DNA [41] and Group4 used MCNP6 [92]. The results obtained from the different MC codes for scaled dose point kernels ($sDPK$) and the range R of mono-energetic electrons, along with associated magnitudes, like R_{50} and R_{90} are evaluated for electrons with initial kinetic energy from 1 up to 50 keV. In-water electron $sDPK$ and corresponding consequences at dosimetry level are reported, compared and discussed.

2.2 Materials and Methods

The procedures for assessing in-water electron range for the different Monte Carlo codes along with corresponding further consequences on dosimetry are described in the following subsections.

2.2.1 Electron range

The track length of mono-energetic electrons with initial energy (E_0) ranging from 1 up to 50 keV was investigated. Isotropic and mono-energetic (1, 5, 10, 15, 20, 25, 30, 40 and 50 keV) electron sources were considered at the center of an unit-density water sphere. The absorption energy used for MCNP6, PENELOPE, FLUKA, EGSnrc and Geant4-DNA Monte Carlo (MC) codes are reported in Table 2.1. In order to estimate the range of low-energy electrons the following three parameters were proposed:

1. Electron range (R): sum over all displacement tracks followed by the electron, i.e. integration over s , where s is the particle path.
2. R_{90} : It was calculated from the depth dose curve. It is defined as the depth at which 90% of initial kinetic energy of electron is lost.
3. R_{50} : the net travelled distance until "loosing" 50% of initial kinetic energy. It is the same as R_{90} , but computing up to $0.5E_0$ instead of $0.9E_0$.

2.2.2 Application to scaled dose point kernel calculation

A potential practical application of the obtained track length results regarding the accurate computation of in-water electron range and associated magnitudes, scaled dose point kernels ($sDPK$) were also calculated. The mono-energetic electron sources have been considered as emulating an isotropic point source placed in the center of a water sphere and energy deposition has been computed in the concentric shells having as thickness ($\delta E(r)$) of $0.025R_{CSDA}$, where R_{CSDA} denoted the electron range calculated in the Continuum slowing down approximation [53]. Figure 2.1 shows the geometry used in the simulations with the MC codes to compute $sDPK$.

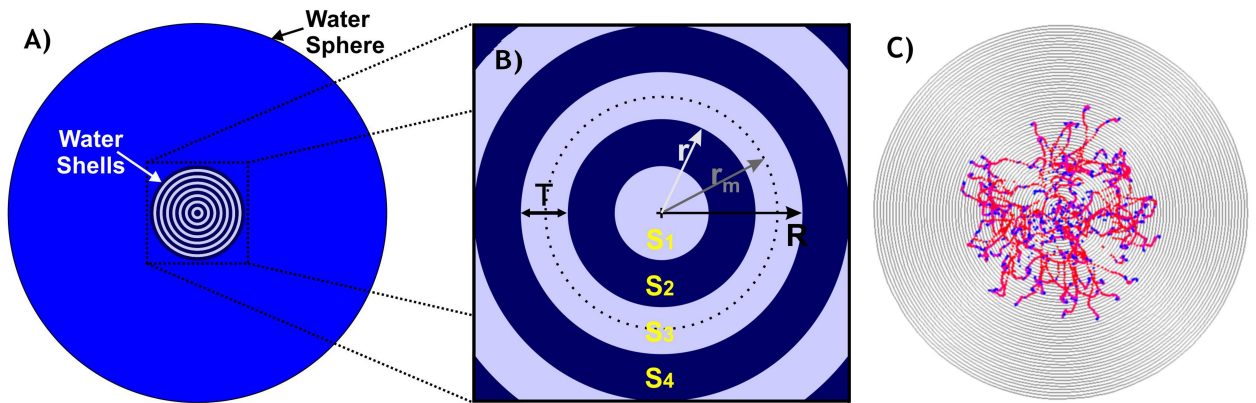


Figure 2.1 A) Water shells immersed in a water sphere, the scoring was done within the shells. The maximum radius of the water spheres was set to $1.5R_{CSDA}$. B) Zoom view of the center of the water shells; $S_1, S_2, S_3, S_4 \dots S_i$ are the numbers of the shells; T is the shell thickness ($T = 0.025R_{CSDA}$); R is the outer radius of a shell ($R = S_i \cdot (0.025R_{CSDA})$); r is the inner radius of a shell ($r = (S_i - 1) \cdot (0.025R_{CSDA})$); r_m is the mean radius of a shell ($r_m = ((R+r)/2)$). C) MCNP Visited view of the isotropic, point and mono-energetic 50 keV electron source tracks.

The scaled point kernel ($sDPK$) have been calculated as a function of the radius in units of r/R_{CSDA} , according to [53]:

$$sDPK \equiv \frac{\delta E(r)/E_0}{\delta r/R_{CSDA}} \quad (2.1)$$

where E_0 is the electron source kinetic energy.

Within this framework, a total of 5 representative cases (1, 5, 10, 25 and 50 keV) have been considered. In-water $sDPK$ values were obtained for assessing the similarities and differences among the different MC codes at low energy levels. The corresponding reference values for R_{CSDA} were obtained directly from ESTAR (NIST, USA) database [74] or extra/interpolating (bi-cubic spline) and they are reported in Table 2.1.

Table 2.1 In-water R_{CSDA} values obtained from the ESTAR database, energy cut-off used, the computational time (CTM) in hours required, and the number of particles by different general-purpose Monte Carlo codes.

Source Energy [keV]	R_{CSDA} [um]	Cutoff [keV]	CTM [hours], Number of Particles (for Statistical Error <1%)				
			MCNP6	EGSnrc	Geant4-DNA	FLUKA	PENELOPE
1.00	0.04	0.10	0.24, 1E+07	-	0.77, 1E+05	-	0.36, 1E+08
5.00	0.75	1.00	0.52, 1E+07	0.30, 1E+07	4.77, 1E+05	15.87, 1E+09	2.11, 1E+08
10.00	2.52	1.00	1.56, 1E+07	0.52, 1E+07	8.46, 1E+05	39.95, 1E+09	4.25, 1E+08
15.00	5.15	1.00	2.29, 1E+07	0.59, 1E+07	13.42, 1E+05	56.27, 1E+09	5.87, 1E+08
20.00	8.57	1.00	2.93, 1E+07	0.82, 1E+07	16.40, 1E+05	68.89, 1E+09	7.13, 1E+08
25.00	13.00	1.00	3.52, 1E+07	0.93, 1E+07	20.09, 1E+05	79.56, 1E+09	8.24, 1E+08
30.00	17.60	1.00	4.02, 1E+07	1.13, 1E+07	23.79, 1E+05	88.03, 1E+09	9.38, 1E+08
40.00	29.20	1.00	5.04, 1E+07	1.33, 1E+07	27.88, 1E+05	106.07, 1E+09	11.05, 1E+08
50.00	43.20	1.00	5.99, 1E+07	1.36, 1E+07	30.14, 1E+05	127.54, 1E+09	12.96, 1E+08

2.2.3 3D dosimetry by kernel convolution

Absorbed dose rate distribution can be estimated by means of convolution patient-specific activity distribution with the corresponding dose point kernel, which is previously obtained by Monte Carlo simulation, for example, typically within the framework of a homogeneous (in chemical composition and mass density) medium. Thus, the dose rate $\dot{D}(\vec{r};t)$ in each voxel is assessed by the superposition of contributions due to the activity in the surrounding voxels. This operation, for a discretized/voxelized space, can be mathematically formalized through a discrete expression of the convolution Equation 2.2 as follows:

$$\dot{D}(i, j, k; t) = \frac{1}{\mu} \sum_{r=1}^{2V+1} \sum_{s=1}^{2V+1} \sum_{u=1}^{2V+1} A(i-V+r-1, j-V+s-1, k-V+u-1; t) \mathbf{K}(r, s, u; t) \quad (2.2)$$

where $\mu = \sum_{i,j,k=1}^{2V+1} \mathbf{K}(i, j, k; t)$, and $\mathbf{A}_{N \times M \times L}$ and $\mathbf{K}_{(2V+1) \times (2V+1) \times (2V+1)}$ are the 3D matrix representations of the activity distribution, and the dose point kernel, respectively. A condition must be satisfied in this Equation: $2V + 1 < n, m, l$. Thus, the resulting dose rate will be a $(N - V - 1) \times (M - V - 1) \times (L - V - 1)$ matrix.

Technically, there are different approaches aimed at solving Equation 2.2, including algorithms for forward and inverse fast Fourier transform (FFT) using properties of the Fourier theorem; or direct discrete 3D convolution algorithms, as implemented in this work, according to Equation 2.3:

$$C(j_1, j_2, \dots, j_N) = \sum_{k_1} \sum_{k_2} \dots \sum_{k_N} A(k_1, k_2, \dots, k_N) B(j_1 - k_1, j_2 - k_2, \dots, j_N - k_N) \quad (2.3)$$

where C denotes the convolution of A and B tensors and each k_i runs over all values that lead to allowed indices of A and B .

The 3D dose rate distributions were calculated using two different approaches. The first one, aimed at the microscopic scale level, consisted of a uniform water-equivalent ($121 \times 121 \times 1286$) phantom with cubic voxel side equals to $R_{csda}(E)/40$ and active voxels were defined according to Figure 2.2. As it can be observed, a first individual voxel was activated and then increasing distance pairs of activated voxels array were performed.

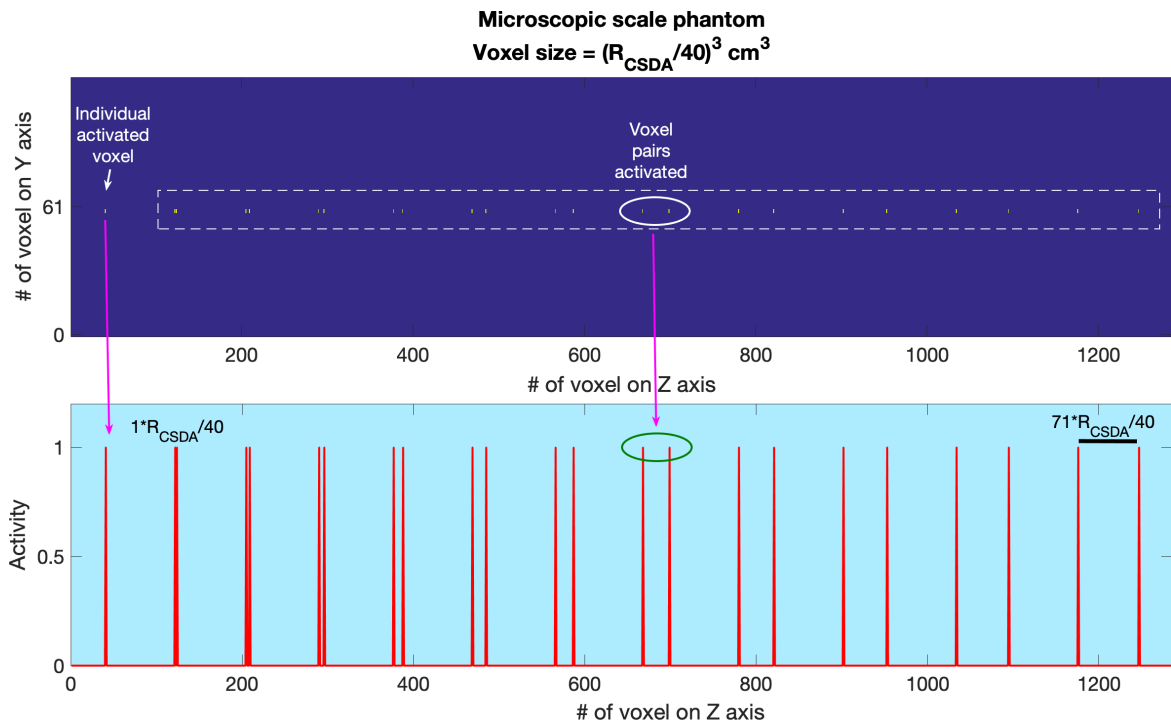


Figure 2.2 Water-equivalent phantom for 3D dosimetry at microscopic scale by kernel convolution. Active voxels (uniformly activated) are highlighted. YZ 2D slice (top) and XY centered z-plot (bottom) are presented.

The second approach, aimed at representing typical, macroscopic, clinical situations. It consisted of a standard nuclear medicine calibration phantom, for example, an image by dual SPECT-CT using ^{99m}Tc radiolabeled agent, as depicted in Figure 2.3

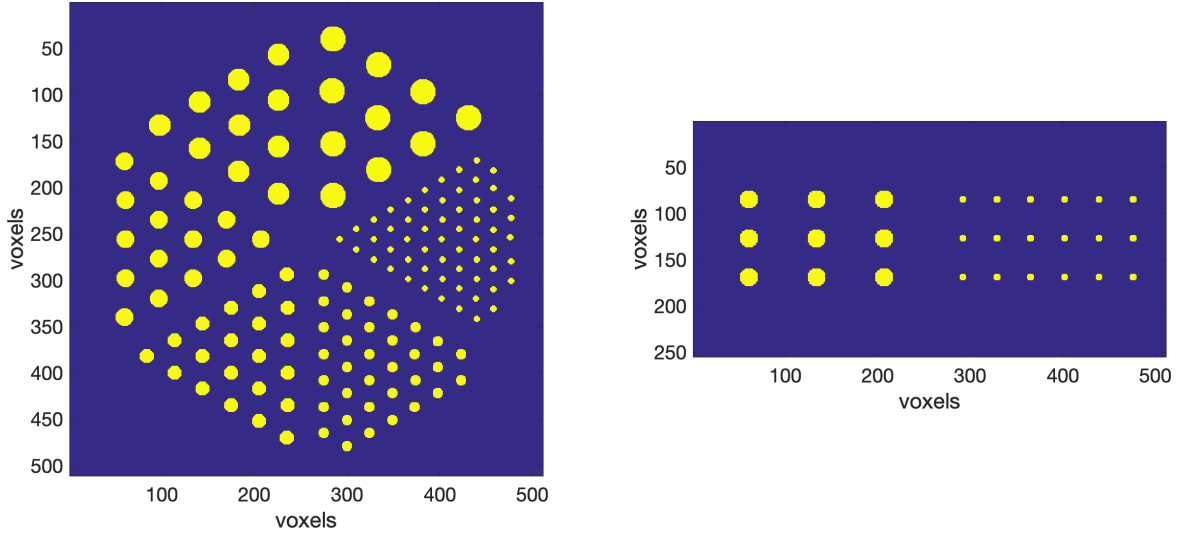


Figure 2.3 Activity distribution transverse (left) and longitudinal (right) slices within the calibration phantom used for 3D dosimetry at macroscopic scale by kernel convolution.

The 3D kernel \mathbf{K} for 3D dosimetry convolution was constructed in terms of the (1D) radial $sDPK$. Briefly, the process consisted on assuming isotropy and uniformity, which are actually the assumptions for calculating $sDPK$ according to Equation 2.1 along with cubic spline interpolation for assessing $\mathbf{K}(n, m, l)$ according to $sDPK(r)$ and establishing the correspondence in terms of the Euclidean distance $d(n, m, l)$ from any (n, m, l) voxel to the kernel center $(N/2, M/2, L/2)$, as stated in Equation 2.4:

$$d(n, m, l) = \sqrt{(n - N/2)^2 + (m - M/2)^2 + (l - L/2)^2} \quad (2.4)$$

Finally, once \dot{D} distributions are obtained by means of convolution using $sDPK$ corresponding to different general-purpose Monte Carlo codes, it becomes necessary to perform quantitative comparisons. The gamma index γ [93] is commonly used for comparing absorbed dose distributions for clinical purposes [94]. It is customary to apply the pass-fail test consisting of computing the percentage of evaluated voxels passing/failing the test if γ is higher or lower than unity [94]. In these tests (user predefined) tolerances are defined in terms of differences in distance to agreement (DTA) denoted by $\Delta\ell$ and dose (D) denoted as δD with respect to the reference value. Detailed discussion on γ index, $\Delta\ell$ and δD can be found in Ref. [93].

In this study, for 3D γ test the absorbed dose distribution obtained using PENELOPE MC code, at both microscopic and macroscopic scale, was considered as a reference value in comparison of the calculations performed using other MC codes. For microscopic scale,

the tolerance was set to $\Delta\dot{D} = 1\%$ and $\delta\ell = R_{CSDA}(E)/40$. Whereas, in case of macroscopic evaluation $\Delta\dot{D} = 1\%$ and $\delta\ell = 1\text{ mm}$ was considered. Also, in 3D dosimetry, the activity distribution was modeled as active voxels. The voxels located at the periphery and far from the active voxels (separated by more than 10 voxels) were not considered in the γ test.

2.2.4 General-purpose Monte Carlo codes

In order to avoid sources of differences beyond inherent codes' properties, the simulations were performed without using any variance reduction methods. The Geant4-DNA and EGSnrc simulations were performed using ubuntu 16.04 LTS Operating System installed in an AMD Ryzen 3 1200 Quad-Core Processor x 4 desktop with 8GB of memory, Fedora30 OS installed on i7core processor was used for FLUKA and PENELOPE. The MCNP6 simulations were performed in a OS Windows7 installed in a i7core with 16GB memory. The number of particles histories (NPS), computational time (CMT) and used cut-off for photons and electrons are reported in Table 2.1.

MCNP6

The origin of this lineage of codes known as Monte Carlo Neutron Particle - MCNP, dates from World War II [95]. Los Alamos National Laboratory (LANL) teams have been responsible for MCNP code development and updated the code. MCNP is currently in version 6, that is, MCNP6. It was originally designed to evaluate neutron interactions and energy deposition. Over time, routines for photons, electrons and other types of particles were included in the code. A new algorithm for electron transport, called single-event, was released with MCNP6 [92]. In recent work, the single-event algorithm showed better results than the condensed-history electron transport algorithms for 50 keV monoenergetic electrons using MCNP6 [96]. The authors did not test low energy electrons. However, the MCNP manual allows the electron cut-off to be defined as low as 10 eV [92]. In this work, the MCNP6.1.0 version single-event algorithm was used for electron transport. Thus, the EPRDATA12 photon library (.12p) must be used. Tally *F8 was used to estimate the energy deposition in the concentric shells to calculate the $sDPK$.

PENELOPE

PENELOPE (version 2014) [91] is a Monte Carlo software capable of simulating the transport of electrons, photons and positrons. Its algorithms make use of numerical databases and cross section models based on analytic approach to simulate different kind of interactions in energy range of 100 eV to 1 GeV. The standard and detailed simulation schemes are used to simulate photon transport, whereas charged particles are simulated implementing a mixed procedure that combined detailed and condensed approaches. Detailed simulation is performed for hard events by simulating the interactions by event-by event basis and condensed history based simulation is performed for soft events. Parameters C_1 , C_2 , W_{CC} and W_{CR} must be selected accordingly, for accurate and fast simulation. More detail about the simulation process and algorithm can be found in [91]. In this study $C_1 = 0.001$, $C_2 = 0.01$ parameters were used for simulating soft events such as elastic scattering. Furthermore, W_{CC} and W_{CR} were set to 100 eV in order to ensure the transport of all particles with energy above this value.

EGSnrc

EGSnrc is a general purpose Monte Carlo code capable of simulating the transport of electrons, photons and positrons in energy range of 1 keV to 1 GeV. It is specialized to simulate experiments related to radiation therapy and medical physics. It is divided into several modules to handle problems related to linear accelerators, voxelized cubical phantoms, brachytherapy etc. [46–49]. The electron-electron interaction are simulated using Moller cross sections and Bhabha cross sections are used to simulate electron-positron interactions [50]. The transport of electrons is simulated using mixed approach. Random sampling methods are used to simulate hard bremsstrahlung, hard inelastic collisions and annihilation interactions, where by the loss of energy is above the threshold value. Interactions where energy loss is lesser than threshold value are subjected to grouping. The concept of boundary crossing algorithm (BCA) is used to simulate the electron transport near the interfaces and heterogeneous mediums. Electrons crossing the boundaries are simulated using the single scattering (SS) mode. The distance at which BCA activates SS mode is resolved by ‘Skin depth for BCA’ parameter. In this study BCA was set to EXACT algorithm, skin depth for BCA = 3, Global AP = Global PCUT = 1 keV and Global AE = Global ECUT = 512 keV were used.

FLUKA

FLUKA is a Monte Carlo simulation package with fully integrated particle physics [84, 85] that makes use of a multiple scattering approach for charged particle transport, with a special algorithm [97] based on Molière’s theory improved by Bethe [98, 99]. The implemented transport algorithm provides robust independence from free path approximating by the sum of the many relative low energy losses in elastic and inelastic collisions (condensed history approximation). The 2011.2x.8 version of FLUKA was used for the scopes of the present work, setting defaults by the PRECISION card and implementing single scattering option. Threshold values for both particle energy production and transport were set to 1 keV for electrons and photons. Liquid water material is available in FLUKA material database. Electron bremsstrahlung is modeled in terms of the full set of Seltzer and Berger differential cross-sections. Photon cross-sections used in FLUKA are taken from the EPDL97 library [100].

Geant4-DNA

Geant4-DNA is a recent open-source code developed to simulate early biological damages caused by ionizing radiation at DNA level. It is an extension of Geant4, a general purpose Monte Carlo toolkit. It is provided within Geant4 and it uses the transport of particles such as electrons, protons, heavy ions, etc. simulating step by step within liquid water or constituents of DNA down to approximately 10 eV. All information about the physics processes, physics models and particles’ properties are included in physics constructor. The “G4EmDNAPhysics_option2,” “G4EmDNA Physics_option4,” and “G4EmDNAPhysics_option6” are the three physics constructors recommended by Geant4-DNA to simulate the transport of particles within liquid water [40]. These models handle the photon transport identically. However, they use different physics model to simulate the transport of electrons, protons, heavy ions etc. More details on the type of interactions and processes it supports can be found in [41, 44, 45, 40]. In present work Geant4 version geant4.10.05.p01, G4EmDNAPhysics_option2 physics constructor and liquid water as simulation medium were used.

2.3 Results and Discussions

2.3.1 In-water electron range

Figure 2.4(A) reports the results for electron range (R) calculated for point, isotropic and mono-energetic electron sources with initial energy 1, 5, 10, 15, 20, 25, 30, 40 and 50 keV. The calculations were performed using the methodology described in section 2.2.1 using the Monte Carlo codes: EGSnrc, FLUKA, GEANT4-DNA, MCNP6 and PENELOPE(2014). The comparison of calculated R values relative to the CSDA ranges provided in NIST [74] database is reported in Figure 2.4(B), which are also included in Table 2.2 up to 15 keV.

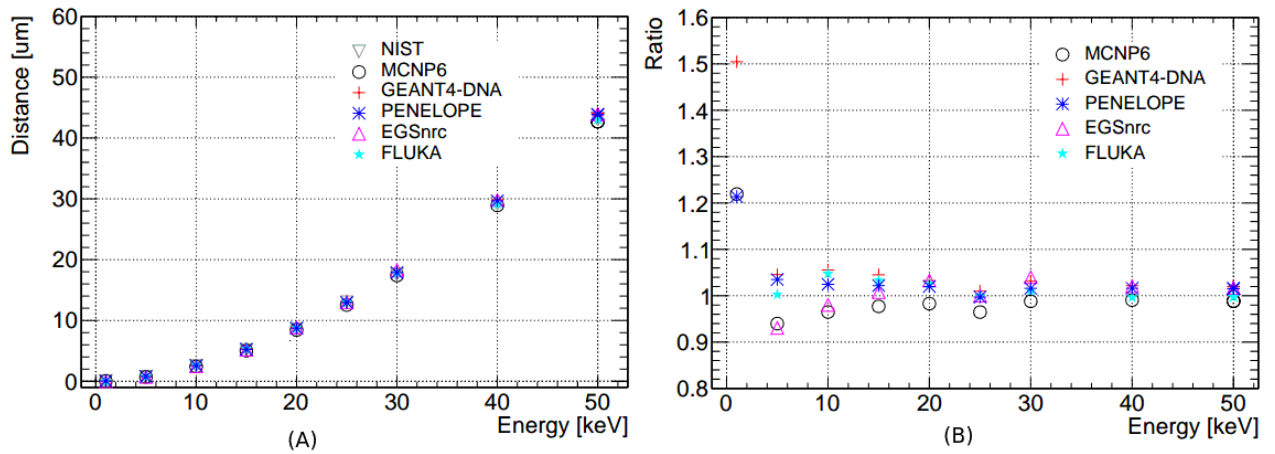


Figure 2.4 In-water range (R) (A) for different energies as calculated by EGSnrc, FLUKA, GEANT4-DNA, MCNP6 and PENELOPE(2014), along with NIST reference values. Figure (B) reports the range relative to NIST for all MC codes.

Figure 2.4 and Table 2.2 show that for all electron energies calculated with GEANT4-DNA presented the largest values. In comparison to NIST, GEANT4-DNA, MCNP6 and PENELOPE overestimated the electron range for 1 keV electron by 20% or more and deviations less than 10% were found for electron source with energy range between 5 to 50 keV and for all Monte Carlo codes. GEANT4-DNA overestimated the R value by about 5% for electron source with energy between 5-50 keV. PENELOPE, MCNP6, EGSnrc and FLUKA overestimated by about 5% for 5 keV electron source and the deviation of less than 5% in R value was observed for electron sources with initial energy 10-50 keV.

Table 2.2 Electron range R calculated using EGSnrc, FLUKA, GEANT4-DNA, MCNP6 and PENELOPE for mono-energetic electron sources with initial energy 1-15 keV. R values for 1 keV electron source were not calculated using EGSnrc and FLUKA.

Energy[keV]	NIST [um]	MCNP6 [um]	EGSnrc [um]	GEANT4-DNA [um]	PENELOPE [um]	FLUKA [um]
1	0.04	0.05 (-21.92%)		0.06 (-50.45%)	0.05 (-21.37%)	
5	0.75	0.70 (6.01%)	0.69 (6.94%)	0.78 (-4.54%)	0.77 (-3.48%)	0.75 (-0.27%)
10	2.52	2.43 (3.52%)	2.47 (1.98%)	2.66 (-5.56%)	2.58 (-2.46%)	2.64 (-4.76%)
15	5.15	5.03 (2.29%)	5.19 (-0.78%)	5.38 (-4.50%)	5.26 (-2.17%)	5.32 (-3.30%)

The values in brackets represent the approximate percentage deviation of calculated range value in comparison to NIST database.

On average the calculated R values were in good agreement with the CSDA range values given in NIST database. And, the overestimation in range by GEANT4-DNA was also reported by [52]. It is worth noting that electron energy cut-off of 100 eV was used in GEANT4-DNA, MCNP6 and PENELOPE, only for 1 keV electron source, as reported in Table 2.1; whereas it was set to 1 keV for EGSnrc and FLUKA. The discrepancies found for R estimations may be due to the difference in energy cut-off used or they may arise directly from the different physics models and transport algorithm particularities found in these Monte Carlo codes.

The net travelled distance until "loosing" 50% of initial kinetic energy (R_{50}) is depicted in Figure 2.5(A), as obtained by the different MC codes. Also, considering R_{50} calculated using PENELOPE as reference value (RV), the deviation of other MC codes with respect to PENELOPE is reported in Figure 2.5(B). For 5-50 keV the GEANT4-DNA, FLUKA, MCNP6 and EGSnrc calculated R_{50} deviated by upto 8% in comparison to PENELOPE. Largest deviation (greater than 5% for electron sources of 5, 10, 15, 20 keV) with respect to RV was observed for GEANT4-DNA. For other MC codes all deviations were less than 5%.

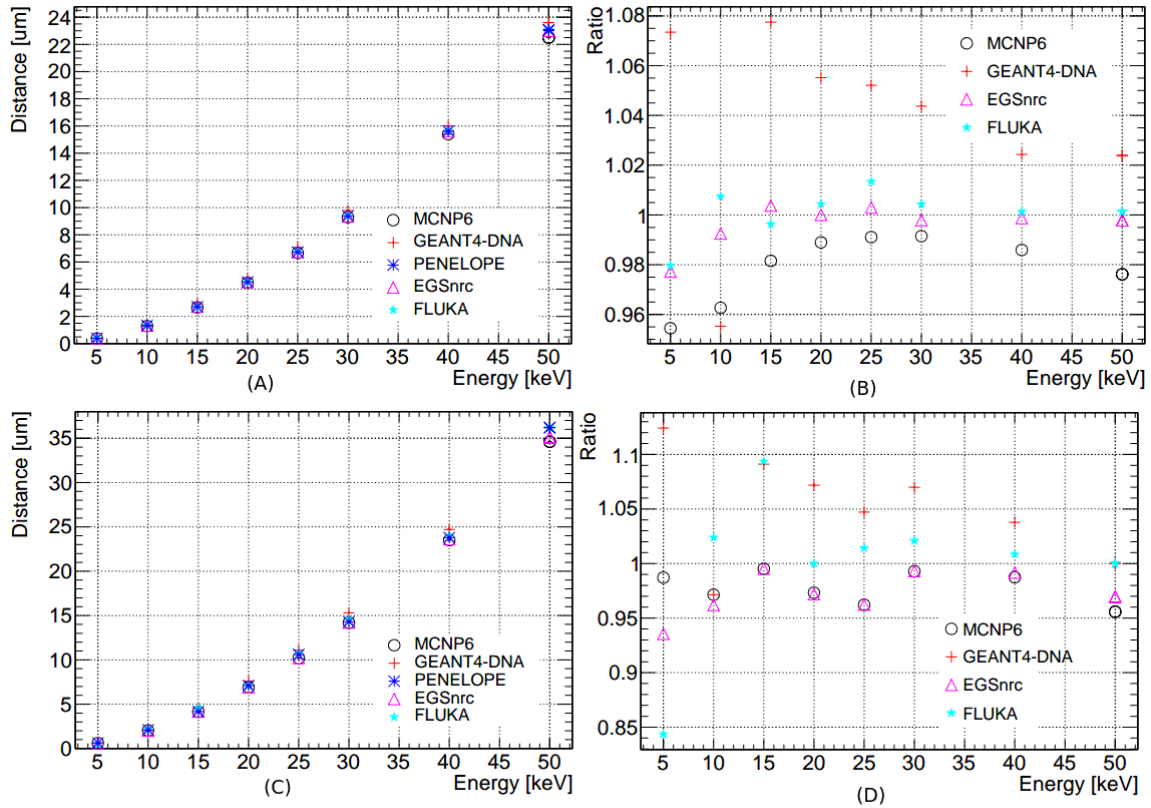


Figure 2.5 In-water R_{50} (A, B) R_{90} (C, D) and Ratio (with respect to PENELOPE) for different electron energies calculated using EGSnrc, FLUKA, GEANT-DNA, MCNP6 and PENELOPE.

Figure 2.5(C) reports R_{90} which is defined as the depth at which 90% of initial kinetic energy of the electron is lost. Also, the comparison of calculated R_{90} with respect to RV is reported in Figure 2.5(D). The deviation of up to 20% with respect to RV is observed for the R_{90} calculated for electron source with initial energy of 5 keV. Remaining all deviations were less than 10%. Similar to R_{50} here also GEANT4-DNA was found deviating by 10% for 5, 10, 15 and 20 keV electron energy sources. Whereas, for all other MC codes the deviation with respect to RV was up to 5%.

According to the reported results for R , R_{50} and R_{90} , it can be summarized that (a) largest variations between the MC calculated values was observed for electron source of 5 keV; R (7%), R_{50} (10%) and R_{90} (20%). (b) Deviation of less than 10% was observed for 10-50 keV electron sources. This variation between different MC codes for computed R , R_{50} and R_{90} can be result of difference in algorithms used to simulate the transport of low electron by the MC codes. Also, the least deviation between the MC codes was observed for the calculated R

values. Hence, it can be suggested as a suitable option to define the range of electron sources.

2.3.2 Scaled Dose point kernel calculation

Figures 2.6 and 2.7 report the scaled dose point kernels (*sDPK*) obtained by the different MC codes using the methodology described in section 2.2.2. *sDPK* values were calculated for electron source with energies of 1, 5, 10, 25 and 50 keV. The shape of the curve plotted for the point kernel values obtained from all MC codes was in good agreement. For 1 keV electron source, the *sDPK* was simulated using GEANT4-DNA, MCNP6 and PENELOPE codes, see Figure 2.6 (A); whereas for other electron sources comparison was performed among all the MC codes. The largest deviation in the calculated *sDPK* by different MC codes was observed for 1 keV and best agreement for 50 keV, as expected, see Figure 2.7. For 1 keV electron source the *sDPK* peak is closer to the point source. For GEANT4-DNA, approximately at $0.4 r/R_{CSDA}$, followed by MCNP6, at $0.5 r/R_{CSDA}$ and then by PENELOPE, between 0.5 and 0.6. On the other hand, for all MC codes the *sDPK* peak for 5, 10, 25 and 50 keV were found between 0.5 up to $0.6 r/R_{CSDA}$. Similar behavior for *sDPK* of 10 keV was previously reported by [77], where *sDPK* comparisons between PENELOPE, ETRAN, GEANT4 and MCNP6 are reported.

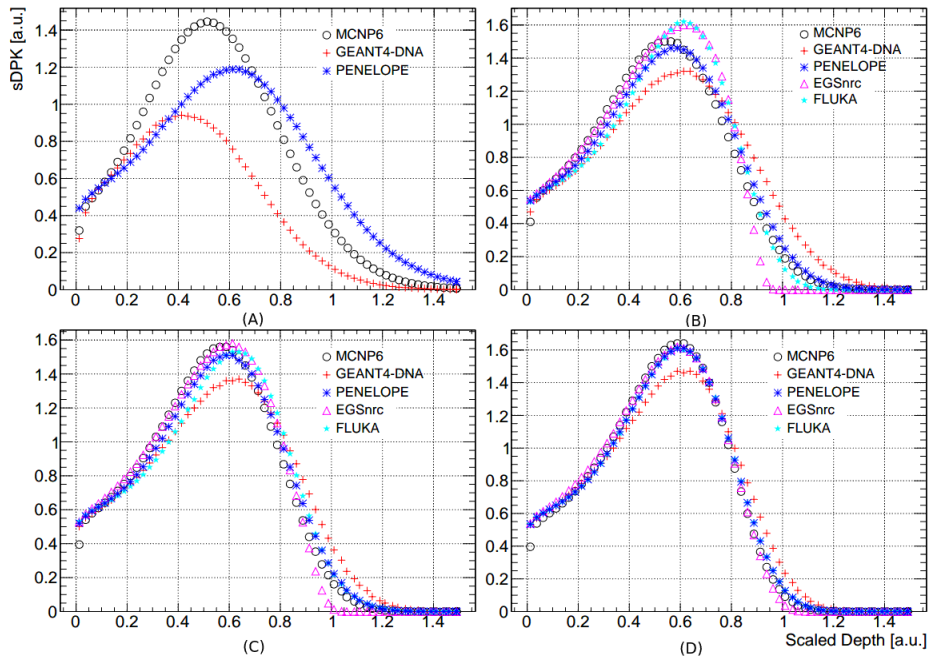


Figure 2.6 1 keV (A), 5 keV(B), 10 keV (C) and 25 keV(D) in-water *sDPK* obtained with different PENELOPE, GEANT4-DNA, EGSnrc, FLUKA and MCNP6 Monte Carlo codes.

The *sDPK* maximum value for 1 keV was 1.5 for MCNP6, between 1 and 1.5 for PENELOPE and less than 1 for GEANT4-DNA. For all other electron energies, the maximum *sDPK* value obtained was approximately at 1.5 for all MC codes. The maximum of GEANT4-DNA calculated *sDPK* value was slightly lower than 1.5 in all cases. Similar behaviour has been reported by [52]. For 1 keV electron source, PENELOPE deposited energy further away compared to MCNP6 and GEANT4-DNA. Finally, for GEANT4-DNA 5, 10, 25 and 50 keV electrons deposited more energy further away from the source in comparison to other codes. Hence, different physics models and transport algorithms lead to non-negligible differences in in-water *sDPK* assessment for low energy electrons. It is important to understand that the difference found for low energy electrons sources lead to appreciable differences in dosimetry only at microscopic scale; whereas typical/standard clinical applications, which use voxel size around 1 mm^3 , or larger, are not significantly affected due to differences in short-distance terms, as happens for in-water low-energy electron range.

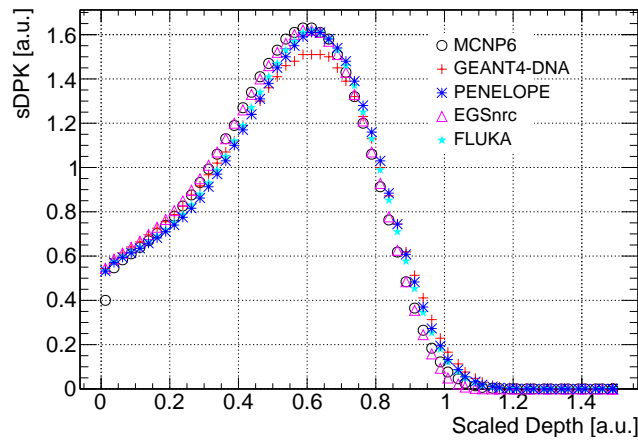


Figure 2.7 50 keV in-water *sDPK* obtained with PENELOPE, GEANT4-DNA, EGSnrc, FLUKA and MCNP6 MC codes.

As can be observed in the reported Figures, the largest differences between the MC codes were observed for 5 and 10 keV electron energies and quite negligible differences were observed in *sDPK* for 25 and 50 keV electrons.

2.3.3 Applications to 3D dosimetry

Two approaches were considered to calculate the 3D absorbed dose rate using the kernel convolution regards the ensemble of the 3D kernel \mathbf{K} in terms of the radial *sDPK*, as described in section 2.2.3 and Equation 2.4. First, aimed to calculate at the microscopic scale level and second at the macroscopic, clinical case. Figure 2.8 reports a representative example of the 3D kernel \mathbf{K} as constructed using the *sDPK* obtained with the PENELOPE MC code for electrons with 50 keV as initial kinetic energy. Similar 3D kernel \mathbf{K} was constructed using *sDPK* obtained from other MC codes for electron sources with different energies.

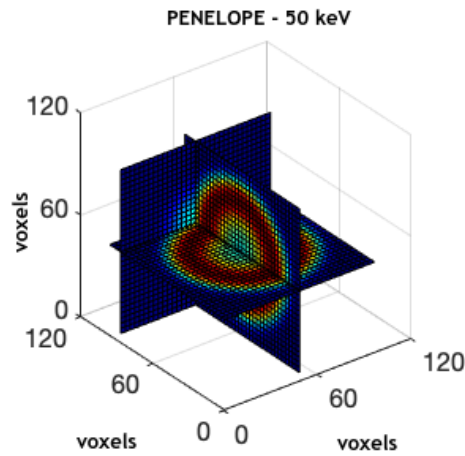


Figure 2.8 Representative example of voxelized 3D kernel \mathbf{K} as obtained in terms of 50 keV $sDPK$ for PENELOPE code.

3D dosimetry at microscopic level

Figure 2.9 reports the corresponding absorbed dose rate profiles along the central axis, as obtained for the different MC codes.

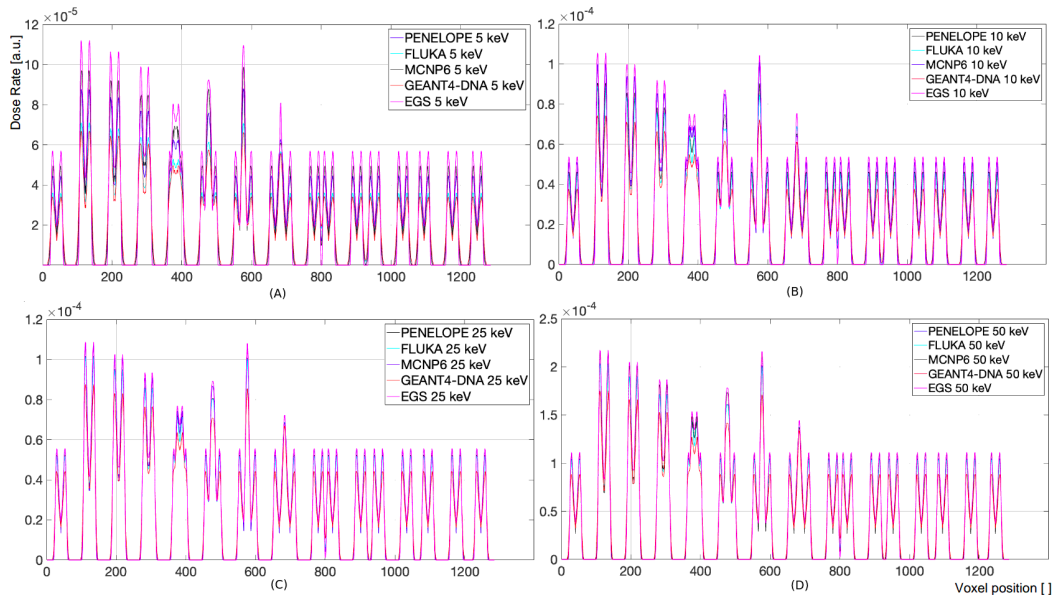


Figure 2.9 Absorbed dose rate profiles obtained by the different MC codes for 5 (A), 10 (B), 25 (C) and 50 keV (D).

Although comparisons by 1D profiles and 2D (not shown) isodose (rate) contour levels are helpful for assessing dosimetry similarities/differences, Table 2.3 reports the corresponding

percentage of voxels passing the γ -test, when considering the PENELOPE distribution as the reference.

Table 2.3 Percentage of passing voxels according to 3D γ -test obtained when comparing the absorbed dose rate distribution at microscopic scale corresponding to different general-purpose Monte Carlo codes using PENELOPE as reference and fixing tolerance to $\Delta\dot{D} = 1\%$ and $\delta\ell = R_{CSDA}(E)/40$.

Energy E [keV]	FLUKA	EGSnrc	GEANT4-DNA	MCNP6
5	> 65 %	> 76 %	> 61 %	> 63 %
10	> 79 %	> 81 %	> 74 %	> 76 %
25	> 83 %	> 84 %	> 80 %	> 82 %
50	> 88 %	> 87 %	> 85 %	> 87 %

3D dosimetry at macroscopic level: application in nuclear medicine

Figure 2.10 summarizes the corresponding absorbed dose rate profiles along the central axis, as calculated for the different MC codes.

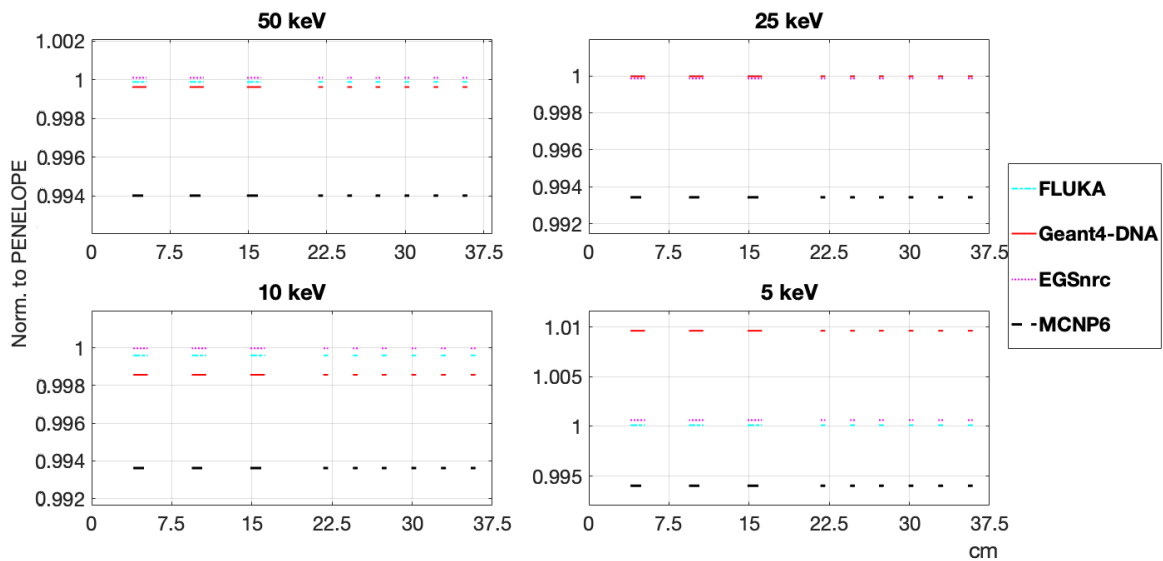


Figure 2.10 Absorbed dose rate profiles obtained by the different MC codes for 50, 25, 10 and 5 keV.

For a better assessment of quantitative comparisons, Table 2.4 summarizes the percentage of passing voxels according to the gamma index γ , when considering the PENELOPE distribution as the reference.

Table 2.4 Percentage of passing voxels according to 3D gamma index γ obtained when comparing the absorbed dose rate distribution at macroscopic scale corresponding to different MC codes using PENELOPE as reference and fixing tolerance to $\Delta\dot{D} = 1\%$ and $\delta\ell = 1\text{ mm}$.

Energy [keV]	FLUKA	EGSnrc	GEANT4-DNA	MCNP6
5	> 99 %	> 99 %	> 99 %	> 99 %
10	> 99 %	> 99 %	> 99 %	> 99 %
25	> 99 %	> 99 %	> 98 %	> 99 %
50	> 98 %	> 98 %	> 98 %	> 98 %

According to typical clinical criteria for complex modern radiotherapy techniques, like intensity modulated radiotherapy (IMRT), 90 % of voxels passing the γ index with $\Delta D = 3\%$ and $\delta\ell = 1\text{ mm}$ is considered as an acceptable performance [94]. As reported by Table 2.4, the differences between the general-purpose Monte Carlo codes found for the electron range at low energies that impacted on the corresponding $sDPK$ do not affect significantly the macroscopic 3D absorbed dose rate distributions. This result might be expected for the clinical case, because voxel size is significantly larger than low-energy electron ranges, and therefore all the energy emitted by corresponding transitions/decay remain within the volume of the active voxel.

It is worth mentioning that the results obtained by the general-purpose Monte Carlo codes provide differences in-water range values for low-energy electrons, and therefore these differences impact, subsequently, on the corresponding dose point kernels $sDPK$. The effect of differences in the obtained range values and $sDPK$ profiles is visible in absorbed dose rate profiles obtained on performing 3D dosimetry. The dose rate profiles obtained at the microscopic level were found deviating from each other. Whereas, negligible differences were observed in the profiles obtained at the macroscopic level, where voxel size was larger than $R_{CSDA}(E)$, see Table 2.3 and Table 2.4. Hence, special care should be taken when modelling microscopic dosimetry applications [101, 102], or situations, like dose due to secondary Auger or Coster-Kronig electrons, as required for nano-particle applications [103–105].

2.4 Conclusions

In this work, in-water electron tracks was studied for initial kinetic energy from 1 up to 50 keV. Besides this, scaled dose point kernels, as required for internal dosimetry in nuclear medicine, were calculated as a practical nuclear medicine application example. Subroutines were successfully adapted to these aims for the well-known MCNP6, PENELOPE, EGSnrc and FLUKA Monte Carlo codes, as well as for the more recent Geant4-DNA code. Results

obtained for all five MC codes for electron range and *sDPK* showed an overall similar trend, thus suggesting their suitability for these purposes. Although the different general-purpose Monte Carlo codes provide different in-water range values for low-energy electrons, these differences do not propagate significant deviations at macroscopic dosimetry level, as commonly required for standard clinical applications. Contrary, the initial differences in low-energy electron range showed to impact non-negligibly on dosimetry calculations at microscopic level, as would be expected.

2.5 Acknowledgments

The following Brazilian institutions support this research project: Research Support Foundation of the State of Minas Gerais (FAPEMIG), Brazilian Council for Scientific and Technological Development (CNPq) and Coordination for the Capacitation of Graduated Personnel (CAPES). Prof. Telma C. F. Fonseca is grateful for financial support provided by CNPq (processo n° 450493/2019-9) and FAPEMIG (Projeto APQ-00083-18 Processo n° 2070.01.0002992/2018-30). Official license to FLUKA and PENELOPE Monte Carlo main codes are addressed to Prof. M. Valente as NEA liaison officer for Argentina and region, MCNP6 to Dr. B. M. Mendes, EGSnrc and Geant4DNA to Telma C. F. Fonseca, PhD.

2.6 Addendum

In section 2.3.3 gamma index γ , proposed by Low et al. [93], was used to perform quantitative comparisons between the estimated 3D dose rate distributions using several MC codes. However, for the 3D dosimetry reported in this chapter, γ index is not a correct tool to perform quantitative comparison. It is because γ index was designed to to perform quantitative comparison between the treatment planning system calculated dose (CD) distribution and experimentally measured dose (MD) distribution. Where MD distribution is used as the reference, and the CD distribution is checked for comparison. Furthermore, the dose to distance agreement (DTA) parameter is used to compare the distance between the MD point and CD point. While comparing the experimental and calculated dose distribution, the use DTA is mandatory because of the difference in the phantom setup during experimental measurements with respect to the calculations. Whereas, while comparing the dose distribution calculated using MC codes. The differences between the phantom setup can be eliminated and the use of γ index or DTA for quantitative comparisons in not correct. Hence, the use of γ index, for cases similar to that reported in this chapter, should be prohibited and the quantitative comparisons must be performed in terms of dose rate ratio.

Chapter 3

Calculation of dose point kernel values for monoenergetic electrons and beta emitting radionuclides: intercomparison of Monte Carlo codes

Bruno Melo Mendes^{1,*}, Paula Cristina Guimarães Antunes², Isabela Soares Lopes Branco², Eduardo do Nascimento³, Baljeet Seniwal⁴, Telma Cristina Ferreira Fonseca⁴, Helio Yoriyaz²

¹Centro de Desenvolvimento da Tecnologia Nuclear, CDTN. Av. Presidente Antônio Carlos, 6.627 Campus da UFMG – Pampulha; 31270-901; Belo Horizonte - Minas Gerais, Brasil.

²Instituto de Pesquisas Energéticas e Nucleares, IPEN, 05508-000. São Paulo, SP, Brasil.

³Universidade Federal da Bahia, UFBA, Instituto de Humanidades, Artes e Ciências, IHAC, 40170-110. Salvador, BA, Brasil.

⁴Departamento de Engenharia Nuclear - Universidade Federal de Minas Gerais, Av. Antônio Carlos, 6.627, Pampulha, 31270-901, Belo Horizonte, MG, Brasil.

Corresponding author: Bruno Melo Mendes (bmm@cdtn.br)

Journal name: Radiation Physics and Chemistry Journal.

Citation: Mendes, B. M., Antunes, P. C. G., Branco, I. S. L., do Nascimento, E., Seniwal, B., Fonseca, T. C. F., Yoriyaz, H. (2021). Calculation of dose point kernel values for monoenergetic electrons and beta emitting radionuclides: Intercomparison of Monte Carlo codes. Radiation Physics and Chemistry, 181, 109327.

Abstract

Targeted radionuclide therapy (TRT) and beta-emitting seeds brachytherapy (BSBT) exploit the characteristics of energy deposited by beta-emitting radionuclides. Monte Carlo (MC) modelling of electron transport is crucial for calculations of absorbed dose for TRT and BSBT. However, computer codes capable of providing consistent results are still limited. Since experimental validations show several difficulties, the estimation of electron dose point kernel (DPK) is often used to verify the accuracy of different MC codes. In this work, we compared DPK calculations for various point, isotropic and monoenergetic electron sources and several beta-emitting radioisotopes using the codes MCNP, EGSnrc, PENELOPE and TOPAS with different simulation options. The simulations were performed using latest versions of EGSnrc and Penelope, TOPAS version 3.3.1 and MCNP version 6.1 Monte Carlo codes. In our simulations, the geometrical model consists of a point electron source placed at the center of a water sphere emitting isotropically. The water sphere was divided into 28 shells and the energy deposition was scored within these shells. The radius of the outermost shell was $1.2 R_{CSDA}$, where R_{CSDA} is the continuous slowing down approximation (CSDA) range. Five monoenergetic beta sources with energies of 0.05, 0.1, 0.5, 1 and 3 MeV were studied. Six beta-emitting radionuclides were also simulated: Lu-177, Sm-153, Ho-166, Sr-89, I-131 and Y-90. Monoenergetic electron simulations showed large deviations among the codes, larger than 13% depending on the electron energy and the distance from the source. In the cases where beta spectra of radionuclides were simulated, all MC codes showed differences from EGSnrc (used as reference value - RV) less than 3% within r_{E90} range (radius of the sphere in which 90% of the energy of the spectrum electrons would be deposited). TOPAS showed results comparable to EGSnrc and PENELOPE. DPK values for 0.1 MeV monoenergetic electrons, calculated using MCNP6, led to differences higher than $\pm 5\%$ from RV despite our attempts to tune electron transport algorithms and physics parameters.

Keywords: Targeted radionuclide therapy, Beta-emitting seeds Brachytherapy, Electron DPK, MC code intercomparison.

3.1 Introduction

Radiation therapies involving the use of beta particle emitting radionuclides have been widely studied and used. Targeted radionuclide therapy (TRT) and beta-emitting seeds brachytherapy (BSBT) are the examples of techniques that take advantage of the characteristic energy deposition of this type of particle [106–109].

TRT uses high affinity carriers to selectively deliver radionuclides to tumor cells [106, 110]. Several types of carriers have been used, including: antibodies, antigens, liposomes, carbon nanotubes, aptamers, microspheres, specific molecules and nanoparticles [106, 111, 112, 109, 60, 113]. In some cases, the radionuclide itself has affinity for tumor tissues, for instance the Iodine and the thyroid gland. Among the beta emitters conjugated to tumor-seeking macromolecules are Sr-89, Y-90, I-131, Sm-153, Ho-166 and Lu-177 [106, 111, 112, 109, 110], covering a range of energy from few keV to 2.28 MeV (ICRP, 2007). Dosimetry is very important in TRT to determine dose deposition within the tumor volume and organs at risk, i.e., treatment planning and follow up. In addition, it has an important role in microdosimetric studies to evaluate the efficiency of a group radionuclide/carrier based on the dose accumulation pattern within the cell [114–117].

The first reported use of BSBT using seeds produced from biocompatible glass was in the early 2000s [118, 119]. This technique is based on the principle of depositing large amounts of energy in the close proximity (few millimeters) of the radiation source by high energy beta particles in comparison to the photon emitters currently used in brachytherapy. Thus, high dose can be deposited within the tumors and healthy tissues can be spared. Initially, the use of Sm-153 was proposed [119]. Since then, the use of different high energy beta emitters such as Pr-142, Y-90, Re-188, Ho-166 and Sr-89, have been evaluated [120–123, 107, 108]. Clinical studies of BSBT have not yet been reported. Dosimetric studies for optimization of seed distribution within tumor volumes and determination of AAPM TG-60 parameters, including reference dose rate, radial dose function and anisotropy function, are required for clinical evaluation of BSBT.

Accurate absorbed dose estimation, which usually is based on Monte Carlo modelling of electron transport, is critical for proper disease control, minimizing the risk of radiation induced deterministic effects for both TRT and BSBT. However, computer codes capable of providing reliable results are still scarce and depend on reliable atomic data and cross-sections. Several electron transport models have been made available along the years by different computer code developers such as Geant4 [34], MCNP6 [35], PENELOPE [36, 37],

TOPAS [38], EGSnrc [39] and PHITS [124].

The MCNP code, up to the MCNPx version, provided the well-known condensed-history method (CHM) for simulating electron transport [125]. In MCNP6 the single event (SE) algorithm was also introduced, which considers individual electron collisions [35]. Other Monte Carlo (MC) codes can also use SE algorithms. PENELOPE [37] code can use either CHM or SE, following a predetermined threshold of energy loss defined by the user. EGSnrc [39] uses a single scattering mode near the boundaries for accurate simulations. EGSnrc is recognized to be a very stable and electron-transport artifact free code [126]. In 2012, TOPAS MC code [38] was launched with applications in medical physics. This code is a wrapper and extension to Geant4, designed with a particular usefulness in proton transport problems considering all secondary particles including neutrons, photons and electrons.

In nuclear medicine, dose point kernel (DPK) is used to verify the accuracy of dosimetric calculations performed using different computer codes. For the calculations, a point, isotropic radioactive source placed at the center of the spherical water phantom and DPK is estimated at different points along the radius of the phantom. Some studies on comparison of electron DPK, calculated using different codes, can be found in literature [96, 53, 127, 52, 128, 129, 126]. However, these usually compare only two codes [96, 126]. Furthermore, the electron transport models and algorithms used are now outdated [53, 52, 126]. In this study, we calculated DPK for various point, isotropic and monoenergetic electron sources and several radioisotopes with potential use in nuclear medicine using the codes: MCNP6, EGSnrc, PENELOPE and TOPAS with different and updated simulation options provided by the updated version of the codes. DPK was calculated in spherical shells composed of water with variable thickness according to electron energy.

3.2 Materials and methods

3.2.1 DPK calculation model

The geometrical model consisting of an isotropically emitting, point electron source placed at the center of a water sphere was used. The water sphere was divided into 28 shells and the energy deposition was computed within these shells. The radius of the outermost shell was $1.2R_{CSDA}$, where R_{CSDA} is the continuous slowing down approximation (CSDA) range

corresponding to the energy of the monoenergetic electron sources and the maximum energy of the betas emitted by the radionuclides. Five monoenergetic beta sources with energies of 0.05, 0.1, 0.5, 1.0 and 3.0 MeV were studied. Six beta-emitting radionuclides were also investigated: Lu-177, Sm-153, Ho-166, Sr-89, I-131 and Y-90. Figure 3.1 shows the model used for the simulations. Table 3.1 reports the average energy of each radionuclide along with the R_{CSDA} and thickness of the shells. The beta emission spectra of the radionuclides was taken from [130]. Electron fluence within the shells were also obtained for monoenergetic electrons.

Based on the work of Antoni and Bourgois in 2017 [96], the dose-point kernel is defined as:

$$DPK(r) = D(r) \cdot 4\pi r^2 \cdot \rho \cdot \frac{R_{CSDA}}{E} \quad (3.1)$$

where $D(r)$ is the absorbed dose in MeV/g; r is the radial distance in cm; R_{CSDA} is the electron CSDA range in cm; ρ is the water density in g/cm^3 ; E is the electron energy in MeV.

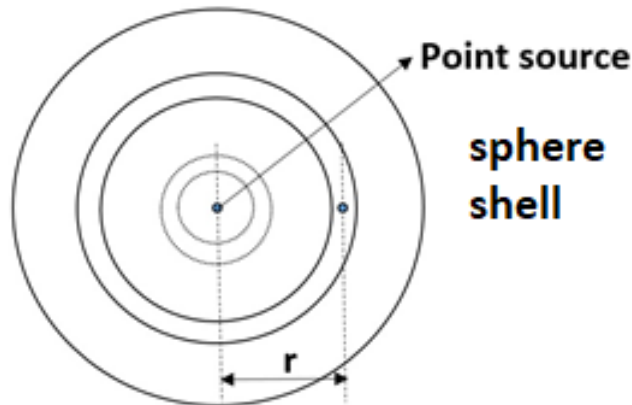


Figure 3.1 Geometric model for the simulation. A water sphere composed of multiple shells, varying in radius, where DPK is calculated.

Table 3.1 Energy, R_{CSDA} and, shell thickness for the cases simulated in this work.

Electron Simulated	Avg./Max. Energies (MeV)	R_{CSDA} (cm)	Shell Thickness (cm)	
monoenergetic	0.05/0.05	0.0043	0.0000864	
	0.1/0.1	0.0143	0.0002862	
	0.5/0.5	0.1766	0.0035320	
	1/1	0.4367	0.0087340	
	3/3	1.5140	0.0302800	
Spectrum	Lu-177	0.133/0.498	0.1755	0.003511
	I-131	0.182/0.807	0.3363	0.006725
	Sm-153	0.228/0.808	0.3369	0.006739
	Sr-89	0.584/1.492	0.7048	0.014097
	Ho-166	0.668/1.854	0.8994	0.017987
	Y-90	0.935/2.280	1.1289	0.022577

3.2.2 Monte Carlo codes

MCNP6

Five different routines were used to calculate DPK using MCNP6.1. code version [35]. First four routines were based on the default MCNP6 condensed-history algorithm (Landau straggling), varying the EFAC and ESTEP parameters. EFAC controls the spacing of the stopping power energy grid, i.e., the step size. ESTEP controls the number of sub-steps. The sub-step is the level at which the angular deflection and the production of secondary particles are sampled [35].

First CH routine, named as CHdd, used default values for ESTEP (3, for water) and EFAC (0.917). The second routine (CHed) used the default ESTEP value and EFAC increased to 0.99. In the third routine, CHee, EFAC was set to 0.99 and ESTEP parameter was increased according to the methodology described in MCNP5 manual [125] such that an electron should make at least ten sub-steps in any shell it enters. The fourth routine, CHee+, maintained EFAC = 0.99 and the methodology used to calculate ESTEP resulted in values an order of magnitude higher than ones that were obtained for CHee mode. The details of the methodology used to calculate ESTEP and values obtained in each case are presented in the supplementary file.

The fifth routine, named as SE, uses the single event electron transport algorithm. Such an algorithm, completely different from CH electron transport, is based on direct sampling of mi-

cross section data and is designed to improve the accuracy of low-energy electron transport [131].

For all the five routines, cross sections from ENDF/B-VI release 8 photon/electron-atomic and relaxation data for H and O were used. The energy deposition by electrons within the target volumes (the 28 shells) were scored using Tally *F8. The DPKs were calculated for all five routines (described above). The results of the routine which showed the best match with the reference value (see section 3.2.3) are plotted in the graphics.

TOPAS

TOPAS [38] is a wrapper and extension of the GEANT4 [34] Monte Carlo code. It is specialized for simulation of radiotherapy problems. The code allows modeling the LINACs heads and geometry of patients based on tomography (CT) images. It can also incorporate movements, related to the gantry and the geometry of the patient, to perform 4D calculations. Initially, this code was designed for use in proton therapy, but today its application extends to all radiation therapies, and there are also drafts of future versions for including radiobiology parameters and calculations. The simulations were performed using version 3.1.1. of TOPAS, default modular physics list and the energy cut off for electrons and photons was set to 50 eV.

PENELOPE

PENELOPE [78] MC code allows the transport of electrons, positrons and photons with energy from a few hundred eV to about 1 GeV, in complex geometries and materials of varied chemistry composition. PenEasy [132] is a general-purpose main program for PENELOPE. It includes a set of source models, tallies and variance-reduction techniques that are invoked from a structured code. PENELOPE is a class II code, i.e., positron and electron interactions are simulated using a mixed approach. The event-by-event detailed simulation is performed for hard events and the condensed-history based simulation approach is used for soft interactions. In the present work, the PENELOPE 2018 version associated with PenEasy 2019-09-26 code version was used. The energy cut off for electrons, positrons and photons was set to 50 eV and the simulation parameters that were used for electron and positron transport for condensed-history are $C1 = C2 = 0.1$, $WCC = WCR = 50$ and $DSMAX = 1030$.

EGSnrc

EGSnrc [39] is an updated version of the Monte Carlo software Electron Gamma Shower (EGS) for clinical purposes [47, 133, 46]. It can simulate the transport of electrons, positrons and photons in the energy range of 1 keV to 1 GeV, within the homogeneous medium. Mixed approach is used to simulate the transport of electrons. Interactions (such as hard bremsstrahlung, hard inelastic collisions, and annihilation) with energy losses greater than the threshold are treated by conventional random sampling. Whereas, sub-threshold interactions such as soft bremsstrahlung emission, soft inelastic collision and elastic scattering are subjected to grouping [50]. To accurately simulate the transport of electrons in heterogeneous medium or near the interfaces the boundary crossing algorithm (BCA) is used. In this work, the default EXACT algorithm was used as BCA and skin depth for BCA was set to 3. This algorithm activates single scattering (SS) mode to simulate the transport of electrons while crossing the boundaries. The distance from the boundary at which the SS mode is activated is resolved by the ‘Skin depth for BCA’ parameter. The energy cut off for electron transport was set to 1 keV.

3.2.3 Code comparison and data analysis

The DPK curves obtained with the EGSnrc MC code were considered as reference values (RV) in order to facilitate the comparison among the codes. A gray area comprising $\pm 3\%$ interval of the EGSnrc curves was included in each graphic.

Simulation relative errors in the outermost shells could be higher than 3%. Thus, the comparisons were restricted from DPK values in the 0 to $0.9R_{CSDA}$ range in the monoenergetic cases. For radionuclide spectra cases, we compared the DPK data up to r_{E90} value, which corresponds to the radius of the sphere in which 90% of the energy of the spectrum electrons would be deposited.

3.3 Results and Discussion

DPK curves obtained for monoenergetic, point and isotropic electron sources with energy 0.05, 0.1, 0.5, 1 and 3 MeV are shown in Figure 3.2. The comparison of the codes was restricted to the DPK values in the $0.9R_{CSDA}$ range (see section 3.2.3).

PENELOPE data was found in the best agreement with the EGSnrc DPK values (RV).

For all points lower than $0.65 R_{CSDA}$, the differences are within $\pm 3\%$ range for all electron energies. TOPAS code also showed a good agreement with RV for 0.1 to 1.0 MeV electrons. However, TOPAS DPK values for 0.05 MeV and 3.0 MeV electrons showed a greater number of points out of the $\pm 3\%$ range. All codes agree with RV within $\pm 5\%$, except MCNP6 for 0.1 MeV electrons and TOPAS for 3.0 MeV electrons.

The results obtained with MCNP6 code varied considerably depending on the simulation parameters. SE routine matches very well with the RV (within $\pm 5\%$) for 0.05 MeV electrons, but for higher energies such as 0.1, 0.5, 1.0 and 3.0 MeV, the discrepancies increase with increase in the source energy ($> \pm 10\%$; $> \pm 50\%$; $> \pm 90\%$; $> \pm 130\%$; respectively). This behavior was also reported by Antoni and Bourgois [96] and Poskus [134]. According to Poskus (2016) these discrepancies are caused by the lack of data for angular distribution of elastic scattering in the ENBF/B library. In this case, the linear interpolation of the angular distribution table could cause overestimation of electron backscattering process resulting in a backward shift of the DPK curve.

MCNP6 DPK results obtained using the condensed-history method (CHM) algorithm showed good agreement with EGSnrc, TOPAS and PENELOPE for 0.5, 1.0 and 3.0 MeV monoenergetic electron energies. All differences were less than $\pm 7\%$, $\pm 6\%$ and $\pm 5\%$ for these energies, respectively, except for 3.0 MeV using CHee+ ($> 20\%$). Values closer to RV were obtained with CHee routine for 0.5 MeV (4.0% to -1.4%). For 1.0 MeV and 3.0 MeV electrons, CHed routine obtained values closer to RV: (1.5% to -2.0%) and (1.1% to -1.1%) respectively. For lower energies (such as 0.05 and 0.1 MeV), CH algorithm diverges considerably near the DPK peak.

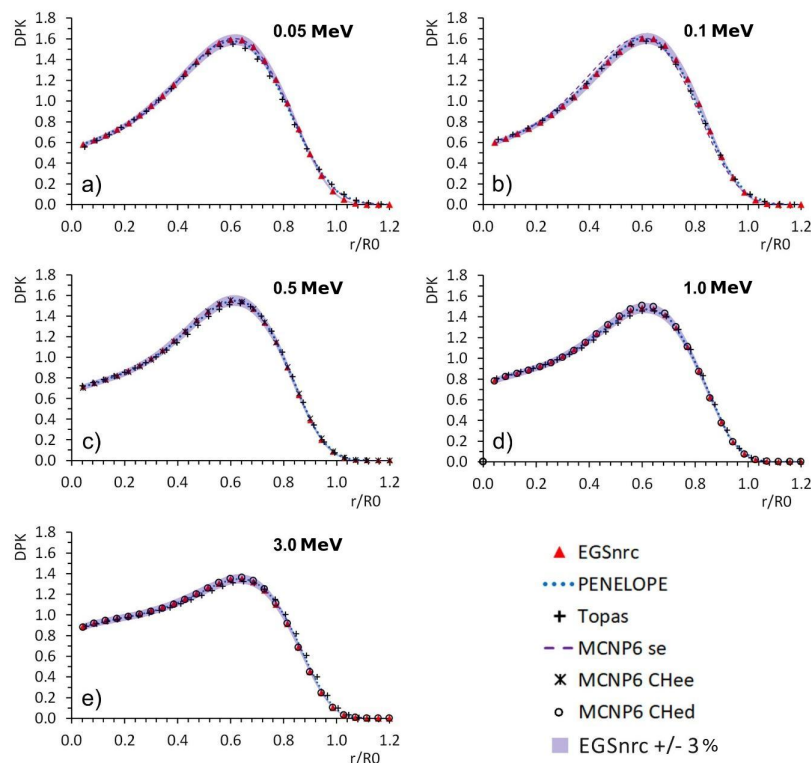


Figure 3.2 DPK curves for monoenergetic electron point sources of: a) 0.05, b) 0.1; c) 0.5; d) 1 and e) 3 MeV. The gray area comprises $\pm 3\%$ of the EGSnrc curves.

Considering only the CH routines, the increase of ESTEP values and EFAC resulted in DPK closer to RV for 0.05 MeV (CHee), 0.1 MeV (CHee+) and 0.5 MeV (CHee or CHee+). Although, for the two first electron energies, the Single-Event algorithm is preferable. Increasing ESTEP and EFAC for 1.0 MeV and 3.0 MeV electrons did not improve the results and considerably increased the computational time. In this regard, the CHdd mode had the lowest computational times per particle history. CHee and CHee+ had, on average, computational times approximately 12x and 85x higher than CHdd, respectively.

Still about MCNP6, none of the MCNP routines for electron transport, tested for the geometry proposed in this work, show results within $\pm 5\%$ of RV for 0.1 MeV monoenergetic electrons. The SE algorithm presented DPK results closer to the RV than CH algorithms. However, many points were left out of the EGSnrc $\pm 3\%$ range (Figure 3.2 (b)). Thus it is important to tune of the electron transport parameters for 0.1 MeV monoenergetic electrons. In fact, for 0.1 MeV electrons, we tested three more routines keeping default value for EFAC and ESTEP parameter was varied. However, the attempts to tune the electrons transport parameters failed to obtain DPK values closer to RV than SE routine. The effect of change in the energy cutoff value was also analyzed for the SE algorithm. The results show that only electrons with

energy below 20 keV could show some improvement with the lowering of cutoff value.

Discrepancies in the DPK curves found here can be better understood by analyzing the corresponding electron fluence for each case. Figures 3.3 (a) to 3.3 (e) present the electron fluence curves obtained for the monoenergetic electron point sources with the different codes and methods used.

The fluence curves obtained with MCNP6 (CHed and CHee+) and PENELOPE agreed well with RV along the entire radius of the spherical phantom. In general, the fluence curves obtained with EGSnrc, MCNP6 and PENELOPE showed faster drops than those obtained with TOPAS. Indeed, TOPAS fluence results demonstrated good agreement with other MC codes along the radius of the sphere, up to a certain point of the CSDA range (such as 0.8-1.0 R_{CSDA}) for all source energies. An increase in deviation is observed with an increase in the electron energy. For 3 MeV electrons, the fluence curve starts diverging at 0.8 R_{CSDA} . It should be noted that for TOPAS the energy cutoff of 50 eV was used and 3.0 MeV is the only monoenergetic electron case where TOPAS showed a difference higher than $\pm 5\%$ from the RV in the 0.9 R_{CSDA} range. TOPAS is a wrapper of Geant4 and it also includes Geant4-DNA facilities as well. So, one possible reason for this deviation can be that TOPAS performed detailed calculations using track structure facilities of Geant4-DNA. Whereas, other MC codes, MCNP6, EGSnrc and PENELOPE are condensed history based code and showed sharp drop in the fluence curves. Also, TOPAS can use a great number of physics constructors options, provided by GEANT4 toolkit, to gather the list of physics processes, particles and physics models desired for the simulation [38]. Thus, fluence output can be tuned, especially for 3.0 MeV electrons, using different physics constructors.

The results calculated by MCNP6 using SE mode showed increasing discrepant values for 0.5 MeV, 1.0 MeV and 3.0 MeV energies. The fluence curves start diverging at 0.8, 0.6 and 0.1 of the CSDA range, for 0.5 MeV, 1 MeV and 3 MeV electrons respectively. The faster drop in the MCNP6 SE fluence results may be responsible for the DPK curve shift to the left, confirming the overestimation of electron backscattering which is evidenced in SE mode.

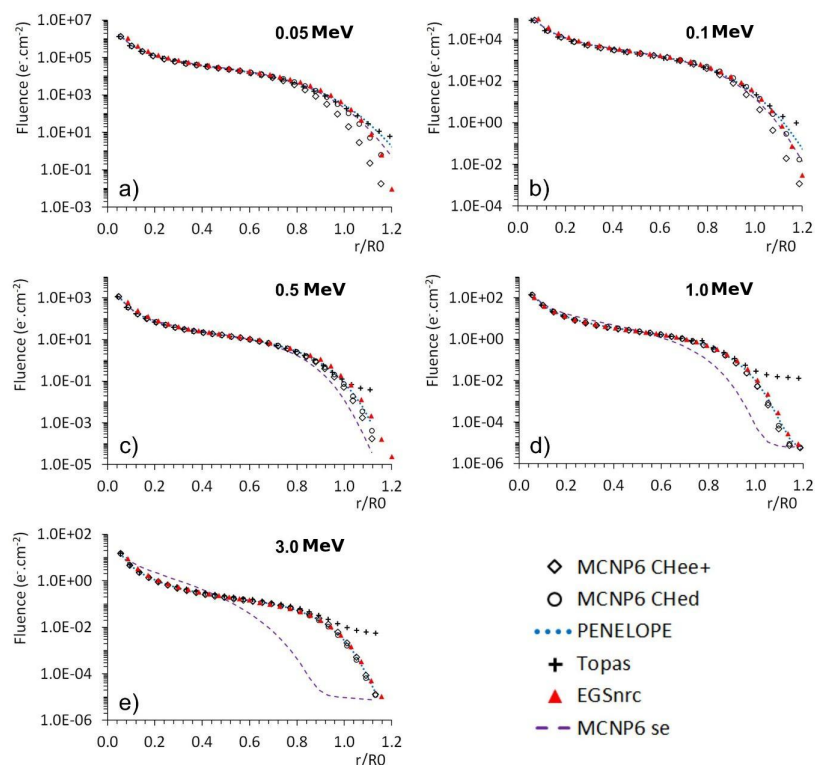


Figure 3.3 Fluence curves for monoenergetic electron point sources of: a) 0.05 MeV; b) 0.1 MeV; c) 0.5 MeV; d) 1 MeV; and e) 3 MeV

The DPK curves obtained for Lu-177, I-131, Sm-153, Sr-89, Ho-166 and Y-90 are presented in Figure 3.4. Lu-177, I-131 and Sm-153 are the radionuclides with lowest average energies (0.133 MeV, 0.182 MeV and 0.228 MeV, respectively). Good agreement between all MC codes was observed for the obtained DPK curves, including MCNP6 CH and SE routines. No MC code showed differences greater than 5% in comparison to the reference values obtained for EGSnrc. Results obtained from TOPAS, PENELOPE and MCNP6 routines CHdd and CHee+ were within $\pm 3\%$ deviation, in the r_{E90} range, compared to the EGSnrc curves. Chdd routine showed the best MCNP6 correlation with RV (differences $< \pm 2\%$).

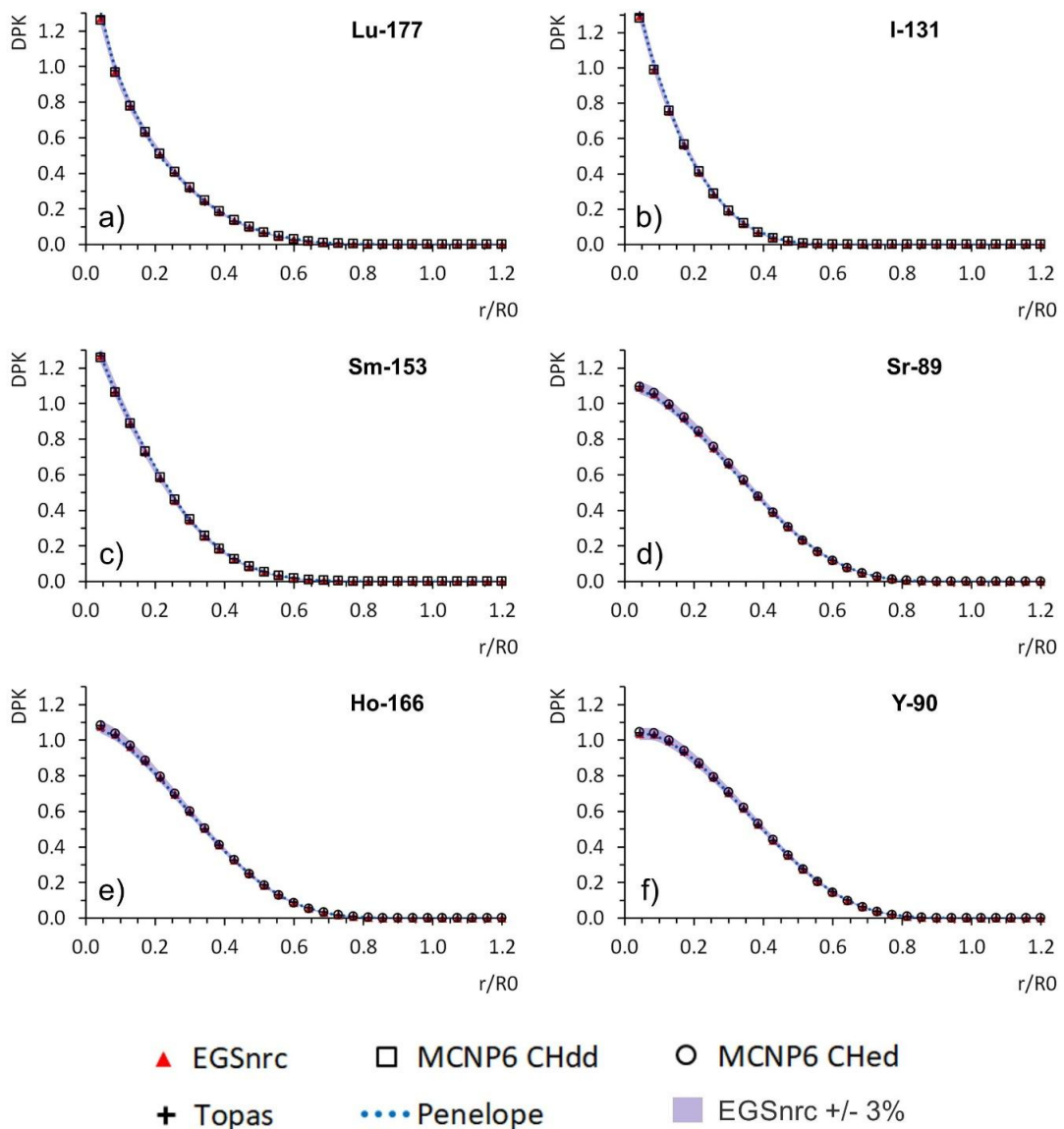


Figure 3.4 DPK curves obtained with different codes for 6 radionuclides: a) Lu-177, b) I-131, c) Sm-153, d) Sr-89, e) Ho-166 and f) Y-90.

Sr-89, Ho-166 and Y-90 are the radionuclides with highest mean energy (0.584 MeV, 0.668 MeV and 0.935 MeV, respectively). All codes, except MCNP6 CHed+ and SE routine, presented discrepancies lower than 5% with respect to EGSnrc reference values. The DPK curves computed using MCNP6 CHdd, CHed, CHed, TOPAS and Penelope were within $\pm 3\%$ of the EGSnrc curves, for these three radionuclides in the r_{E90} range. The best correlation with RV (differences $< \pm 1\%$) for MCNP6 was observed with CHed routine. Huge discrepancies (even higher than 70%) were observed for the results obtained with MCNP6 SE algorithm and it should not be used with higher energy radionuclides.

The increase in ESTEP value (CHee and CHee+) did not calculate the DPK values closer to RV for any radionuclide spectra simulations. The only improvement in DPK calculations observed was for 0.5 keV monoenergetic electrons using CHee and CHee+. The MCNP Manual does not make it clear that an excessive increase in ESTEP, as in CHee+ simulations, should be avoided. Using it, for the best case (0.5 keV electrons) CHee and CHee+ showed similar differences from RV. Such fact, associated with the high computational time and the possibility of generating instabilities in the CH algorithm seems to discourage this practice of excessively increasing ESTEP value.

DPK results for beta emitter radionuclides showed lower variations among codes than DPK results obtained for the monoenergetic electrons. Wu and coworkers found similar results using MCNP5 and FLUKA [135]. Each calculated point in the DPK curve represents the ratio of dose in a sphere shell relative to the dose in the entire sphere of radius R_{CSDA} . For monoenergetic sources all curves showed the same pattern. The most of the energy is deposited within the spherical region corresponding to approximately 60% of its radius (CSDA range) and doses in the shells beyond this point decrease rapidly. However, in realistic cases, i.e., when radionuclides with their energy emission spectra are simulated, DPK results present smoother curves along the R_{CSDA} radius, without the well-defined peak of energy deposition. MC codes present small differences in these cases and consistent DPK results were observed. Thus, studies related target radionuclide therapy and beta-emitting seeds brachytherapy using different MC codes and radionuclides studied here should present comparable results. It is very important due to the difficulty in obtaining experimental results.

As far as we know, no study has presented TOPAS DPK values for monoenergetic electrons and beta spectra, comparing the results with other codes. TOPAS present results in good agreement with EGSnrc and the other codes evaluated, proven to be reliable for this type of simulations. It should be remembered that, in this study, the default configuration for electron transport was used in simulations with the TOPAS code. Over the past five years GEANT-DNA electron transport was greatly improved [42, 136] and these developments, in terms of physics constructors, can be applied for tuning TOPAS simulations. In this way, future assessments can be made to investigate if some of these new options, in terms of physics constructors, can further improve the performance of this code, especially for 0.05 MeV and 3.0 MeV.

3.4 Conclusion

Experimental validations for electron energy deposition are very difficult, especially for the region near to the source, small volumes and low energy electrons. Benchmarking, such as the DPK comparison, remains a good option to evaluate the electron energy transport of different Monte Carlo codes.

In this study, the results obtained in the simulations using monoenergetic electron sources ranging from 0.05 up to 3.0 MeV, demonstrated that EGSnrc and PENELOPE MC codes had good agreement in the 0.9 R_{CSDA} range. The 0.05 MeV to 3.0 MeV energy range cover the majority of radionuclides energy spectra in nuclear medicine. TOPAS also presented results compatible with EGSnrc and PENELOPE, especially for electrons with energies of 0.05 MeV to 1.0 MeV. For 3.0 MeV, only the last shell in 0.9 R_{CSDA} range presented the differences higher than 10%; this can be attributed to the track structure nature of the electron transport used in TOPAS simulations. This fact is of lesser concern, since more than 90% of electron energy was already deposited before this shell and beta emissions in 3.0 MeV range are considerably rare.

The MCNP6 code showed results compatible with the other codes for 0.05 MeV, using the SE transport algorithm. The same was observed for energy sources of 0.5 MeV, 1.0 MeV and 3.0 MeV when using condensed-history routines (CHee to 0.5 MeV and CHed for both 1.0 and 3.0 MeV). The choice of the electron transport algorithm was found important to obtain the best correlation with EGSnrc DPK values when simulating monoenergetic electrons. DPK values for 0.1 MeV monoenergetic electrons, calculated using MCNP6, found deviating higher than $\pm 5\%$ from RV despite the attempts made to tune electron transport algorithms and physic parameters. Thus, further approaches regarding tuning of MCNP6 electron transport parameters for 0.1 MeV monoenergetic electrons would be desirable in the future.

All MC codes studied in this work could provide DPK values with differences less than $\pm 3\%$ in the r_{E90} range, for all simulated beta-emitting radionuclides (Lu-177, I-131, Sm-153, Sr-89, Ho-166 and Y-90). DPK results obtained with MCNP6 CH routines show better correlation with other codes for low energy beta-emitters (CHdd) as well as to high energy beta-emitters (CHed).

3.5 Acknowledgement

We would like to thank Dr. Ernesto Mainegra-Hing from National Research Council, Canada for helpful discussions on fluence calculations using EGSnrc. The following Brazilian institutions supported this research project: Fundação de Amparo à Pesquisa de Minas Gerais (FAPEMIG), Fundação de Amparo à Pesquisa do Estado de São Paulo (FAPESP) and Conselho Nacional de Desenvolvimento Científico e Tecnológico (CNPq).

3.6 Addendum

In this chapter following statements were made regarding TOPAS MC parameter setting and results:

- **Section 3.2.2 TOPAS:** default modular physics list and the energy cut off for electrons and photons was set to 50 eV.
- **Section 3.3:** So, one possible reason for this deviation can be that TOPAS performed detailed calculations using track structure facilities of Geant4-DNA.
- **Conclusion:** TOPAS also presented results compatible with EGSnrc and PENELOPE, especially for electrons with energies of 0.05 MeV to 1.0 MeV. For 3.0 MeV, only the last shell in 0.9 RCSDA range presented the differences higher than 10%; this can be attributed to the track structure nature of the electron transport used in TOPAS simulations.

The above statements may not be correct because it is not known if the track structure facility of TOPAS was turned ON explicitly or not. In TOPAS user must explicitly select Geant4-DNA physics list option to perform detailed simulation of electron transport. Considering that this work was performed in collaboration with several group from various institutions, it is not known if the the Geant4-DNA physics list was explicitly used or not. If not then the results presented in Fig. 3.3, electron fluence, for TOPAS may not be correct. Additionally, the differences observed in fluence curves may be the artifact of using wrong physics list settings.

Chapter 4

Microdosimetric calculations for radionuclides emitting β and α particles and Auger electrons

Baljeet Seniwal^{1,*}, Mario A. Bernal², Telma C.F. Fonseca¹

¹ DEN & Pós-Graduação em Ciências e Técnicas Nucleares-Universidade Federal de Minas Gerais Departamento de Engenharia Nuclear, 31270-901, Belo Horizonte, Brasil

² Departamento de Física Aplicada, Instituto de Física Gleb Wataghin, Universidade Estadual de Campinas, SP, Brazil.

Corresponding author: Baljeet Seniwal (bseniwal@eng-nucl.dout.ufmg.br)

Journal name: Applied Radiation and Isotopes journal and presented in the ISSSD 2019.

Citation: Seniwal, B., Bernal, M. A., & Fonseca, T. C. (2020). Microdosimetric calculations for radionuclides emitting β and α particles and Auger electrons. Applied Radiation and Isotopes, 166, 109302.

Abstract

This work focuses on the calculation of S-values and radial energy profiles for radionuclides emitting high (Y-90, Sr-89), medium (Re-186, Sm-153) and low-energy (Er-169, Lu-177) β -particles, Auger electrons (In-111, Ga-67, I-123) and α -particles (At-211, Ac-225). Simulations were performed using the EGSnrc and GEANT4-DNA Monte Carlo (MC) codes for a spherical cell geometry. S-values were computed using decay spectra available in literature for Tc-99m and In-111. To investigate the effect on S-value when the same emission spectrum is used in two different MC codes. Internal modules of the MC codes were used to simulate the decay of other radionuclides mentioned above. Radial energy profiles for uniformly distributed radioactive sources in the cell nucleus and cytoplasm were calculated and results were compared with the literature. For S-values calculated using the same emission spectrum, the results showed good agreement with each other and with the literature. Whereas, the S-values calculated using the internal decay data of the MC codes, for instance, for Ga-67 and Y-90, showed discrepancies up to 40%. Radial energy profiles were also different from those reported in the literature. Our results show that well validated radiation emission spectra must be used for such calculations and internal decay spectra of MC codes should be used with caution. The normalized probability density functions must be used to sample points uniformly into spherical volumes and the methodology proposed here can be used to correctly determine radial energy profiles.

Keywords: Radio-immunotherapy, S-value, Radial Energy Profile, GEANT4-DNA, EGSnrc, β -emitter, α -emitter, Auger-emitter.

4.1 Introduction

Radioimmunotherapy (RIT) is an internal radiation therapy that makes use of unsealed radiation sources conjugated with monoclonal antibodies. These antibodies are directed to specific tumor antigens to deliver radiation dose directly to tumor cells [137]. The characteristics of an ideal radiopharmaceutical for RIT are: (a) Specificity: the antibody should only attach to the tumor cells; (b) Universality: the antibody must link to all cells of tumor notwithstanding their location; (c) Cytotoxic potency: the radiopharmaceutical must kill the tumor cells with high efficiency; (d) Short-range effects: the normal tissues should not be damaged or effected by the radiopharmaceutical, while in circulation or attached to tumor antigens [138]. The first

two characteristics, specificity and universality, are affected by the choice of the monoclonal antibody and its binding efficiency with the radioisotope in question. Cytotoxic potency and short-range effects are dependent on the choice of radionuclide. Three possible solutions are: α -particle, β , or Auger electron (AE) emitting radionuclides, α -particle emitting radionuclides offer high Linear Energy Transfer (LET) and short-range effects. For instance, At-211 has a LET value of 97 keV/ μm and a mean range of 70 μm in tissue. Hence, there is a high probability of killing tumor cells and reducing normal tissue complication [139]. However, β -emitting radionuclides offer low LET and usually travel long distances within the tissue. For instance, Y-90, a β -emitting radionuclide, offers a LET of 0.2 keV/ μm and has a mean range of 3960 μm . Auger electron (AE) emitting radionuclides, similar to α -emitters, provide the advantages of short-range and high cytotoxicity [140]. Auger electrons (AE) have energy generally <500 eV and travel several nanometers in biological tissue. The abundant emission of short-range electrons results in large energy densities locally [141, 142]. From above, it may appear that both low LET and large range in tissue make β -particle emitting radionuclides poor candidates for RIT in comparison to Auger electron (AE) or α -emitting radionuclides. However, many experimental studies have reported that the distribution of radiopharmaceutical is not uniform within the tumor cells [143–145]. Hence, in case of non-uniform activity distribution within the cell for bulky tumors, β -emitting radionuclides can be used to achieve uniformity in the delivered radiation dose and minimum normal tissue complications. In general, bulky tumors are treated with radionuclides that emit high energy α -particles or β -particles. Whereas for treatment of small tumor clusters, Auger electron (AE) emitting radionuclides are used. The radio-pharmaceuticals used in clinical treatments are: I-131 for the treatment of thyroid cancer, P-32-orthophosphate used for the treatment of polycythaemia and thrombocythaemia and I-125-labelled MIBG (meta-iodobenzylguanidine) for the treatment of pheochromocytoma and neuroblastoma [146].

The Medical Internal Radiation Dose (MIRD) committee has proposed a general methodology to calculate the absorbed dose from the activity administered. One of the key parameter of this formalism is the S-value, $S(r_t \leftarrow r_s)$. It is defined as the absorbed dose to the target region (r_t) per unit of activity present within the source region (r_s). For single cell dosimetry, the source and target region combinations are: C \leftarrow C, C \leftarrow CS, N \leftarrow Cy, N \leftarrow N, and N \leftarrow CS, where C: Whole Cell, N: Nucleus, Cy: Cytoplasm and CS: Cell Surface. Falzone et al., [57] calculated the S-value and dose point kernel (DPK) which is a radial dose distribution around an isotropic point source, for 12 Auger emitting radionuclides. Different concentric and eccentric cell/nucleus arrangements were modelled using the PENELOPE MC code [78]. It has been reported that the computed S-values were in agreement with MIRD [147] when

the source and target regions were overlapping each other, for instance $S(N \leftarrow N)$. Whereas, large variations were reported for other combined regions, $S(N \leftarrow Cy)$ and $S(N \leftarrow CS)$. Strong effects of eccentricity were found when the nucleus size is considered smaller than the size of the cell and considering the radiation source sampled on the cell surface. It was concluded that for evaluating the efficacy of any radioisotope for theranostic applications, the single-cell dosimetry approach must be considered. Theranostics can be defined as a rationale of combining therapeutic and medical imaging capabilities into a single agent in order to obtain high therapeutic efficacy and desirable bio-distribution [148]. Falzone et al., [58] also investigated the effect of the decay data on S-value and DPK results obtained for 14 Auger emitting radioisotopes by simulating, with PENELOPE MC code, the decay data published by MIRD [149] and BrIccEmis code [150]. The authors found that the MIRD decay data overestimate the yield of Auger (AE) electrons, Coster Kronig (CK) electrons and photons in comparison to BrIccEmis and the DPK obtained using BrIccEmis were found to be considerably different from those obtained using the MIRD database. It was concluded that while using MIRD decay data for simulations, this overestimation must be taken into account. Champion et al., [52] reported an inter-comparison to check the accuracy of the low energy models implemented into the GEANT4-DNA toolkit [41, 44], against other well documented MC codes (EGSnrc [50], PENELOPE etc.). It was reported that the GEANT4-DNA code was able to accurately model radial energy profiles for mono-energetic electron sources.

Sefl et al., [55] calculated S-values for ellipsoidal, spherical and irregular cell geometries using the GEANT4-DNA toolkit. Mono-energetic electron sources with energy ranging from 1 to 100 keV and Auger electron emitting radioisotopes: Tc-99m, I-125 and In-111 were considered in the calculations. The decay spectra published by the AAPM [151] were used to calculate the S-values when the radiation source was uniformly sampled in different compartments of the cell. They also presented an algorithm to sample points randomly within sub-cellular volume. Authors reported: (a) difference up to 20% in the S-value calculated using GEANT4-DNA and MIRD database for mono-energetic electrons; (b) and less than 10% for Auger electron emitting radionuclides; (c) On average, the difference between S-values from MIRD and GEANT4-DNA, for spherical cell geometry, up to 20% was found; (d) the S-values calculated for ellipsoidal cell geometry and irregular cell geometry were compared with S-values of spherical cell geometry and reported: (i) maximum difference of 32% for ellipsoidal geometry and (ii) 100% to 300% discrepancies for irregular cell geometry; (e) the S-values calculated for spherical cell geometry using two I-125 decay spectra published by AAPM were found deviating up to 19% from each other. The authors concluded that the spherical cell geometry can be safely used as an approximation comparing to the ellipsoidal

one.

Fourie et al., [56] calculated S-values and radial energy profiles considering radiation sources uniformly distributed in the nucleus, cytoplasm and the whole cell. The internal database of GEANT4 was used to simulate the decay of the I-123 radionuclide. All discrepancies observed in S-value with respect to literature were attributed to differences in the emission spectra used by different authors.

Andre et al., [152] calculated S-values for a number of mono-energetic electron sources and I-131, I-132, I-133, I-134 and I-135 radioisotopes for spheres of nanometric sizes and two spherical geometries describing the thyroid components. The aim of their investigation was to evaluate the accuracy of the GEANT4-DNA physics models in simulating the transport of low energy electrons in liquid water. GEANT4-DNA results were compared against numerous MC codes and literature. All MC codes were found statistically compatible with GEANT4-DNA and the observed dispersion were attributed to differences in stopping power.

Considering all above studies and the importance of single cell dosimetry, in this article the S-value and radial energy profiles for spherical cell geometry were studied using EGSnrc and GEANT4-DNA MC codes for α -, β -particle and Auger electron (AE) emitting radionuclides. Wide variety of radionuclides were selected in order to study the efficacy of these radionuclides for RIT applications. The results are presented in following sequence: (a) S-values obtained for Tc-99m and In-111 were calculated using the emission spectra reported by AAPM [151] and compared to results reported by [55]. The motivation was to check the deviation on the S-value using different MC codes; (b) The S-values for α -particle (At-211, Ac-225), high (Y-90, Sr-89), medium (Re-186, Sm-153) and low (Er-169, Ga-67) energy β -particle and Auger electron (In-111, Ga-67) emitting radionuclides are reported. For calculation of S-value the decay spectra of radionuclides were extracted from radioactive decay module of GEANT4 and *egs_radionuclide_source* library of EGSnrc. In order to test the reliability of the internal modules of both MC codes to simulate the decay of radionuclides; (c) The radial energy profiles is the energy deposited per decay along the radius of the source region (nucleus/cytoplasm) and it was obtained for I-123 to compare against the one reported by [56]; (d) New radial energy profiles were obtained and the total energy deposited per decay, normalized to the square of the radial distance versus the radius of the source region, are reported for AE and β -particle emitters.

4.2 Material and Methods

All modelling and simulations were performed on Ubuntu v.16.04 operating system on desktop with an AMD Ryzen 3 1200 Quad-Core processor with 8GB of memory. The statistical uncertainties, calculated in terms of standard deviation of the mean, were less than 1%. The computing time of each simulations varied; for instance, GEANT4-DNA took 3-4 hours to finish each simulation for β and Auger emitter using 10^5 histories. For α emitting radioisotopes using 5×10^4 particles, it took almost 1.5-3 days to finish each simulation. EGSnrc code took between 5 to 10 minutes for each simulation.

4.2.1 GEANT4-DNA

The GEANT4-DNA code is a internal package of GEANT4, a general purpose Monte Carlo simulation toolkit. It is capable of simulating track structures of electrons and various ions, such as He^{2+} , H^+ , C^{6+} , N^{7+} , in liquid water. It is able to simulate physical processes such as ionization, excitation, elastic scattering, vibrational excitation and dissociative attachment. The simulation of electron interactions is possible for energies from 1 MeV down to 7.4 eV and interactions of helium ions, from 400 MeV down to 1 keV [41]. The G4EmDNAPhysics() [41] and G4RadioactiveDecay() physics functions were used to accurately simulate the transport of low energy electrons and α -particles and the decay of radionuclides. Energy cut off was set to 7.4 eV and bosons, leptons, baryons and ions were constructed. The simulation of processes such as the Auger cascade and fluorescence emission were enabled.

4.2.2 EGSnrc

EGSnrc [50] is a general purpose MC code based on the condensed history approach. It is restricted to simulations of the coupled electron-photon transport, with energies ranging from 10 GeV down to a few keV. It uses electron-impact ionization of inner shells and Möller and Bhabha inelastic cross-sections for outer shells to simulate the interaction of electrons and positrons with matter. It cannot handle the transport of α -particles. EGSnrc is extensively used for MC simulations in the Medical Physics field [133, 47, 46]. In this study, the C++ based module of the EGSnrc software was utilized. The *egs_sphere* library was used for geometry simulation and the *egs_radionuclide_source* library was employed to simulate the decay of radionuclide from internal database. In order to implement the spectra for

Tc-99m and In-111 [151], *egs_isotropic_source* source library was used. A region selection method was utilized to bound and sample the source uniformly and randomly in different compartments of the cell. EGSnrc parameters AE = ECUT = AP = PCUT were set to 0.001 MeV. For the simulation of radial energy profiles, the cellular volume was divided into 200 spherical shells with radial thickness of $2.5 \times 10^{-2} \mu\text{m}$.

4.2.3 The MIRD formalism for S-value estimation

Medical Internal Radiation Dose (MIRD) committee has proposed a methodology to perform internal dosimetry for radiation therapy using radionuclides [153, 82, 154]. The aim of the MIRD committee is to develop models and methods based on mathematical calculations to estimate the radiation dose deposited in different parts of human body due to administered radio-pharmaceuticals. Using the MIRD methodology, the absorbed dose within a specific organ can be estimated as follows:

$$\bar{D}(r_t \leftarrow r_s) = \tilde{A}_{r_s} \cdot S(r_t \leftarrow r_s) \quad (4.1)$$

where r_t represents the target region, r_s is the source region, $\bar{D}(r_t \leftarrow r_s)$ represents the mean absorbed dose within the target region, \tilde{A}_{r_s} is the cumulative activity inside the source region and $S(r_t \leftarrow r_s)$ is the absorbed dose per activity within the target region; also known as S-value. S-value can be expressed as:

$$S(r_t \leftarrow r_s) = \frac{EY \cdot \phi}{m_{r_t}} \quad (4.2)$$

where Y is the emission probability of radiation with energy E , EY is the mean emitted energy per decay of the radionuclide, ϕ is the absorbed fraction of energy emitted from r_s that is absorbed in r_t and m_{r_t} is the mass of the target region. The current study is based on the estimation of S-values and $(EY \cdot \phi)$ using MC simulation.

4.2.4 Cell geometry and Random point sampling

S-value can be calculated using MC simulations. According to the definition of S-value, it is assumed that the radioactivity is uniformly distributed inside the source region. Therefore, the points emitting radiation must be sampled randomly and uniformly inside different cellular compartments (whole cell, nucleus, cytoplasm, cellular surface). The spherical cell geometry was composed of two concentric spheres made up of unit-density water. The cell and nucleus radii were kept at $5\mu m$ and $4\mu m$, respectively (as shown in Fig. 4.1). The values of these radii lead to similar cell and nucleus volume as those defined by the MIRD committee [147].

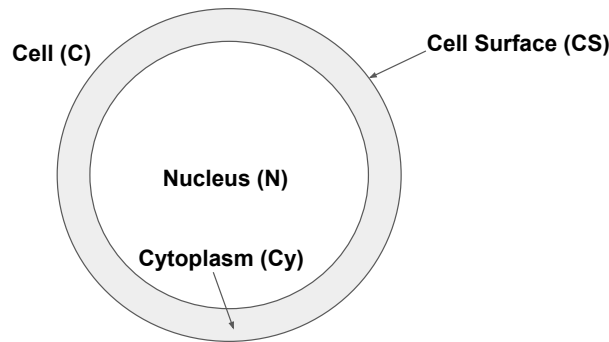


Figure 4.1 Cell geometry used for S-value and radial energy profile calculations, where the cell and nucleus radii are $5.0\mu m$ and $4.0\mu m$, respectively.

To sample the points in different cell compartments, a normalized probability density function (PDF) was built by considering a infinitesimal volume element in the spherical coordinate system and two parameters were introduced R_{min} : inner radius of the shell and R_{max} : outer radius of the shell. Thus, the derived equations are:

$$\cos \theta = 1 - 2\xi_1 \quad (4.3)$$

$$\phi = 2\pi\xi_2 \quad (4.4)$$

$$r = \sqrt[3]{(R_{min})^3 + ((R_{max})^3 - (R_{min})^3)\xi_3} \quad (4.5)$$

where r , θ and ϕ are the coordinates of the point in the spherical coordinate system and ξ_1 , ξ_2 and ξ_3 are random numbers.

4.2.5 Calculation of S-value and Radial Energy Profile

S-values were determined for low energy β -emitters: Er-169, Lu-177; medium energy β -emitters: Re-186, Sm-153; high energy β -emitters: Y-90, Sr-89; α -particle emitters: At-211, Ac-225; Auger emitters: In-111, Ga-67 and Tc-99m radionuclides. Equation (4.2) was used in these calculations. Radial energy profiles were computed by plotting energy deposited per decay at a point ($EY \cdot \phi/r^2$) versus r , where r is radial dimension with respect to the center of the cell.

4.3 Results and Discussion

Table 4.1 reports cellular S-values for Tc-99m and In-111 calculated for different source-target combinations, using the decay spectra published by Howell et al.(1992) [151]. The results obtained using the GEANT4-DNA and EGSnrc codes are presented and compared to those reported in Sefl et al. (2015) [55]. The different source-target region combinations considered were C \leftarrow C, N \leftarrow N, N \leftarrow Cy, N \leftarrow CS and C \leftarrow CS. It should be remembered that the uncertainties of our results are below 1%, which should be taken into account for the analysis of the discrepancies reported in this section. That is, discrepancies above about 1% may be regarded as statistically significant.

For the S-values calculated using GEANT4-DNA, a maximum difference of 10% was observed for S(C \leftarrow CS) in the case of Tc-99m, while variation of 7% in case of In-111 for S(C \leftarrow CS). Small differences were observed for S(N \leftarrow Cy) and S(N \leftarrow N) for both radionuclides. On average, discrepancies in S(N \leftarrow CS), and S(C \leftarrow CS) were found higher than S(N \leftarrow N), S(N \leftarrow Cy) and S(C \leftarrow C) for both Tc-99m and In-111. All the differences observed for S-values were less than 10%. A good agreement between the literature and GEANT4-DNA calculated cellular S-values was observed. However, for the S-values calculated using EGSnrc, the maximum discrepancies were observed in the case of S(C \leftarrow CS): Tc-99m (22%) and In-111 (25%). The minimum difference of $\sim 0\%$ was observed in the calculation of S(N \leftarrow N) and S(C \leftarrow C) for Tc-99m. For In-111 S(N \leftarrow Cy), S(N \leftarrow N), and S(C \leftarrow C) were

found deviating by approximately 2% respect to [55]. All discrepancies were less than 10% except for S(C←CS). This variation can be attributed to the thickness of CS (7 nm was considered) and it is possible that algorithm used by EGSnrc is not able to sample points accurately in shell of such a small thickness or it can be attributed to different physics models and transport algorithm particularities found in these two codes. In overall both EGSnrc and GEANT4-DNA calculated S-values were found in good agreement with respect to the literature [55]. The readers must consider that the aim of this comparison was not to verify the accuracy of EGSnrc and GEANT4-DNA with respect to each other. In order to compare the accuracy of two MC codes the comparison must be performed using monoenergetic low energy electron sources as performed by Ref. [52]. As the use of full emission spectrum tends to smooth the results, which may hide the differences. The aim of this comparison was to instigate the effect on calculated S-value when same emission spectrum and simulation geometry are used but different MC codes are employed.

Table 4.1 Comparison of S-values calculated using GEANT4-DNA and EGSnrc for different source target combinations with respect to Sefl et al. 2015 using emission spectrum published by Howell et al. 1992 for Tc-99m and In-111.

		S(C←C) (Gy/Bq/s)	S(N←N) (Gy/Bq/s)	S(N←Cy) (Gy/Bq/s)	S(N←CS) (Gy/Bq/s)	S(C←CS) (Gy/Bq/s)
Tc-99m	GEANT4-DNA	8.11E-04(1.34%)	1.60E-03(-1.91%)	8.39E-05(-1.21%)	4.62E-05(7.41%)	3.83E-04(10.09%)
	EGSnrc	8.27E-04(-0.61%)	1.58E-03(-0.64%)	8.11E-05(2.17%)	4.92E-05(1.40%)	3.34E-04(21.60%)
	[55]	8.22E-04	1.57E-03	8.29E-05	4.99E-05	4.26E-04
In-111	GEANT4-DNA	1.48E-03(2.81%)	2.74E-03(1.31%)	3.53E-04(1.90%)	2.29E-04(5.95%)	7.74E-04(7.44%)
	EGSnrc	1.55E-03(-1.68%)	2.83E-03(-1.89%)	3.70E-04(-2.68%)	2.61E-04(-7.35%)	6.25E-04(25.25%)
	[55]	1.52E-03	2.78E-03	3.60E-04	2.43E-04	8.36E-04

*The values in brackets represent the percentage deviation between both studies.

Table 4.2 depicts the S-values calculated for 10 radionuclides considering C←C, N←N, N←Cy, N←CS and C←CS as source and target region combinations within the cellular volume. The decay of these radionuclides was simulated using *egs_radionuclide_source* library of EGSnrc and radioactive decay module of GEANT4. Since, EGSnrc does not support the transport of α -particles GEANT4-DNA was used to calculate cellular S-values for α emitting radionuclides. The S-values were calculated by simulating the whole radionuclide progeny. The order observed for the S-value deposition was α -emitters > Auger electron emitter > low energy β -emitter > medium energy β -emitter > high energy β -emitter. The S-values obtained for Ac-225 were more than twice of At-211 for different source target combinations.

The S-values calculated for α -emitters were compared against the MIRDcell database [155]. The calculated S-values for both At-211, with maximum difference of 6%, and Ac-225, with maximum difference of 9.5%, were found in good agreement with this database. For all other radionuclides the S-values calculated using EGSnrc and GEANT4-DNA were compared against the results published in the literature. In Refs. [114, 55], cellular S-values were calculated using the decay spectrum published by AAPM [151], whereas [156] used the decay spectrum provided by [157]. The largest discrepancies were observed for S-values calculated using GEANT4-DNA, while those calculated using EGSnrc were found in good agreement with the literature.

For EGSnrc the largest variations were observed for Auger electron emitting radionuclides (In-111 and Ga-67). These differences range from 6% to 10% for S(C \leftarrow C), S(N \leftarrow N), S(N \leftarrow Cy). Whereas, when radiation source was distributed on the cell surface 12% to 18% of variation was observed. However, for high energy β -particle emitting radionuclides (Y-90 and Sr-89), all discrepancies were less than 10%.

The S-values calculated using GEANT4-DNA for In-111 and Sr-89 were with a maximum variations observed up to 17% when radionuclide is distributed on the surface of the cell and differences up to 14% were observed when the radioactive source was distributed within the cellular compartments. However, GEANT4-DNA showed large variations for the cellular S-values calculated for Ga-67 and Y-90, which ranged from 20% to 50%. Maximum variations were observed for S(C \leftarrow CS), S(N \leftarrow CS) and S(N \leftarrow Cy). Fourie et al., [56] also reported a similar behaviour when comparing the GEANT4-DNA to literature. They reported discrepancies up to 23% for I-123 and only three source-target combinations were considered, C \leftarrow C, N \leftarrow N and N \leftarrow Cy. Apart from the differences with respect to literature GEANT4-DNA calculated S-values also showed large variations when compared to EGSnrc. Particularly, for Er-169, Sm-153 and Y-90, variations even larger than 100% were observed. All these variations can be attributed to differences in the decay spectra of radionuclides. It was also found that the decay spectra obtained from internal library of EGSnrc are more reliable than those from GEANT4. For Auger emitters, Ref. [58] has also reported the overestimation in the yield of AE, CK electrons, and photons by the MIRD decay data in comparison to the BrIccEmis code. Hence, it is recommended to use validated spectra for calculating S-values. Spectra published by [151, 150] may be a good choice.

Figure 4.2 reports the total energy deposited per decay along the radius of the cell when

I-123 was uniformly sampled within the nucleus (Red) and cytoplasm (Blue). This profile was obtained when radiation source was sampled using the probability distribution function described in section 2.2.4.

These energy profiles do not match with the one reported by [56]. Two possible reasons can be suggested for these differences: (1) The probability function used by Fourie et al. is different from the one used in this study or (2) they reported dose instead of energy deposited in each spherical shell. If the activity is uniformly distributed within a sphere, then the radial dose function should be constant, at least far enough from the sphere surface so that no frontier effect can be observed. Then, for a radial dose function constant, the energy deposited in each spherical shell must increase with the radius because the mass of the shell also increases.

Table 4.2 S-values calculated using *egs_radionuclide_source* library of EGSnrc Monte Carlo software and Radioactive decay module of GEANT4 toolkit for various source-target combinations of cellular compartments.

Radionuclide	Monte Carlo code	S(C←C) (Gy/Bq/s)	S(N←N) (Gy/Bq/s)	S(N←Cy) (Gy/Bq/s)	S(N←CS) (Gy/Bq/s)	S(C←CS) (Gy/Bq/s)
At-211 (α)	GEANT4-DNA	3.87E-02(3.06%)	6.06E-02(5.90%)	2.69E-02(3.59%)	2.03E-02(3.33%)	2.57E-02(3.38%)
	MIRDcell [155]	3.99E-02	6.44E-02	2.79E-02	2.10E-02	2.66E-02
Ac-225 (α)	GEANT4-DNA	1.04E-01 (-9.56%)	1.61E-01(-6.05%)	6.40E-02(4.39%)	4.84E-02(4.35%)	6.06E-02(4.72%)
	MIRDcell [155]	9.47E-02	1.52E-01	6.69E-02	5.06E-02	6.36E-02
In-111 (Auger)	GEANT4-DNA	1.39E-03(8.68%)	2.50E-03(10.07%)	3.04E-04(15.56%)	1.89E-04(22.22%)	6.62E-04(20.81%)
	EGSnrc	1.59E-03(-4.65%)	2.91E-03(-4.37%)	3.84E-04(-6.13%)	2.70E-04(-10.05%)	6.76E-04(-23.62%)
	[55]	1.52E-03	2.78E-03	3.60E-04	2.43E-04	8.36E-04
Ga-67 (Auger)	GEANT4-DNA	1.48E-03(22.92%)	2.87E-03(20.72%)	3.95E-04(23.60%)	7.30E-05(48.23%)	6.20E-04(33.97%)
	EGSnrc	2.04E-03(-6.31%)	3.82E-03(-5.66%)	5.70E-04(-10.17%)	1.58E-04(-12.15%)	8.04E-04(14.36%)
	[114]	1.92E-03	3.62E-03	5.17E-04	1.41E-04	9.39E-04
Er-169 (Low β)	GEANT4-DNA	8.96E-04	1.48E-03	5.60E-04	3.77E-04	4.69E-04
	EGSnrc	1.77E-03	3.12E-03	7.65E-04	4.14E-04	9.53E-04
Lu-177 (Low β)	GEANT4-DNA	7.90E-04	1.27E-03	4.87E-04	3.29E-04	4.13E-04
	EGSnrc	1.04E-03	1.74E-03	5.90E-04	2.47E-04	6.15E-04
Re-186 (Med. β)	GEANT4-DNA	5.50E-04	9.40E-04	2.88E-04	1.80E-04	2.85E-04
	EGSnrc	8.41E-04	1.46E-03	3.76E-04	2.39E-04	4.50E-04
Sm-153 (Med. β)	GEANT4-DNA	5.45E-04	8.71E-04	3.30E-04	2.38E-04	2.95E-04
	EGSnrc	2.63E-03	4.52E-03	1.16E-03	8.12E-04	1.34E-03
Y-90 (High β)	GEANT4-DNA	1.74E-04(29.27%)	2.70E-04 (30.05%)	1.08E-04 (37.21%)	7.87E-05 (38.52%)	9.67E-05 (40.67%)
	EGSnrc	2.25E-04(8.51%)	3.51E-04(9.19%)	1.60E-04(6.95%)	1.20E-04(5.96%)	1.49E-04 (8.39%)
	[156]	2.46E-04	3.86E-04	1.72E-04	1.28E-04	1.63E-04
Sr-89 (High β)	GEANT4-DNA	2.90E-04(-2.47%)	4.60E-04 (-3.37%)	1.83E-04(6.15%)	1.33E-04(8.28%)	1.63E-04(12.83%)
	EGSnrc	2.76E-04(2.36%)	4.32E-04(2.93%)	1.96E-04(-0.31%)	1.47E-04(-1.27%)	1.83E-04(2.34%)
	[156]	2.83E-04	4.45E-04	1.95E-04	1.45E-04	1.87E-04

*The values in brackets represent the percentage deviation between both studies.

Figure 4.3 (a) depicts the radial energy deposition profiles for Auger electron emitting radionuclides I-123, In-111 and Ga-67. In this case, values were normalized to the square of the radius. The reader should notice that the volume of the spherical shell increases with r^2 to a good approximation, so the profiles reported here could be considered as radial dose functions. I-123, In-111 show flat normalized energy profiles when radiation source is uniformly sampled within the nucleus or cytoplasm.

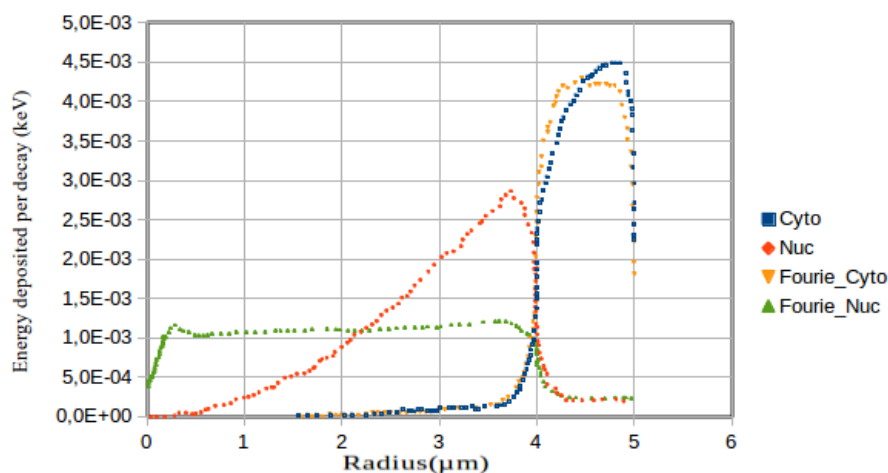


Figure 4.2 Energy deposited per decay (keV) along the radius of cell (μm), when I-123 radionuclide is sampled uniformly in nucleus (Red) and cytoplasm (Blue) compared with Fourie et al. 2015

Also, it can be observed that Ga-67 does not have a dose falloff outside the source region as sharp as the rest of the isotopes. When nucleus is used as a source region, some energy is also deposited in cytoplasm and vice-versa. These behaviors can be explained by the range of emitted electrons and the energy of emitted photons. Ga-67 deposited the largest amount of energy per decay, In-111 and I-123 deposited almost the same amount of energy.

Figures 4.3 (b), (c) and (d) report the radial energy deposited within the cell when low energy (Er-169, Lu-177), medium energy (Re-186, Sm-153) and high energy (Y-90 and Sr-89) β -emitters were uniformly sampled either within the nucleus or the cytoplasm. From these graphs: (i) consistent decrease in energy deposited to the source region (nucleus or cytoplasm) and (ii) consistent increase in energy deposited in the region adjacent to source region (cytoplasm or nucleus) was observed. This behaviour can also be related to the energy and range of emitted β -electrons. These profiles depicts the cross-fire effect of β -particle emitting radionuclides.

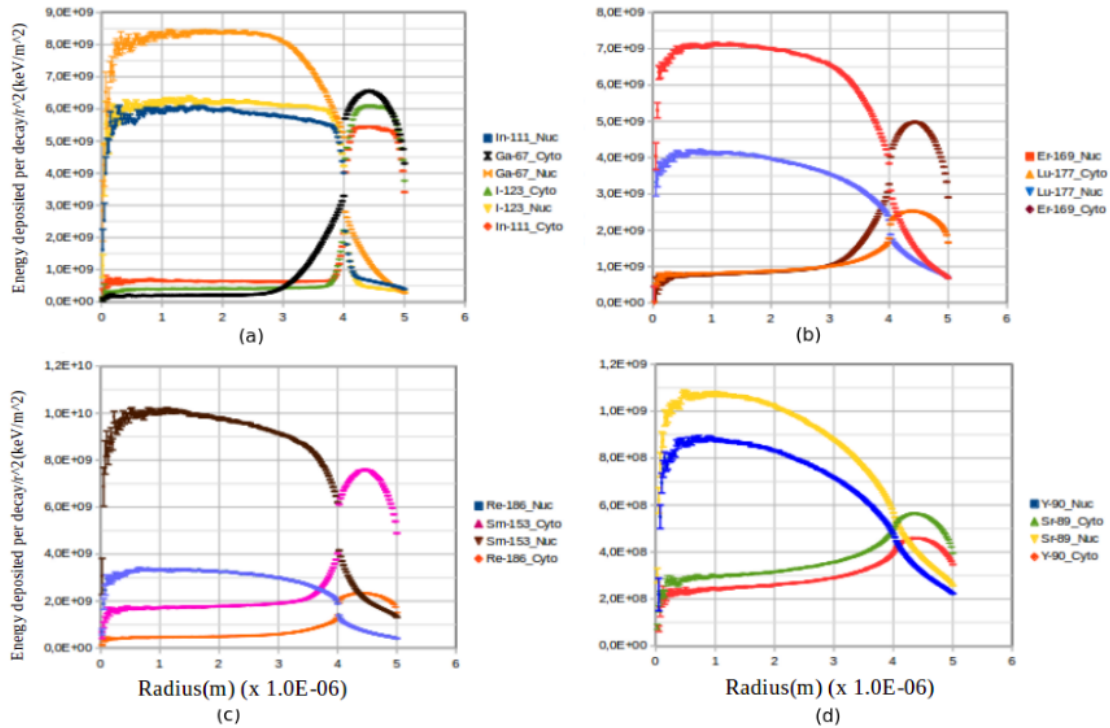


Figure 4.3 Energy deposited per decay along the radius of the cell, normalized to the square of radius, when (a) Auger emitting radioisotope (I-123, In-111 and Ga-67); (b) Low energy β -emitting radioisotope (Er-169 and Lu-177); (c) Medium energy β -emitting radioisotope (Re-186, Sm-153) and (d) High energy β -emitting radioisotope (Y-90, Sr-89) are sampled uniformly within the nucleus or cytoplasm.

4.4 Conclusion

This work presents the S-values and the radial energy profiles for several source-target combinations in a spherical cell geometry calculated using EGSnrc and GEANT4-DNA Monte-Carlo codes. In total, 12 radionuclides were investigated, which includes α -, β -particle and Auger electron emitters. For the S-values calculated using the spectra reported by AAPM both EGSnrc and GEANT4-DNA showed good agreement with literature. EGSnrc had discrepancy up to 25% while GEANT4-DNA had differences up to 10%. This variation can be associated to the differences in physics models and transport algorithm particularities found in these codes. Furthermore, GEANT4 can simulate the decay of α -emitters. Since, the S-values calculated using GEANT4-DNA were found in good agreement with MIRDcell database [155]. For the S-values calculated using the emission spectra from internal modules of MC codes most of the discrepancies can be attributed to the differences in the emission spectra. It was found that the decay spectra obtained from the internal library of EGSnrc

are more reliable than those from GEANT4. Hence, for calculating S-values or simulating biological effects at nanometric dimensions, well validated radiation emission spectra must be used. Also, the order of S-values, from higher to lower values, is α -emitter > Auger emitters > low energy β > medium energy β > High energy β emitters. Thus, α emitters appear to be promising candidates for targeted radionuclide therapy.

The radial energy profiles obtained for the uniformly distributed activity in the source region (nucleus/cytoplasm) were found deviating from the Ref. [56]. This variation can be due to the difference in probability density function used the Ref. or author's have reported dose instead of energy deposited. Hence, it was suggested that the normalized probability density function must be used to sample points uniformly into spherical volumes. The new radial energy profiles were normalized to the square of the radius. For Auger emitting radionuclides flat normalized energy profiles were observed. Whereas, the cross-fire effect for β -particle emitting radionuclides was observed. This behaviour can be attributed to the range of emitted electrons.

4.5 Acknowledgments

The following Brazilian institutions support this research project: Research Support Foundation of the State of Minas Gerais (FAPEMIG), Brazilian Council for Scientific and Technological Development (CNPq) and Coordination for the Capacitation of Graduated Personnel (CAPES). Prof. T. Fonseca is grateful for the financial support provided by CNPq (processo n° 450493/2019-9 and AVG. 450493/2019-9) and FAPEMIG (Projeto APQ-00083-18 Processo n° 2070.01.0002992/2018-30). M. A. Bernal also thanks the CNPq, for financing his research activities through the project 306298/2018-0. He also acknowledges the support received from the FAPESP foundation in Brazil, through the 2011/51594-2, 2015/21873-8 and 2018/15316-7 projects.

Chapter 5

***In silico* dosimetry of low-dose rate brachytherapy using radioactive nanoparticles**

Baljeet Seniwai^{1,*}, Lucas F. Freitas², Bruno M. Mendes³, A. B. Lugão², K. V. Katti⁴,
Telma C.F. Fonseca¹

¹Departamento de Engenharia Nuclear - Universidade Federal de Minas Gerais, Av. Antônio Carlos, 6627, Pampulha, 31270-901, Belo Horizonte, MG, Brazil

²Nuclear and Energy Research Institute-IPEN/CNEN/SP, São Paulo, Brazil

³Nuclear Technology Development Center-CDTN/, BH / MG, Brazil

⁴Department of Radiology, Physics, Institute of Green Nanotechnology, University of Missouri, One Hospital Drive, Columbia, MO 65212, USA

Corresponding author: Baljeet Seniwai (bseniwal@eng-nucl.dout.ufmg.br)

Journal name: Physics in Medicine and Biology

Citation: Seniwai, B., de Freitas, L. F., Mendes, B. M., Lugao, A. B., Katti, K. V., & Fonseca, T. C. F. (2020). *In silico* dosimetry of low-dose rate brachytherapy using radioactive nanoparticles. *Physics in Medicine & Biology*.

Abstract

Purpose: Nanoparticles (NPs) with radioactive atoms incorporated within the structure of the NP or bound to its surface, functionalized with biomolecules are reported as an alternative to low-dose-rate seed-based brachytherapy. In this study, authors report a mathematical dosimetric study on low-dose rate brachytherapy using radioactive NPs.

Method: Single-cell dosimetry was performed by calculating cellular S-values for spherical cell model using Au-198, Pd-103 and Sm-153 NPs. The cell survival and tumour volume vs time curves were calculated and compared to the experimental studies on radiotherapeutic efficiency of radioactive NPs published in the literature. Finally, the radiotherapeutic efficiency of Au-198, Pd-103 and Sm-153 NPs was tested for variable: administered radioactivity, tumour volume and tumour cell type.

Result: At the cellular level Sm-153 presented the highest S-value, followed by Pd-103 and Au-198. The calculated cell survival and tumour volume curves match very well with the published experimental results. It was found that Au-198 and Sm-153 can effectively treat highly aggressive, large tumour volumes with low radioactivity.

Conclusion: The accurate knowledge of uptake rate, washout rate of NPs, radiosensitivity and tumour repopulation rate is important for the calculation of cell survival curves. Self-absorption of emitted radiation and dose enhancement due to AuNPs must be considered in the calculations. Selection of radionuclide for radioactive NP must consider size of tumour, repopulation rate and radiosensitivity of tumour cells. Au-198 NPs functionalized with Mangiferin are a suitable choice for treating large, radioresistant and rapidly growing tumours.

Keywords: Radioactive nanoparticles, low-dose-rate brachytherapy, dosimetric calculation, single-cell dosimetry, radio-therapeutic efficiency, EGSnrc.

5.1 Introduction

Nanoparticles (NPs) are used in radiation therapy (RT) to enhance the radiation response or as a therapeutic or theranostic agent [158, 159]. In this regard, NPs made of high-Z material, especially gold nanoparticles (AuNPs), can attenuate the ionizing radiations and enhance radiation dose within the tumor. The technique of radiation dose enhancement using AuNPs is called radiosensitization [160, 161]. Recently the enhancement in radiation dose by AuNPs is observed in brachytherapy (BT) [162–165]. It is due to the interaction of

X-rays from the BT source with atoms of AuNP through the mechanism of photoabsorption. After photoabsorption the Au atoms deexcite to produce a number of emission products: photo-electrons, Auger electrons, or characteristic X-rays [158, 32].

For solid tumors such as prostate cancer, localized within the organ, seed based BT is a preferred treatment modality [166]. Radioactive seeds of I-125/Pd-103 are permanently implanted within the prostate gland and low doses of radiation are delivered to the tumor volume for several months [9]. Seed based BT can be conjugated with AuNPs to deliver higher doses of radiation to the tumor volume. But low-dose rate BT has some limitations such as: limited options for radiation dose modulation, artifacts in radiographic images caused by metallic seeds, etc.

Recently, radioactive NPs are investigated as an alternative to low-dose rate seed based BT [9, 159]. There are two main categories of radioactive NPs: (a) radioactive nanoparticles: the radioactive atoms are incorporated within the structure of NP, (b) radiolabeled NPs: radioactive atoms are bound to the surface of NPs [32]. Nowadays a wide range of radioactive or radiolabeled NPs are available: metallic, polymeric, lipidic, etc. (presented briefly in Figure 5.1). These NPs are either made radioactive via neutron activation technique [9, 113] or are radiolabeled with the help of biomolecules or chelators [159, 167] or by heat induced radiolabeling technique [168].

Several experimental studies have been performed to investigate the therapeutic efficiency of both radioactive and radiolabeled NPs. Authors [29], investigated the therapeutic efficacy of Gum arabic glycoprotein (GA) functionalized radioactive Au-198 NPs. The single dose of 70 Gy was administered with intratumor injection to mice bearing human prostate xenografts. Shukla et al. [169], used epigallocatechin-gallate (EGCg) conjugated Au-198 NPs and performed pharmacokinetic studies in PC-3 xenograft mice. Investigators [170], used nanoseed with core of Pd-103 coated with gold. Here also, the radiotherapeutic efficiency was tested on xenograft model of prostate cancer. Authors [31], used two different types of radioactive NPs: (a) radioactive core of Pd-103 coated with gold, and (b) radioactive core of Pd-103 coated with radioactive Au-198 to test the therapeutic efficacy on xenograft model of prostate cancer. The NPs were functionalized with polyethylene glycol (PEG). Al-Yasiri et al. [59] and Katti et al. [9], also investigated the therapeutic efficiency on xenograft model of prostate cancer using Au-198 NPs functionalized with mangiferin (MGF). Investigators [113], used radioactive carbon nanocapsules of Sm-153 functionalized with Cetuximab (antibody) and performed pharmacokinetic studies on melanoma lung metastatic tumor model in mice.

Authors [167], utilized AuNPs radiolabeled with I-131 and twin arginine translocation (TAT) peptide to target the nuclei of the cancer cells.

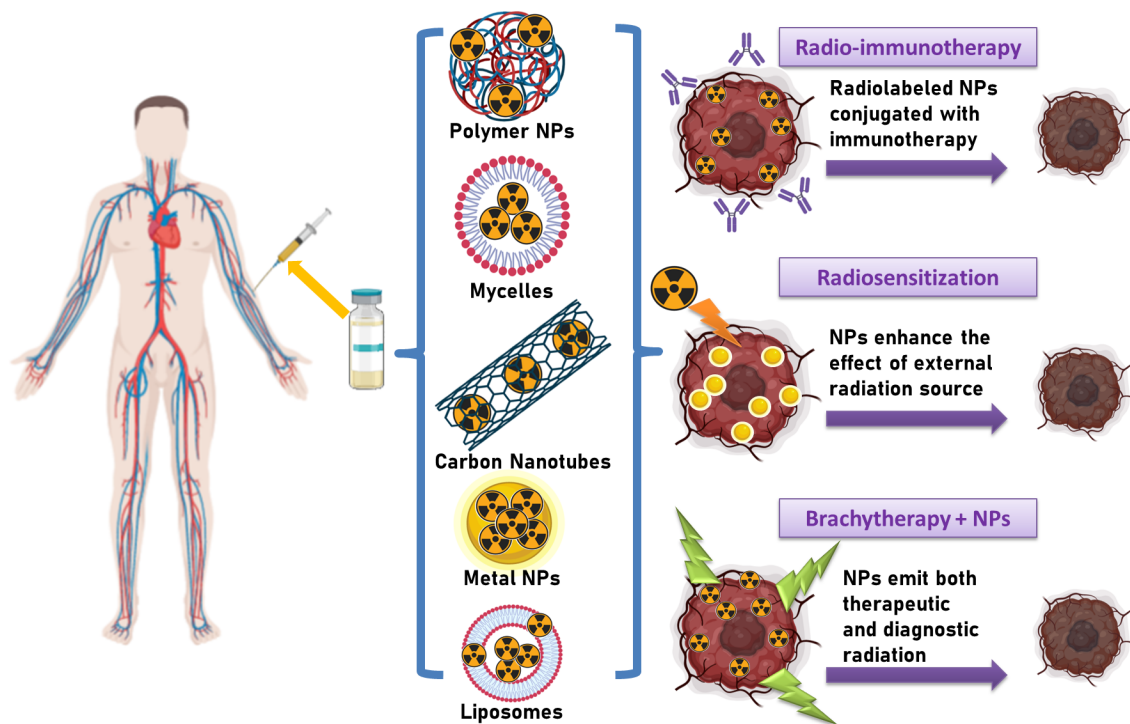


Figure 5.1 Main approaches for cancer treatment using nanomaterials and radiation. Nanomaterials, i.e. polymer nanoparticles, mycelles, carbon nanotubes, metal nanoparticles, and liposomes can be radiolabeled or made radioactive and act as therapeutic or diagnostic tools in radio-immunotherapy and in nanobrachytherapy, it can also enhance the effects of radiation via radiosensitization.

The linear quadratic (LQ) model is extensively used in radiation biology to analyze and predict the response of *in vitro* and *in vivo* experiments involving ionizing radiation [171]. The cell survival probability (S), according to LQ formalism, following radiation exposure is described as: $S = \exp(-[\alpha D + G\beta D^2])$. Where, α and β represent the radiosensitivity of the cell, D is the radiation dose to which cell is exposed and G represents generalized Lea-Catcheside time factor [172]. The G -factor narrates the effects of protraction in the dose delivery in terms of DNA double strand break (DSB) repair. It can hold values from 0 to 1. Where $G = 1$ represents a single fraction of radiation dose, leading to the most common expression of the LQ model: $S = \exp(-[\alpha D + \beta D^2])$. Whereas, $G < 1$ represents the increase in S due to the repair of DSBs during the protracted treatments, similar to

radiotherapy using radioactive NPs [173].

In case of radioactive NPs (radio-NPs) based radiotherapy (RT), the key radiobiological features are decreasing dose rate, repair of sub-lethal damage, proliferation of tumor cells and uptake and washout of radioactivity. Hence, an extended mathematical model is required to accurately estimate the probability of cell survival. Dale [174], extended the LQ model for exponentially decreasing dose rate by including the repair rate of sub-lethal damage. Authors assumed mono-exponential rate of repair independent of irradiation time, dose and dose rate. A detailed review on the radiobiology of targeted radiotherapy (TRT) was reported by Ref. [175]. Authors suggested that for low dose rate treatments, such as radio-NPs based RT, an approximately complete repair of sub-lethal damage can be assumed and the cell survival probability, in absence of proliferation, can be considered as an exponentially decreasing function of the dose: $S = \exp(-[\alpha D])$. It is because the repair rates of cells are generally much shorter than in comparison to the irradiation time. Wheldon et al. [176], estimated the curability of tumors of different sizes using a mathematical model. It was suggested that micro-metastases may be resistant to long range beta emitters and can be effectively treated using short range emitters. O'Donoghue [177], presented a simple mathematical model to investigate the effect of re-population of tumor cells, on S, irradiated using mono-exponentially decreasing dose rate. This model assumed instantaneous uptake of radiopharmaceutical by tumor cells. Ref. [178], used the LQ model to compare the conventional radiotherapy [179, 46] and targeted radiation therapy in terms of prescribed dose and relative biological effectiveness (RBE). Sefl et al. [180], extended mathematical model proposed by Ref. [177], by assuming the mono-exponential uptake and washout rate of radiopharmaceutical and investigated its effect on the cell survival. Present study makes use of the mathematical model proposed by Sefl. et al. [180] to estimate the cell survival and tumor volume curves.

In this study we performed dosimetric calculations to determine (a) Cellular S-values (single cell dosimetry) for spherical cell model using Au-198, Pd-103 and Sm-153 NPs compared with MIRDcell database [155]; (b) The cell survival and tumor volume curves compared with experimental studies; (c) The radio-therapeutic efficiency of Au-198, Pd-103 and Sm-153 NPs for (i) administered radioactivity, (ii) tumor volume and (iii) tumor cell type (variable radiosensitivity and repopulation rate), as shown in Table 5.1.

5.2 Methods

5.2.1 Cellular S-values

The cellular S-values were calculated for spherical cell geometry using EGSnrc [50] MC code following previously published methods [181] (and briefly described in Table 5.1) for 3 radionuclides: Pd-103, Sm-153 and Au-198. The selection of radionuclides was based on the availability of experimental data on the use of radioactive nanoparticles [31, 9, 113]. The cell geometry was constructed using two concentric spheres, representing commonly used cell geometry used for single cell dosimetry. The inner sphere with radius $4 \mu\text{m}$ was considered as nucleus and outer sphere with radius $5 \mu\text{m}$ as cell. The cell geometry was placed inside another sphere of radius 1.2 times radius of the cell. All spheres were composed of unit density water. Based on the definition of S-value, point, isotropic, radioactive sources were sampled uniformly and randomly within the source region. The Evaluated Nuclear Structure Data Files (ENSDF) for the radionuclides was extracted from the national nuclear data center database [182, 183]. These files contained the complete decay spectrum of the radionuclides (Pd-103, Sm-153 and Au-198). These ENSDF were used to simulate the decay of radioisotopes with the help of *egs_radionuclide_source* library of EGSnrc. The calculation was performed for 5 source target combinations: $(C \leftarrow C)$, $(C \leftarrow CS)$, $(N \leftarrow N)$, $(N \leftarrow CY)$ and $(N \leftarrow CS)$ (Table 5.1), where C = Cell, N = Nucleus, CY = Cytoplasm and CS = Cell Surface. All calculated S-values were compared with MIRDcell database [155] (presented in Table 5.2).

Table 5.1 Summary of calculations performed in this study.

	Cellular S-values	Calculations for surviving fraction or tumor volume	Comparison of radiotherapeutic efficiency of Pd-103, Sm-153 and Au-198 NPs
Parameters calculated	Cellular S-values for 5 different source target combinations: Cell to cell ($C \leftarrow C$), cell-surface to cell ($C \leftarrow CS$), nucleus to nucleus ($N \leftarrow N$), cytoplasm to nucleus ($N \leftarrow CY$) and cell-surface to nucleus ($N \leftarrow CS$).	1. Relative tumor volume, or 2. Tumor volume function of time based on results reported in the reference study	Relative tumor volume function of time by varying 1. Case 1: administered activities. 2. Case 2: tumor volume 3. Case 3: tumor cell type
Geometry Configurations	Spherical cell geometry Seniwal et al., 2020 1. Nucleus radius $4.0\mu m$ 2. Cell radius $5.0\mu m$	Spherical tumor volume 1. L-Pelletier et al., 2017: 0.27cc 2. Wang et al., 2020: 0.05cc 3. Katti et al., 2018: 0.03 cc	Spherical tumor of volume 1. Case 1: 0.3cc 2. Case 2: 0.3, 0.6 and 1.0 cc 3. Case 3: 0.3 cc
Radionuclides considered Reference data from previous publications	Pd-103, Sm-153, Au-198 Cellular S-values from [155]	Pd-103, Sm-153, Au-198 Experimental data 1. Pd-103 NPs: L-Pelletier et al., 2017 2. Sm-153 NPs: Wang et al., 2020 3. Au-198 NPS: Katti et al., 2018	Pd-103, Sm-153, Au-198
Tumor cell lines and radio-sensitivity parameter (α)		1. for Pd-103 NPs PC-3 cells: 0.059, 0.089, $0.107Gy^{-1}$ 2. for Sm-153 NPs B16F10 cells: 0.0068, 0.0102, $0.0122Gy^{-1}$ 3. for Au-198 NPs PC-3 cells: 0.059, 0.089, $0.107Gy^{-1}$	1. Case 1 and 2: PC-3 cells: $0.059Gy^{-1}$ 2. Case 3: PC-3 ($0.059Gy^{-1}$) and B16F10 ($0.0068Gy^{-1}$)
Activity administered		1. L-Pelletier et al., 2017: 62.9 MBq 2. Wang et al., 2020: 15.0 MBq 3. Katti et al., 2018: 0.15 MBq	1. Case 1: 20, 40, 60 MBq 2. Case 2 and 3: Activity was selected such that all radionuclides deposit equal absorbed dose, for Pd-103 is was fixed to 60 MBq and 600 MBq.
Outcome	Table 5.2	Table 5.3, Figure 5.2	Case 1: Figure 5.3 (A, B, C); Case 2: Figure 5.4 (A); and Case 3: Figure 5.4 (B)

5.2.2 Calculation of surviving fraction

For low dose rate radiation therapy techniques, such as targeted radiation therapy, the complete repair of sub-lethal damage can be expected. The cell survival curve, in the absence of proliferation, can be approximated by exponentially decreasing function of total dose D at time t ($SF(t) = \exp(-\alpha \cdot D(t))$), where $\alpha > 0[\text{Gy}^{-1}]$ [177]. Assuming that all tumor cells grow exponentially with a growth rate λ during the course of radiation treatment, and that NP uptake and washout occurs at mono-exponential rate [184, 180], the equation for cell survival curve can be written as follows:

$$SF(t) = \exp\left\{-\alpha D_0 \left(\frac{m-k}{m \cdot k} + \frac{1}{m} \exp(-m(t-t_i)) - \frac{1}{k} \exp(-k(t-t_i))\right) + \lambda(t-t_0)\right\} \quad (5.1)$$

where: (i) $D_0(> 0)$ = the extrapolated dose rate at $t = 0$, (ii) m = effective uptake rate, (iii) k = effective washout rate, (iv) t_0 = time of measuring tumor volume before intratumoral injection of radioactive NPs, (v) t_i = time of injection and (vi) α = radiosensitivity parameter. The uptake and washout rates (m and k respectively) can be estimated from the pharmacokinetic data of NPs by fitting using:

$$\%ID(t) = \%ID(\exp(-kt) - \exp(-mt)) \quad (5.2)$$

where $\%ID$ is the percentage of injected dose in the tumor.

The tumor growth rate (λ) can be estimated by least square fit of tumor size data of saline treated control group by:

$$N(t) = \text{const} \cdot \exp(\lambda t) \quad (5.3)$$

The D_0 is equal to:

$$D_0 = A \cdot ID_0 \cdot f_t \cdot S \quad (5.4)$$

where A is administered radioactivity (Bq), ID_0 is fraction of mean injected dose retained in tumor volume, f_t is mass fraction (mass of tumor/(mass of organ containing tumor + mass of tumor)) and S is S-value (Gy/Bq/s).

From the calculated surviving fraction the tumor volume at time t ($V(t)$) can be estimated using the relation

$$V(t) = V(t_0) \cdot SF(t) \quad (5.5)$$

Where $V(t_0)$ is measured tumor volume before injection and $SF(t)$ is surviving fraction of tumor cells at any time t . All the variables mentioned in equations(5.2, 5.3, 5.4) were calculated using the experimental data given in Ref. [31, 9, 113]. Based on the findings of Ref. [113] $\alpha = 0.0068, 0.0102, \text{ and } 0.0122 \text{ Gy}^{-1}$ were used for B16F10 melanotic melanoma

cells. For PC-3, prostate cancer, cells the surviving fraction after 2 Gy of gamma radiation is 0.7 [185] and α/β ratio is variable between 1-3 [186]. Based on this information α for PC-3 cells was calculated using the equation $SF = \exp(-\alpha D - \beta D^2)$. Lastly, the S-value for tumors is calculated using EGSnrc MC code, considering tumors as spherical volumes composed of water. The calculated values of all the variables are presented in Table 5.3 and cell survival curves (or $V(t)$) are presented in Figure 5.2.

Also, the minimum surviving fraction, SF_{min} , is generally used to estimate the efficacy of the treatment. The time at which $SF(t) = SF_{min}$ is defined as the critical time (t_c). It is the time a which the derivative of SF(t) with respect to time goes to zero:

$$\frac{d}{dt}SF(t) = SF(t) \left[\lambda - \alpha D_0 \left(\exp(-k(t - t_i)) - \exp(-m(t - t_i)) \right) \right] = 0 \quad (5.6)$$

For $t < t_c$, the tumor cell sterilization dominates over proliferation of tumor cells. Whereas, for $t > t_c$, cell proliferation dominates over the cell killing. In targeted treatments using radioactive nanoparticles, the dose rate is effected by the physical decay of radionuclides and uptake and washout rates of NPs. Initially the dose rate increases with increase in the uptake and reaches to its maximum value. After that it starts decreasing due to the washout of radioactive NPs and physical decay. The dose rate at which the rate of tumor cell killing and proliferation is balanced is termed as critical dose rate, $D(t_c)$. It can be estimated by re-writing Equation 5.6, at $t = t_c$, as:

$$D(t_c) = D_0 \left(\exp(-k(t_c - t_i)) - \exp(-m(t_c - t_i)) \right) = \frac{\lambda}{\alpha} \quad (5.7)$$

The Equation 5.7 can be solved numerically to estimate t_c . The t_c , $D(t_c)$ and SF_{min} were estimated for all cases considered in this study (see Table 5.3 and Table 5.5).

5.2.3 Radio-therapeutic efficiency of Pd-103, Sm-153 and Au-198 NPs

To compare the therapeutic efficiency of radioactive NPs three cases were considered:

1. **Case 1:** Variable administered activity: Here 0.3 cc tumor volume was assumed to be treated with variable radioactivity of 20 MBq, 40 MBq and 60 MBq. λ and α of PC-3 cells (Table 5.1), and k , m calculated from Ref. [9](Table 5.3) were used. In this work, mangiferin (MGF) was utilized as NP tumor-targeting agent. The cell survival curves for Pd-103, Sm-153 and Au-198 were calculated using Equation 5.1. The results are presented in Figure 5.3(A, B, C).

2. **Case 2:** Variable tumor volume: The activity of the radionuclides was selected such that they deposit similar absorbed dose. The activity of Pd-103 was fixed to 60 MBq (equivalent to the activity of Pd-103 brachytherapy seed). Whereas, the activity required for Au-198 and Sm-153 was estimated by using the relation: $D = S \cdot A$, where D is the absorbed dose, S is S-value and A is activity. The cell survival curves for tumor volume of 0.3, 0.6 and 1.0 cc were calculated for PC-3 cells in similar fashion as mentioned in case 1. The results are presented in Figure 5.4(A).
3. **Case 3:** Variable tumor cell type: Here we considered difference in cell lines, B16F10 ($\alpha = 0.0068 \text{ Gy}^{-1}$) and PC-3 ($\alpha = 0.059 \text{ Gy}^{-1}$) cells. The tumor volume of 0.3 cc and administered radioactivity of 600 MBq was considered for Pd-103. Here also the activity of the radionuclides was selected such that it resulted in similar absorbed dose. Hence, the activity for Au-198 and Sm-153 was estimated in similar fashion to that of Case 2. The calculated cell survival curves are presented in Figure 5.4(B).

5.2.4 MIRDcell dosimetry tool

In this study the S-values calculated using the MIRDcell, version MIRDcell V2.1, dosimetry tool [155] were used as reference. MIRDcell is a multidisciplinary tool provided by the MIRD committee of the Society of Nuclear Medicine and Molecular imaging. It can be used for bioeffect and microscale modeling purposes, such as calculation of S-values and surviving fraction, based on LQ formalism. Three type of radiation sources are supported by MIRDcell: (i) predefined MIRD radionuclides as source using full/average emission spectrum; (ii) monoenergetic particle emitter; or (iii) user defined radioactive source, and it only supports spherical volumes. We calculated cellular S-values by setting cell radius = 5 μm and nucleus radius = 4 μm . The calculations were performed for 5 source-target combinations as discussed in Section 5.2.1. Whereas, the self dose for tumors ($S(T \leftarrow T)$) was estimated by setting cell radius = 0.42 cm (for 0.3cc), 0.14 cm (for 0.6 cc) and 0.62 cm (for 1 cc) respectively and nucleus radius = 0. For both, cellular and tumor, S-value calculations full emission spectrum of predefined MIRD radionuclides: Pd-103, Sm-153 and Au-198 was used.

5.3 Results and Discussion

5.3.1 Cellular S-values

The comparison between calculated cellular S-values and the S-values calculated from MIRDcell database [155] is presented in Table 5.2. Overall, the S-values calculated using EGSnrc were found in good agreement with MIRDcell database. In case of Pd-103 for all source-target combinations ($(C \leftarrow C)$, $(C \leftarrow CS)$, $(N \leftarrow N)$, $(N \leftarrow CY)$ and $(N \leftarrow CS)$) the calculated S-values were found deviating by $\approx 14-15\%$. For Sm-153 and Au-198 deviation less than 5% was observed for $(C \leftarrow C)$, $(N \leftarrow N)$, $(N \leftarrow CY)$ and deviation $\approx 14\%$ was observed for $(N \leftarrow CS)$ and $(C \leftarrow CS)$. These variations can be due to: (i) differences in the emission spectrum used in calculation, and (ii) MIRDcell uses analytical methods for calculation of S-values. Whereas, EGSnrc performs detailed calculation by simulating the transport of electrons and photons. Ref. [181], have reported a detailed study on discrepancies in S-value caused by differences in (i) Monte Carlo codes used in calculation, (ii) emission spectrum. Seniwal et al. [181], have also reported the similar deviation of S-values.

It can be observed that Sm-153 deposits the highest S-value within the source region ($(C \leftarrow C)$ or $(N \leftarrow N)$) or in close proximity to it ($(C \leftarrow CS)$ or $(N \leftarrow CY)$). Even for the target regions $1\mu m$ far from the source region, $(N \leftarrow CS)$, Sm-153 deposits higher absorbed dose per activity to the target region in comparison to Pd-103 and Au-198. It may be because Sm-153 emits Beta particles with mean and maximum energy of 223 and 807 keV, respectively [187]. Seniwal et al. [181], also reported this behaviour for medium energy Beta particle emitters with the help of radial dose functions.

In comparison of S-values for Pd-103 and Au-198, it can be observed that for $(C \leftarrow C)$, $(N \leftarrow N)$ and $(C \leftarrow CS)$ configurations Pd-103 deposits 2-3 times higher S-value than Au-198. This may be due to the Auger electrons and low energy X-rays, 35 keV (98%) [182, 149], emitted by Pd-103. The Auger electrons, low energy X-rays do not contribute to cellular S-values [56], deposit most of their energy within the source region or target region in close proximity to the source region. Whereas, Au-198 emits high energy Beta particles, 961 keV (98.99%) [182], which deposits most of the energy far from its origin. As most of the emitted particles escape the cell volume without depositing energy the S-value is almost equal for all source-target combinations. For $(N \leftarrow CY)$ and $(N \leftarrow CS)$ Pd-103 deposits less S-value in comparison to other configurations. It may be because the Auger electrons and the secondary electrons generated by low energy X-rays are absorbed within the source region or region near it before reaching the target volume. Seniwal et al. [181] and Seftl et al. [55], have also

reported similar behaviour.

Table 5.2 Comparison of the cellular S-values (Gy/Bq/s) obtained with EGSnrc for Au-198, I-131, Pd-103, Sm-153 radionuclides with respect to MIRDcell. Five different source-target combinations were considered: ($C \leftarrow C$), ($C \leftarrow CS$), ($N \leftarrow N$), ($N \leftarrow CY$) and ($N \leftarrow CS$) (Table 5.1).

Radionuclide		$S(C \leftarrow C)$	$S(C \leftarrow CS)$	$S(N \leftarrow N)$	$S(N \leftarrow CY)$	$S(N \leftarrow CS)$
Pd-103	EGSnrc	1.39E-03 (-13.17%)	7.71E-04 (-13.22%)	2.42E-03 (-8.04%)	3.58E-04 (-14.38%)	2.47E-04 (-15.42%)
	MIRD-Cell	1.23E-03	6.81E-04	2.24E-03	3.13E-04	2.14E-04
Sm-153	EGSnrc	2.63E-03 (-2.33%)	1.34E-03 (12.99%)	4.52E-03 (0.22%)	1.16E-03 (-2.65%)	8.12E-04 (-14.04%)
	MIRD-Cell	2.57E-03	1.54E-03	4.53E-03	1.13E-03	7.12E-04
Au-198	EGSnrc	4.70E-04 (3.89%)	2.72E-04 (12.67%)	7.64E-04 (6.60%)	2.96E-04 (2.31%)	2.10E-04 (2.78%)
	MIRD-Cell	4.89E-04	3.11E-04	8.18E-04	3.03E-04	2.16E-04

*The values in round brackets represent the percentage deviation in calculated cellular S-values using EGSnrc with respect to MIRD-cell.

5.3.2 Surviving fraction and Tumor volume

Table 5.3 presents the calculated washout rate (k), uptake rate (m) of NPs, tumor growth rate (λ), tumor S-value and fraction of injected dose retained in tumor volume (ID_0) from the experimental data available in Ref. [31, 9, 113]. It also includes the critical time (t_c), critical dose rate ($D(t_c)$) and minimum survival fraction ($SF_{min}(t_c)$) calculated using Equation 5.6 and 5.7. The t_c , $D(t_c)$ and $SF_{min}(t)$ were estimated by assuming $\alpha = 0.059 \text{ Gy}^{-1}$ for PC-3 cells and $\alpha = 0.0068 \text{ Gy}^{-1}$ for B16F10 cells. As these values of α provide best agreement between the calculated and experimental cell survival (or tumor volume) curves (see Figure 5.2). From the table it can be observed that Mangiferin (MGF) functionalized Au-198 activated NPs have (a) lower washout rate, (b) higher uptake rate, and (c) equal ID_0 in comparison to cetuximab conjugated Sm-153 nanocapsules or PEG labelled Pd-103 NPs. The high value of λ and low value of α results in high $D(t_c)$ for B16F10-Luc cells in comparison to PC-3 cells. That is high dose rate, greater than the one required for PC-3 cells, is required to balance between the sterilization and proliferation of B16F10-Luc. Also, melanoma B16F10-Luc cells are more aggressive, growth rate 10 times higher than PC-3 prostate cancer cells. From these observations it can be suggested that MGF is a better targeting agent and higher doses of radiation are required to eliminate B16F10 cells in comparison to PC-3 cells.

Table 5.3 Effective NP washout rate ($k[day^{-1}]$), uptake rate ($m[day^{-1}]$), tumor growth rate ($\lambda[day^{-1}]$), S-value [Gy/Bq/day], ID_0 were calculated using the method explained in section 2 and Table 5.1. Also, critical time (t_c [day]), critical dose rate ($D(t_c)$ [Gy/hr]) and minimum survival fraction ($SF_{min}(t_c)$) were calculated considering $\alpha = 0.059 Gy^{-1}$ for Pd-103 and Au-198, and for Sm-153 $\alpha = 0.0068 Gy^{-1}$.

	L-Pelletier et al., 2017 (Pd-103)	Wang et al., 2020 (Sm-153)	Katti et al., 2018 (Au-198)
$k [day^{-1}]$	0.55	0.63	0.38
$m [day^{-1}]$	26.70	31.20	84.00
$\lambda [day^{-1}]$	4.08E-02	4.37E-01	5.00E-02
S-value [Gy/Bq/s]	4.78E-12	7.58E-10	1.29E-09
ID_0	0.8	0.8	0.8
t_c [day]	7.00	6.02	9.2
$D(t_c)$ [Gy/hr]	2.88E-02	2.66	3.53E-02
$SF_{min}(t_c)$	0.21	0.65	0.21

The calculated cell survival curves, using Equation 5.1, and the tumor volume, using Equation 5.5 are illustrated in Figure 5.2, as well as the experimental data extracted from previously published work [31, 9, 113]. Globally all calculated and experimental curves show similar trend. However, some discrepancies are observed in early days (or weeks) of treatment. One hypothesis is that even if cell death starts to occur very early from the start of treatment, it must take some time for the tissue architecture to reorganize and a decrease in the volume of the tumor to be observed. This may be one of the causes of the delay in the tumor volume shrinkage observed in the experiments in relation to the calculated one. Reader must note that in these calculations NPs are treated as isotropic point sources uniformly and randomly sampled within the tumor volume. This may be a reasonable assumption for tumor volumes of size in cubic centimeters as the dimensions of nanoparticles are smaller by order of 10^{-7} in comparison to tumor size (diameter). Also the NPs with diameter in the range of 15-30 nm (with hydrodynamic diameter of 30-80 nm) can easily penetrate the vasculature of tumor and transport therapeutic payload to the tumor cells [9]. According to the findings of Ref. [33], after intratumoral injection within 24 hours the NPs, carried in aqueous solution, diffuse slightly from the injection site within the extracellular matrix before getting internalized in the cell. However, it may not be a good assumption at cellular level, because the NPs accumulate within the cellular vesicles which are not uniformly distributed [33]. Also, it must be noted that in most of the pre-clinical studies available in literature Au is considered as biocompatible material to deliver radionuclides to the tumor cells, and do not investigate the dose enhancement or self absorption caused by Au. However, Ref. [31] used Pd-103 NPs coated with Au in order to exploit the enhancement in dose due

to radiosensitization. In the calculations performed in this study we also do not consider the self absorption [188, 189] or dose enhancement [163, 162, 165, 164] by material of NPs. However, the radionuclides: Pd-103, Sm-153 and Au-198 along with electrons emit photons of energy 20.6 keV (average) [190], 103 keV (28%) [191] and 411 keV (93%) [192]. These emitted photons/electrons on interaction with material of NPs, Au, can result in radiosensitization/self absorption. Consequently, it may result in increase/decrease in total absorbed dose within the tumor. The increase/decrease in tumor absorbed dose can lead to over-estimation/under-estimation of reduction in tumor volume.

Figure 5.2(A) illustrates the comparison between the calculated tumor volume and experimental data for Pd-103 NPs conjugated with PEG. The day -7 in Figure 5.2(A) represents the day of measuring tumor volume before intratumoral injection (t_0) and day of injection (t_i) is day 0. The calculations consider PC-3 cell lines, $\alpha = 0.059, 0.089$ and 0.107 Gy^{-1} . The best agreement was observed for $\alpha = 0.059 \text{ Gy}^{-1}$, with $t_c = 7.0$ days, and $SF_{min} = 0.21$. The reduction in tumor volume is over-estimated for $\alpha = 0.089$ and 0.107 Gy^{-1} (results not shown). The Pd-103 NPs used by Ref. [31] had radioactive core of Pd-103 coated with gold (Au). Hence, the disagreement between the calculated and experimental curve might be consequence of not considering self-absorption or radiosensitization effect of Au. More detail on impact of size and concentration of AuNPs, and localization of NPs on radiosensitization for Pd-103 (brachytherapy seeds) can be found elsewhere [190]. Also, the mathematical model used in this study assumes, considering near complete repair of sublethal damage, a cell survival curve as an exponentially decreasing function of dose. However, a fully comprehensive model should include the quadratic mediated cell killing and Lea-Catcheside time factor [172], G-factor, to account for DSB repair. Similarly, Figure 5.2(B) illustrates the comparison between the calculated data and experimental data in terms of relative tumor volume (or surviving fraction). In Figure 5.2(B) t_0 is day 3 and t_i is day 4. The calculations were performed for $\alpha = 0.0068, 0.0102$ and 0.0122 Gy^{-1} , B16F10 cell lines and the best agreement between the experimental and calculated results was for $\alpha = 0.0068 \text{ Gy}^{-1}$, with $t_c = 6.02$ days, and $SF_{min} = 0.65$. Figure 5.2(C, D) reports the tumor volume and cell survival curves for Au-198 NPs, activated by neutron activation of Au, functionalized with MGF. In case of Figure 5.2(C, D) t_0 is day 2 and t_i is day 2. Also, Figure 5.2 (C) includes two set of experimental data, Katti et al. 2018 (1) and Katti et al. 2018 (2), published in [9]. The calculations were performed for $\alpha = 0.059, 0.089$ and 0.107 Gy^{-1} , PC-3 cell lines. The best agreement between the experimental and calculated results was for $\alpha = 0.059 \text{ Gy}^{-1}$, with $t_c = 7.0$ days, and $SF_{min} = 0.21$. The discrepancies between calculated tumor volume curve and experimental data may be because we did not consider self-absorption or radiosensiti-

zation effect of Au. Other possible reasons for discrepancies between the calculated and experimental data are: (a) unavailability of detailed pharmacokinetic data, which affects the calculation of k and m (consequently the calculations), (b) large standard deviation in published experimental data, (c) discrepancies in emission spectrum used in calculations.

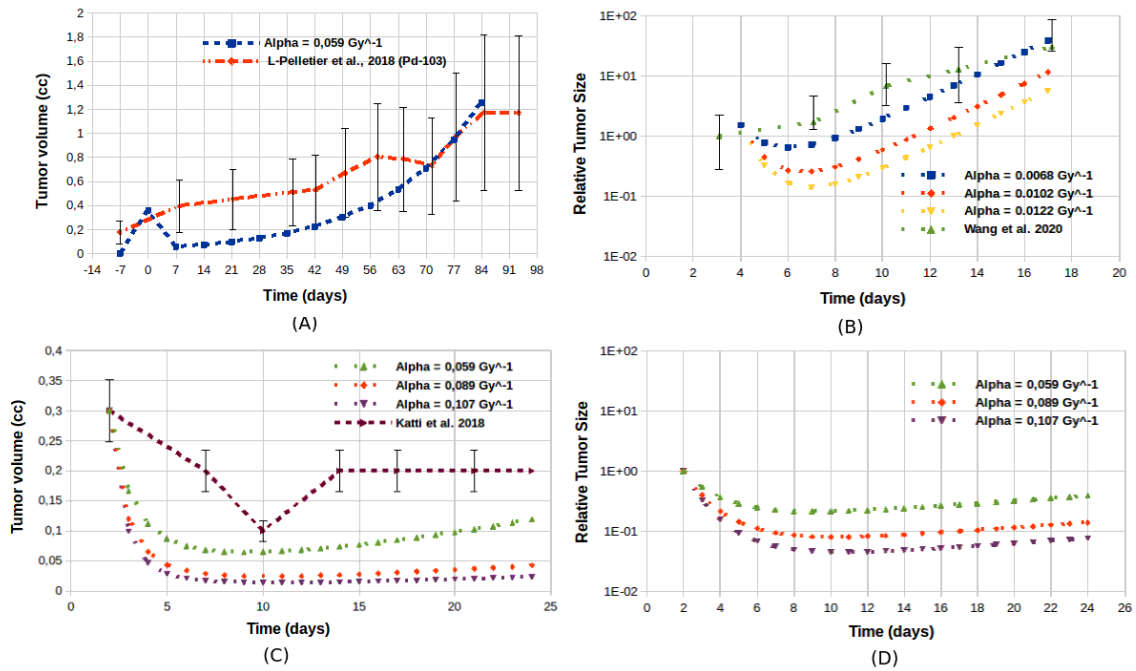


Figure 5.2 Comparison between calculated (A) tumor volume and L-Pelletier et al., 2018, (B) cell survival curve and Wang et al., 2020, (C) tumor volume and Katti et al., 2018, (D) expected cell survival curve for Katti et al., 2018.

5.3.3 Comparison of radiotherapeutic efficiency of Pd-103, Sm-153 and Au-198 NPs

The comparison of S-values calculated using EGSnrc MC code and extracted from MIRDcell database [155], for spherical tumors of volume 0.3, 0.6 and 1.0 cc using Pd-103, Sm-153 and Au-198 is illustrated in Table 5.4. In these calculations tumor acted both as source and target :($T \leftarrow T$). The difference between the EGSnrc calculated S-values and MIRDcell database for Au-198 and Sm-153 was within 5%. However, for Pd-103 the difference up to 55%, with respect to MIRDcell, was observed. In order to investigate the cause of such high deviation we extracted the emission spectrum of Pd-103 from MIRDcell database and used it to esti-

mate S-values using EGSnrc (not presented here). The calculated S-values, using emission spectrum from MIRDCell, were found equal to the S-values extracted from MIRDCell. Thus, the deviation observed between the MIRDCell database and EGSnrc calculated S-values, for Pd-103 (Table 5.4), is caused by discrepancies in emission spectrum.

Table 5.4 Comparison of calculated S-values (Gy/Bq/s) for different sizes of tumor using EGSnrc with respect to MIRDCell.

	0.3 cc	0.6 cc	1.0 cc
S($T \leftarrow T$): Au-198	1.57E-10 (-5.37%)	8.11E-11 (-4.70%)	4.98E-11 (-4.40%)
MIRDCell	1.49E-10	7.75E-11	4.77E-11
S($T \leftarrow T$): Sm-153	1.36E-10 (-2.18%)	6.90E-11 (-1.02%)	4.20E-11 (-1.11%)
MIRDCell	1.33E-10	6.83E-11	4.15E-11
S($T \leftarrow T$): Pd-103	4.36E-12 (-39.24%)	2.30E-12 (-47%)	1.46E-12 (-55.5%)
MIRDCell	3.13E-12	1.56E-12	9.37E-13

From the calculated S-values it can be observed that Au-198 and Sm-153 deposit nearly equal absorbed dose per activity in all tumor volumes, whereas, according to Table 5.2 Au-198 calculated S-values were lowest. This discrepancy is because at cellular level the high energy Beta particles emitted by Au-198 deposit most of their energy out of the cell. However, in this case all the emitted beta particles deposit their energy within the tumor volume. Pd-103 emissions are composed mainly of low energy monoenergetic photons and electrons and lack the relative high energy Beta emissions of Sm-153 and Au-198. Thus it can be explained why the Pd-103 deposits almost 10-100 times less S-value in comparison to Au-198 and Sm-153. So, it can be expected that higher radioactivity of Pd-103 is required to achieve radiotherapeutic effects similar to Au-198 and Sm-153.

The calculated critical time (t_c), critical dose rate ($D(t_c)$) and $SF_{min}(t_c)$, using Equation 5.6 and Equation 5.7, for three cases considered to compare the radiotherapeutic efficiency of Pd-103, Sm-153 and Au-198 NPs (described in section 5.2.3) is presented in Table 5.5.

Table 5.5 The critical time (t_c) [days], critical dose rate ($D(t_c)$) [Gy/hr] and $SF_{min}(t_c)$ calculated for variable tumor size (cc), type, administered activity [MBq] and radionuclide.

Case#	Radionuclide	Activity [MBq]	Tumor Type	Volume [cc]	t_c [days]	$D(t_c)$ [Gy/hr]	$SF_{min}(t_c)$	
1	Pd-103	20	PC3	0.30	8	3.53E-02	4.81E-01	
		40			9.5		1.67E-01	
		60			10.5		5.57E-02	
	Au-198	20	PC3	0.30	17	3.53E-02	3.00E-18	
		40			19		4.08E-36	
		60			20		5.35E-54	
	Sm-153	20	PC3	0.30	16.7	3.53E-02	6.66E-16	
		40			18.5		2.05E-31	
		60			19.5		6.06E-47	
	2	Pd-103	60	PC3	0.30	10.5	3.53E-02	5.51E-02
			60		0.60	8.9		2.59E-01
			60		1.00	7.7		4.77E-01
Au-198		0.17	PC3	0.30	10.5	3.53E-02	5.51E-02	
		0.17		0.60	8.9		2.59E-01	
		0.18		1.00	7.7		4.77E-01	
Sm-153		0.19	PC3	0.30	10.5	3.53E-02	5.51E-02	
		0.2		0.60	8.9		2.59E-01	
		0.21		1.00	7.7		4.77E-01	
3		Pd-103	600	PC-3	0.3	14.4	3.53E-02	2.28E-15
			600	B16F10	0.3	9.1	2.68E-01	8.93E-16
		Au-198	16.7	PC-3	0.3	14.4	3.53E-02	2.28E-15
	16.7		B16F10	0.3	9.1	2.68E-01	8.93E-16	
	Sm-153	19.2	PC-3	0.3	14.4	3.53E-02	2.28E-15	
		19.2	B16F10	0.3	9.1	2.68E-01	8.93E-16	

Case 1: Variable radioactivity administered

From Table 5.5 it can be observed that when tumor, 0.3 cc, with PC-3 cell is treated with variable activity of 20, 40 and 60 MBq, for all radionuclides with increase in administered activity there is increase in t_c and decrease in $SF_{min}(t_c)$. That is, the dose rate remains higher than $D(t_c)$ for a longer period of time when higher activities are administered. Since, $D(t_c)$ depends on tumor growth rate (λ) and radiosensitivity factor (α), it has a constant value of 3.53 cGy/hr. The decrease in $SF_{min}(t_c)$ is maximum for Au-198 (up to 5.35E-54) and minimum for Pd-103 (up to 5.57E-02). The value of t_c is almost equal for Au-198 and Sm-153 (≈ 20 days for 60 MBq), which is almost 7 times of their physical half life. Whereas, for Pd-103 the value of t_c is 10.5 days (for 60 MBq), which is less than one physical half life. It may be because of low dose rate of Pd-103 which cannot withstand the tumor proliferation rate for more than 10 days. Also, from the cell survival curves presented in Figure 5.3(A, B, C), it can be observed that activity between 40-60 MBq of Pd-103 is required to treat 0.3 cc

tumor. On the other hand, Sm-153 and Au-198, as medium and high energy Beta emitters, are capable of treating 0.3 cc tumors with activity as low as 20 MBq.

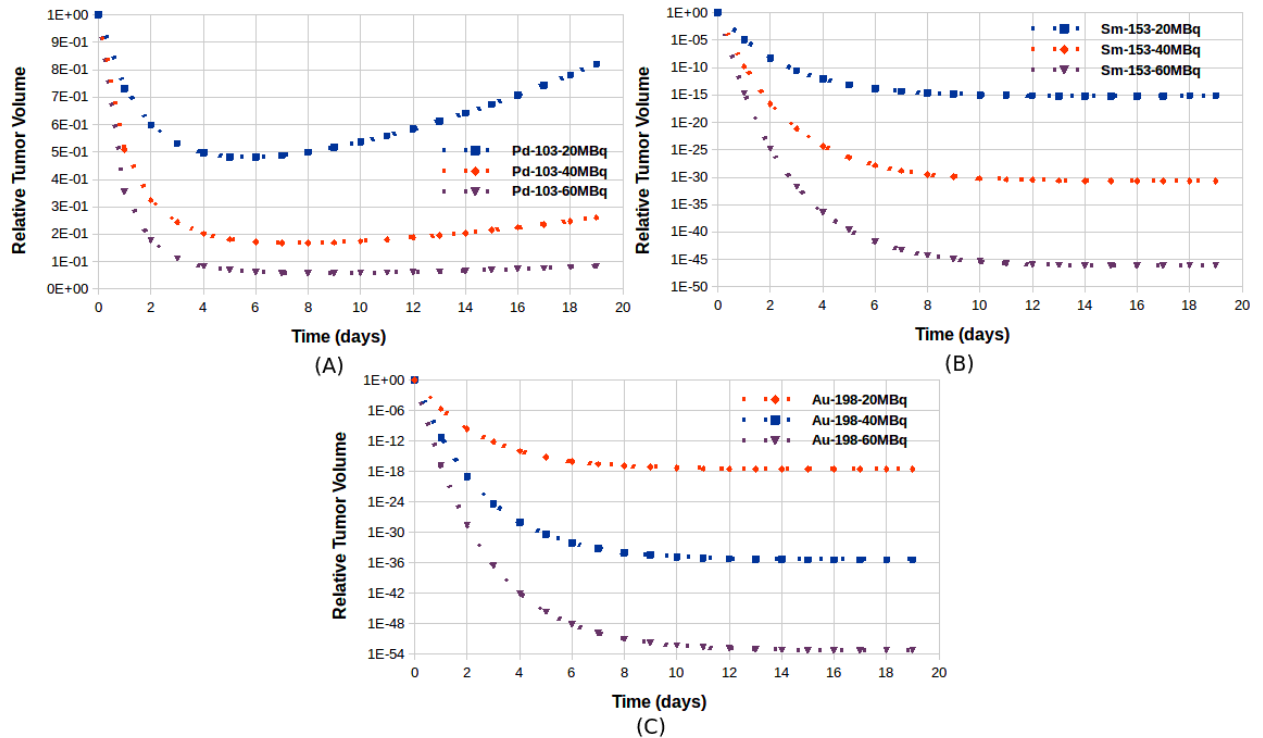


Figure 5.3 Comparison of radiation therapeutic efficiency of Pd-103, Sm-153, and Au-198 NPs (A, B, C) considers constant tumor volume of 0.3cc and administered radioactivity of 20, 40, 60MBq.

Case 2: Variable tumor volume

Here the therapeutic efficacy of Pd-103, Sm-153 and Au-198, variable administered activity and similar absorbed dose, was compared for variable tumor (PC-3 cell lines) sizes: 0.3, 0.6 and 1.0 cc. The administered activity, keeping 60 MBq of Pd-103 as reference, for other radionuclides was selected such that they deposited equal dose, using the relation $Dose = S\text{-value}(T \leftarrow T) \times Activity$. It was found that ≈ 0.2 MBq of Au-198 and Sm-153 is required to deposit same dose as deposited by 60 MBq of Pd-103 (See Table 5.5). Since, all radionuclides deposited similar absorbed dose, similar cell survival curves, t_c and $SF_{min}(t_c)$ were obtained. The cell survival curves obtained using Pd-103 are presented in Figure 5.4(A). It can be observed that 60 MBq of Pd-103 effectively treats 0.3 cc tumor ($t_c = 10.5$ days and $SF_{min}(t_c) = 5.5E-02$). Also, with increase in tumor volume, there is decrease in t_c (10.5 days to 7.7 days) and increase in $SF_{min}(t_c)$ (0.055 to 0.5). Hence, it can be suggested

that higher activities of Pd-103 are required to ablate 1.0 cc tumors, as tumor repopulation rate overtakes cell killing in 7.7 days (less than 1 half life), $t_c = 7.7$ days and $SF_{min}(t_c) = 0.477$.

Case 3: Variable tumor cell type

Figure 5.4(B) reports the cell survival curves for two different kind of tumors: (a) PC-3 prostate cancer cells, and (b) highly aggressive B16F10 melanotic melanoma cells, treated with 600 MBq of Pd-103. Here also the comparison of therapeutic efficiency was made considering that all radionuclide deposited equal absorbed dose and activity required for Au-198 and Sm-153 was estimated considering 600 MBq of Pd-103 as reference. It was found that 16.7 MBq, 19.2 MBq and 600 MBq of Au-198, Sm-153 and Pd-103 deposit equal absorbed dose to 0.3 cc tumor volume, and same absorbed dose resulted in similar cell survival curves. From Table 5.5, it can be observed that with increase in radioresistance and growth rate of tumor cells there is increase in $D(t_c)$ and $SF_{min}(t_c)$ and decrease in t_c . Also, from the Figure 5.4(B) it can be appreciated that 600 MBq of Pd-103 almost completely ablate PC-3 tumor cells, $t_c = 14.4$ days and $SF_{min}(t_c) = 2.28E-15$. Whereas, in case of B16F10 melanoma cells the cell sterilization could not withstand cell repopulation rate after 9 days (t_c) with $SF_{min}(t_c) = 8.93E-16$.

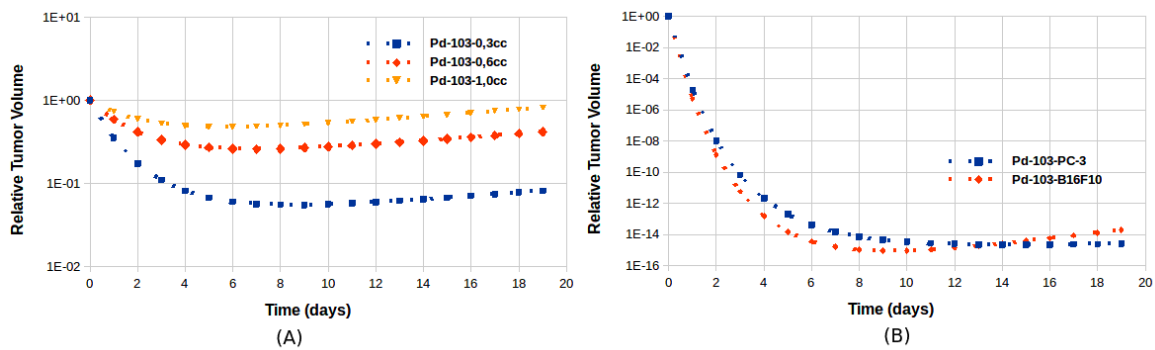


Figure 5.4 Comparison of radiation therapeutic efficiency of Pd-103 considering administered radioactivity of (A) 60MBq to tumor volume, PC-3 cell lines, of 0.3, 0.6 and 1.0 cc (B) 600 MBq to constant tumor volume of 0.6cc of two different cell lines PC-3 and B16F10.

In comparison it was found that (a) Au-198 has the highest dose rate (deposited highest dose per activity), (b) Au-198 and Sm-153 effectively reduce the cell surviving fraction of radioresistant tumors of size 0.3, 0.6 and 1.0 cc with low administered activity compared to Pd-103. Hence, it can be suggested that for large tumors Au-198 and Sm-153 are more

effective than Pd-103.

5.4 Conclusion

The radioactive nanoparticles (NPs) have been reported as an alternative to low-dose-rate seed-based brachytherapy (BT). In this study we performed dosimetric calculations for NPs activated with Pd-103, Sm-153 and Au-198. The calculation was performed in three steps: (A) Single cell dosimetry: the cellular S-values were calculated and compared with MIRDcell [155] database; (B) Cell survival (or tumor volume) curve calculations: the cell survival (or tumor volume) curves were calculated using Equation (5.1) (or Equation (5.5)) and compared with experimental data published in literature [31, 9, 113]; (C) The radiotherapeutic efficiency of these NPs were tested for variable (i) administered radioactivity, (ii) tumor volume, and (iii) tumor cell type.

At cellular level low energy X-ray emitter (Pd-103) and medium energy Beta-particle emitter (Sm-153) deposited maximum dose per activity within the cell. Whereas, the high energy Beta particles emitted from Au-198 leave the cell volume without depositing much energy. Also, the findings of this study support the mathematical model used to calculate the cell survival curves. It is able to reproduce the experimental results to a great extent. Better knowledge of uptake rate, washout rate of NPs, radiosensitivity and growth rate of tumors is important for these calculations. Also, self absorption of emitted radiation by NPs and dose enhancement caused by AuNPs must be considered in cell survival curve calculations.

Au-198 and Sm-153 effectively ablate large (1.0 cc), radio-resistant and aggressive tumors. However, considering the activity range studied here Pd-103 is only suitable for treatment of millimeter size tumors. Also, the use of MGF as targeting agent shows great potential over cetuximab and PEG due to its high uptake rate and low washout rate.

5.5 Acknowledgments

The following Brazilian institutions support this research project: Research Support Foundation of the State of Minas Gerais (FAPEMIG), Brazilian Council for Scientific and Technological Development (CNPq) and Coordination for the Capacitation of Graduated Personnel

(CAPES). Prof. T. Fonseca is grateful for financial support provided by CNPq (processo no. 450493/2019-9) and FAPEMIG (Projeto APQ-00083-18 Processo no. 2070.01.0002992/2018-30). Dr. Lucas F. Freitas and Prof A. B. Lugão would like to thank Fundação de Amparo á Pesquisa do Estado de São Paulo for the financial support (grant no. 2018/15598-2).

Chapter 6

Conclusion and Future Directions

6.1 Conclusion:

For successful ablation of cancer cells the radiotherapeutic agent must interact at the cellular level and must be uniformly distributed within the tumor volume. Recently, with the advancements in nanotechnology, some research groups have reported preclinical studies, on both mice and dog models, using radioactive nanoparticles (NPs). These radioactive nanosized, size in the range of 15-30 nm (hydrodynamic size of 30-85 nm), particles, injected through intratumoral injection, are expected to penetrate the tumor vasculature and deliver optimum payloads to the tumor volume for complete remission of the primary tumor cells.

This PhD thesis aims to perform dosimetry of these radioactive nanoparticles, used for low dose rate (LDR) brachytherapy applications, using Monte Carlo (MC) methods. Two widely used MC codes: (i) EGSnrc, and (ii) Geant4-DNA were used in this work. The formalism provided by Medical Internal Radiation Dose (MIRD) committee in their report "MIRD pamphlet No. 21" was used in estimation of absorbed dose per unity activity (also known as S-value). The whole research work was performed and published in the form of four articles (chapter 2-5 of this thesis).

The first study (chapter 2 of this thesis), aimed to test the accuracy of Geant4-DNA and EGSnrc MC codes with respect to other commonly used, for radiation physics dosimetry, MC codes: MCNP6, PENELOPE, and FLUKA. The electron range (penetration depth) and dose point kernel (DPK) for electrons with initial energy from 1 keV up to 50 keV, using Equation 2.1, were estimated using above mentioned MC codes. The impact of differences in the DPK on the absorbed dose (using Equation 2.2) was also investigated. Results obtained from all five MC codes for electron range and DPK showed an overall similar trend, the

maximum differences in electron range and DPK were observed for electrons with initial energy less than 10 keV. These differences affect the dose distribution at microscopic scale, and no impact is observed in millimeter sized voxels. Hence, it can be concluded that while performing microdosimetry the accuracy of MC codes and its MC parameter settings must be benchmarked and validated.

The aim of the second study was to test the accuracy of EGSnrc MC code for electrons in the energy range of 50 keV to 3 MeV, covers the entire energy range of the beta-emitting radionuclides used for targeted radionuclide therapy (TRT) or seed based brachytherapy applications. For this the comparison was performed in terms of DPK (using Equation 3.1) for monoenergetic electron sources and beta-emitting radionuclides, using their emission spectrum as input. The DPK calculated using EGSnrc was compared against MCNP6, PENELOPE and TOPAS MC codes. It was found that in case of monoenergetic, isotropic, point electron sources, the differences between the estimated DPK, using above mentioned 4 MC codes, on average were less than 5%. Whereas, using emission spectrum of beta emitting radionuclides as source resulted in differences, between estimated DPKs, less than 3%. Hence, it was concluded that EGSnrc is suitable in performing dosimetry in the 50 keV to 3 MeV energy range. It was also concluded the in order to test the accuracy of MC code the comparison must be made in terms of DPK of monoenergetic electrons. It is because the use of emission spectrum tend to smooth the results and can hide the differences.

The third study aimed to investigate the therapeutic efficacy of alpha, beta and Auger emitters for theranostic applications. The commonly used method of single cell dosimetry was used and the cellular S-values were estimated for 12 selected radionuclides using EGSnrc and Geant4-DNA MC codes (using Equation 4.1). The localized dose deposition property of Auger emitters and cross fire effect of beta emitting radionuclides was shown graphically, by calculating radial dose functions. Such graphical representation of energy deposition is important because it provides clear insight regarding the distribution of the radioactivity in source region. According to MIRD formalism the radioactivity should be randomly and uniformly distributed within the source region. Furthermore, the mean absorbed dose cannot be the right parameter to represent the distribution of radioactivity. It is because if the same number of points are sampled (following MIRD recommendations or not) within a particular volume, it may result in same mean absorbed dose. Hence, the discrepancies in activity distributions can only be observed through graphical methods. The alpha emitters deposited highest absorbed dose in comparison to Auger and beta emitters. It was concluded that care must be taken while using the internal modules of EGSnrc or Geant4-DNA to simulate the

decay of radionuclides while performing such single cell dosimetry. It was also concluded that the single cell dosimetry is suitable in evaluating the therapeutic efficacy of alpha and Auger emitters. Whereas, the electrons emitted by beta emitters deposit most of their energy out of the cell geometry (detector volume), sphere of radius $5 \mu m$. Hence, while checking the therapeutic efficacy of beta emitting radionuclides for brachytherapy application maybe single cell dosimetry is not an effective method of evaluation.

The last part, chapter 5 of this thesis, of the work was focused on performing the dosimetry for experimental preclinical studies published in literature. The aim of the study was to reproduce the published experimental results (using Equation 5.1), in terms of cell survival curves, using a mathematical model. Such study can be a handy and easy to use guide for preclinical studies based on use of radioactive NPs for LDR Brachytherapy applications. It can be useful in selection of radionuclides and administration activity based on the volume growth rate and radiosensitivity of the tumor. Moreover, taking into account the washout and uptake rate of these radioactive nanocarriers. We estimated the cell survival curves, and evaluated the therapeutic efficacy of Pd-103 (Auger emitter), Sm-153 (medium energy beta emitter) and Au-198 (high energy beta emitter) using the mathematical model proposed by Sefl et al. (2016). The applied methodology to estimate the cell survival curves was able to reproduce the experimental curves. It was concluded that accurate knowledge of uptake rate, washout rate of NPs, radiosensitivity and growth rate of tumors is crucial for these calculations. Also, Au-198 and Sm-153 effectively ablate large (1.0 cc), radio-resistant and aggressive tumors (both PC-3 cells $\alpha = 0.06 \text{ Gy}^{-1}$, and B16F10 cells $\alpha = 0.006 \text{ Gy}^{-1}$). However, considering the activity range used, Pd-103 is only suitable for treatment of millimeter size tumors. Based on above conclusion it may appear that it would not be possible to treat whole prostate, breast cancers or eye melanoma using Pd-103. For this it should be noted that in this case low activities of Pd-103 were used ($60 \text{ MBq} \approx 1 \text{ Pd-103 seed}$). Whereas, in general permanent seed brachytherapy applications approximately 50-100 seeds of Pd-103 are implanted. Our findings do conclude that with higher doses of radioactivity it is possible to treat large volumes of tumor with Pd-103.

From dosimetric point of view, our work, presented in chapter 2-5 of this thesis, generated a solid base for dosimetry of LDR brachytherapy applications using radioactive nanoparticles. We have validated the electron transport algorithm of both EGSnrc and Geant4-DNA for electron energy ranging from 1 keV to 3 MeV. Compared the therapeutic efficacy of 12 selected radionuclide: low-, medium-, and high energy beta, Auger and alpha emitters for theranostic applications, using the commonly used approach of single cell dosimetry. Lastly,

using all the information gathered in terms of: (i) correct MC parameters setting for accurate estimation of absorbed dose, (ii) impact of discrepancies in emission spectrum on computed absorbed dose, the *in-silico* dosimetry was performed and the cell survival published in literature (experimental) were reproduced using mathematical model. We believe this contribution will be helpful in future progress in the dosimetry of radioactive nanoparticles of LDR BT applications.

6.2 Future Directions

This PhD thesis has laid a solid foundation in the direction of dosimetry of LDR brachytherapy applications using radioactive nanoparticles. But still there are many unanswered questions left for the future. The future work concerns deeper analysis of methods presented in this thesis, new proposals to try different methods, or simply curiosity.

Some of the research questions that I think can be explored are:

1. Chapter 4 we used simple spherical cell geometry to estimate the therapeutic efficacy of different radionuclides. And in chapter 5 we used spherical tumor geometry to predict the cell survival curves. However, these spherical geometries are very far from the realistic scenario. The use of realistic models of tumor/cell can provide better insight and understanding of the problem.
2. The mathematical model we used to predict in chapter 5, approximated cell survival as exponentially decreasing function of total dose. However, a fully comprehensive model should include: (i) the quadratic mediated cell killing, (ii) consider the repair of double strand breaks, and (iii) heterogeneity in terms of radiosensitivity tumor cells as a function of time.
3. Considering the fact that cell killing after radiation exposure and interaction of radiation are stochastic in nature. Today Monte Carlo codes such as: Geant4-DNA/TOPAS-nBio has potential to simulate radiobiological processes. Hence, full Monte Carlo based setup can be used to model the absorbed dose, DNA damage (and estimating the cell survival curves). The cell survival curves estimated by this approach might be more closer representation of reality. However, the application of rate of uptake and washout rate of nanoparticles can

be still challenging with currently available Monte Carlo tools.

4. Also, most of the preclinical studies make use of high Z nanoparticles for LDR brachytherapy applications, for example use of radioactive gold NPs. The interaction of emitted radiation with the material of NPs is expected to result in radiosensitization/self absorption. This radiosensitization/self absorption depends on many factors, such as size and concentration of NPs. Hence, overlooking the radiosensitization/self absorption property of high-Z NPs can result in inaccurate dose predictions.
5. In chapter 4 and chapter 5 we have shown that the discrepancies in emission spectrum has a large impact on the computed absorbed dose, for example, the emission spectrum provided by NNDC and ICRP for Pd-103 are different in terms of Auger emissions and this difference results in discrepancies in calculated absorbed dose as high as 50% or more. Hence, it is very important to find the solution, either better documenting of the source of emission spectrum or finding a reliable solution that can be used to circumvent the impact of differences in emission spectrum on absorbed dose.

Bibliography

- [1] Lois B Travis. Therapy-associated solid tumors. *Acta oncologica*, 41(4):323–333, 2002.
- [2] Cyrus Chargari, Eric Deutsch, Pierre Blanchard, Sebastien Gouy, H el ene Martelli, Florent Gu erin, Isabelle Dumas, Alberto Bossi, Philippe Morice, Akila N Viswanathan, et al. Brachytherapy: An overview for clinicians. *CA: a cancer journal for clinicians*, 69(5):386–401, 2019.
- [3] Ratul Mukerji, Jeffrey Schaal, Xinghai Li, Jayanta Bhattacharyya, Daisuke Asai, Michael R Zalutsky, Ashutosh Chilkoti, and Wenge Liu. Spatiotemporally photoradiation-controlled intratumoral depot for combination of brachytherapy and photodynamic therapy for solid tumor. *Biomaterials*, 79:79–87, 2016.
- [4] Kohei Sano, Yuko Kanada, Kengo Kanazaki, Ning Ding, Masahiro Ono, and Hideo Saji. Brachytherapy with intratumoral injections of radiometal-labeled polymers that thermoresponsively self-aggregate in tumor tissues. *Journal of Nuclear Medicine*, 58(9):1380–1385, 2017.
- [5] Nikolaos Zamboglou, Nikolaos Tselis, Dimos Baltas, Thomas Buhleier, Thomas Martin, Natasa Milickovic, Sokratis Papaioannou, Hanns Ackermann, and Ulf W Tunn. High-dose-rate interstitial brachytherapy as monotherapy for clinically localized prostate cancer: treatment evolution and mature results. *International Journal of Radiation Oncology* Biology* Physics*, 85(3):672–678, 2013.
- [6] Yasuo Yoshioka, Takayuki Nose, Ken Yoshida, Takehiro Inoue, Hideya Yamazaki, Ei-ichi Tanaka, Hiroya Shiomi, Atsushi Imai, Satoaki Nakamura, Shigetoshi Shimamoto, et al. High-dose-rate interstitial brachytherapy as a monotherapy for localized prostate cancer: treatment description and preliminary results of a phase i/ii clinical trial. *International Journal of Radiation Oncology* Biology* Physics*, 48(3):675–681, 2000.
- [7] James Dolan, Zuofeng Li, and Jeffrey F Williamson. Monte carlo and experimental dosimetry of an brachytherapy seed. *Medical physics*, 33(12):4675–4684, 2006.
- [8] Eric Barbarite, Justin T Sick, Emmanuel Berchmans, Amade Bregy, Ashish H Shah, Nagy Elsayyad, and Ricardo J Komotar. The role of brachytherapy in the treatment of glioblastoma multiforme. *Neurosurgical review*, 40(2):195–211, 2017.
- [9] Katti et al. Prostate tumor therapy advances in nuclear medicine: green nanotechnology toward the design of tumor specific radioactive gold nanoparticles. *Journal of Radioanalytical and Nuclear Chemistry*, 318(3):1737–1747, 2018.

- [10] Jeremy G Price, Nelson N Stone, and Richard G Stock. Predictive factors and management of rectal bleeding side effects following prostate cancer brachytherapy. *International Journal of Radiation Oncology* Biology* Physics*, 86(5):842–847, 2013.
- [11] Byron H Lee, Adam S Kibel, Jay P Ciezki, Eric A Klein, Chandana A Reddy, Changhong Yu, Michael W Kattan, and Andrew J Stephenson. Are biochemical recurrence outcomes similar after radical prostatectomy and radiation therapy? analysis of prostate cancer–specific mortality by nomogram-predicted risks of biochemical recurrence. *European urology*, 67(2):204–209, 2015.
- [12] Corrado Gallo Curcio, Carla Vasile, Antonio Gianciotta, Alessandro Casali, Tommaso Gionfra, Massimo Rinaldi, Alfredo Guadagni, Vittorio Le Pera, and Ercole Segà. Short-term results of combined radioimmunotherapy in inoperable lung cancer. *Tumori Journal*, 62(6):587–597, 1976.
- [13] Vinod Kumar Khanna. Targeted delivery of nanomedicines. *International Scholarly Research Notices*, 2012, 2012.
- [14] Daniel Rosenblum, Nitin Joshi, Wei Tao, Jeffrey M Karp, and Dan Peer. Progress and challenges towards targeted delivery of cancer therapeutics. *Nature communications*, 9(1):1–12, 2018.
- [15] George N Sfakianakis and FH DeLand. Radioimmunodiagnosis and radioimmunotherapy, 1982. *Journal of Nuclear Medicine*, 23(9):840–850, 1982.
- [16] Priyanka Ganguly, Ailish Breen, and Suresh C Pillai. Toxicity of nanomaterials: exposure, pathways, assessment, and recent advances. *ACS Biomaterials Science & Engineering*, 4(7):2237–2275, 2018.
- [17] Eşref Demir. A review on nanotoxicity and nanogenotoxicity of different shapes of nanomaterials. *Journal of Applied Toxicology*, 41(1):118–147, 2021.
- [18] David M Goldenberg, Chien-Hsing Chang, Edmund A Rossi, et al. Pretargeted molecular imaging and radioimmunotherapy. *Theranostics*, 2(5):523, 2012.
- [19] Jean-Pierre Pouget, Catherine Lozza, Emmanuel Deshayes, Vincent Boudousq, and Isabelle Navarro-Teulon. Introduction to radiobiology of targeted radionuclide therapy. *Frontiers in medicine*, 2:12, 2015.
- [20] Encouse B Golden and Lionel Apetoh. Radiotherapy and immunogenic cell death. In *Seminars in radiation oncology*, volume 25, pages 11–17. Elsevier, 2015.
- [21] Lawrence E Williams, Gerald L DeNardo, and Ruby F Meredith. Targeted radionuclide therapy. *Medical physics*, 35(7Part1):3062–3068, 2008.
- [22] Mostafa Sefidgar, Madjid Soltani, Kaamran Raahemifar, Hossein Bazmara, Seyed Mojtaba Mousavi Nayinian, and Majid Bazargan. Effect of tumor shape, size, and tissue transport properties on drug delivery to solid tumors. *Journal of biological engineering*, 8(1):1–13, 2014.
- [23] Seong Hoon Jang, M Guillaume Wientjes, Dan Lu, and Jessie L-S Au. Drug delivery and transport to solid tumors. *Pharmaceutical research*, 20(9):1337–1350, 2003.

- [24] N Tselis, P Hoskin, D Baltas, V Strnad, N Zamboglou, C Rödel, and G Chatzikonstantinou. High dose rate brachytherapy as monotherapy for localised prostate cancer: review of the current status. *Clinical Oncology*, 29(7):401–411, 2017.
- [25] Dong Soo Park. Current status of brachytherapy for prostate cancer. *Korean journal of urology*, 53(11):743, 2012.
- [26] Nripen Chanda, Vijaya Kattumuri, Ravi Shukla, Ajit Zambre, Kavita Katti, Anandhi Upendran, Rajesh R Kulkarni, Para Kan, Genevieve M Fent, Stan W Casteel, et al. Bombesin functionalized gold nanoparticles show in vitro and in vivo cancer receptor specificity. *Proceedings of the National Academy of Sciences*, 107(19):8760–8765, 2010.
- [27] Sandra M Axiak-Bechtel, Anandhi Upendran, Jimmy C Lattimer, James Kelsey, Cathy S Cutler, Kim A Selting, Jeffrey N Bryan, Carolyn J Henry, Evan Boote, Deborah J Tate, et al. Gum arabic-coated radioactive gold nanoparticles cause no short-term local or systemic toxicity in the clinically relevant canine model of prostate cancer. *International journal of nanomedicine*, 9:5001, 2014.
- [28] Raghuraman Kannan, Ajit Zambre, Nripen Chanda, Rajesh Kulkarni, Ravi Shukla, Kavita Katti, Anandhi Upendran, Cathy Cutler, Evan Boote, and Kattesh V Katti. Functionalized radioactive gold nanoparticles in tumor therapy. *Wiley Interdisciplinary Reviews: Nanomedicine and Nanobiotechnology*, 4(1):42–51, 2012.
- [29] Chanda et al. Radioactive gold nanoparticles in cancer therapy: therapeutic efficacy studies of ga-198aunp nanoconstruct in prostate tumor-bearing mice. *Nanomedicine: Nanotechnology, Biology and Medicine*, 6(2):201–209, 2010.
- [30] Ravi Shukla, Satish K Nune, Nripen Chanda, Kavita Katti, Swapna Mekapothula, Rajesh R Kulkarni, Wade V Welshons, Raghuraman Kannan, and Kattesh V Katti. Soybeans as a phytochemical reservoir for the production and stabilization of biocompatible gold nanoparticles. *Small*, 4(9):1425–1436, 2008.
- [31] L-Pelletier et al. Low-dose prostate cancer brachytherapy with radioactive palladium-gold nanoparticles. *Advanced Healthcare Materials*, 6(4):1601120, 2017.
- [32] Laprise-Pelletier et al. Gold nanoparticles in radiotherapy and recent progress in nanobrachytherapy. *Advanced healthcare materials*, 7(16):1701460, 2018.
- [33] Laprise-Pelletier et al. Intratumoral injection of low-energy photon-emitting gold nanoparticles: A microdosimetric monte carlo-based model. *ACS nano*, 12(3):2482–2497, 2018.
- [34] J Allison, Katsuya Amako, John Apostolakis, Pedro Arce, M Asai, T Aso, E Bagli, A Bagulya, S Banerjee, GJNI Barrand, et al. Recent developments in geant4. *Nuclear Instruments and Methods in Physics Research Section A: Accelerators, Spectrometers, Detectors and Associated Equipment*, 835:186–225, 2016.
- [35] John T Goorley, MR James, TE Booth, FB Brown, JS Bull, LJ Cox, JW Durkee, JS Elson, ML Fensin, RA Forster, et al. Mcnp6 user’s manual, version 1.0. *Los Alamos, NM: Los Alamos National Laboratory*, 2013.

- [36] J Baro, J Sempau, JM Fernández-Varea, and F Salvat. Penelope: an algorithm for monte carlo simulation of the penetration and energy loss of electrons and positrons in matter. *Nuclear Instruments and Methods in Physics Research Section B: Beam Interactions with Materials and Atoms*, 100(1):31–46, 1995.
- [37] Francesc Salvat, José M Fernández-Varea, Eduardo Acosta, and J PENELOPE Sempau. a code system for monte carlo simulation of electron and photon transport. In *Proceedings of a Workshop/Training Course, OECD/NEA*, pages 5–7, 2001.
- [38] Joseph Perl, Jungwook Shin, Jan Schümann, Bruce Faddegon, and Harald Paganetti. Topas: an innovative proton monte carlo platform for research and clinical applications. *Medical physics*, 39(11):6818–6837, 2012.
- [39] Iwan Kawrakow. The egsnrc code system, monte carlo simulation of electron and photon transport. *NRCC Report Pirs-701*, 2001.
- [40] S. Incerti, Ioanna Kyriakou, MA Bernal, MC Bordage, Z Francis, Susanna Guatelli, V Ivanchenko, M Karamitros, N Lampe, Sang Bae Lee, et al. Geant4-dna example applications for track structure simulations in liquid water: A report from the geant4-dna project. *Medical physics*, 45(8):e722–e739, 2018.
- [41] S. Incerti et al. The geant4-dna project. *International Journal of Modeling, Simulation, and Scientific Computing*, 1(02):157–178, 2010.
- [42] I Kyriakou, S Incerti, and Z Francis. Improvements in geant4 energy-loss model and the effect on low-energy electron transport in liquid water. *Medical physics*, 42(7):3870–3876, 2015.
- [43] MC Bordage, J Bordes, S Edel, M Terrissol, X Franceries, Manuel Bardiès, N Lampe, and Sebastien Incerti. Implementation of new physics models for low energy electrons in liquid water in geant4-dna. *Physica Medica*, 32(12):1833–1840, 2016.
- [44] S Incerti et al. Comparison of geant4 very low energy cross section models with experimental data in water. *Medical physics*, 37(9):4692–4708, 2010.
- [45] MA Bernal et al. Track structure modeling in liquid water: A review of the geant4-dna very low energy extension of the geant4 monte carlo simulation toolkit. *Physica Medica*, 31(8):861–874, 2015.
- [46] Baljeet Seniwal et al. Comparison of dosimetric accuracy of acuros xb and analytical anisotropic algorithm against monte carlo technique. *Biomedical Physics & Engineering Express*, 6(1):015035, 2020.
- [47] T.C.F. Fonseca et al. Mcmeg: Intercomparison exercise on prostate radiotherapy dose assessment. *Radiation Physics and Chemistry*, 167:108295, 2020.
- [48] T.C.F. Fonseca et al. Mcmeg: Simulations of both pdd and tpr for 6mv linac photon beam using different mc codes. *Radiation Physics and Chemistry*, 140:386 – 391, 2017.
- [49] DWO Rogers et al. Beam: a monte carlo code to simulate radiotherapy treatment units. *Medical physics*, 22(5):503–524, 1995.

- [50] Iwan Kawrakow. Accurate condensed history monte carlo simulation of electron transport. i. egsnrc, the new egs4 version. *Medical physics*, 27(3):485–498, 2000.
- [51] Amal Y Al-Yasiri, Nathan E White, Kattesh V Katti, and Sudarshan K Loyalka. Estimation of tumor and local tissue dose in gold nanoparticles radiotherapy for prostate cancer. *Reports of Practical Oncology & Radiotherapy*, 24(3):288–293, 2019.
- [52] Christophe Champion et al. Dose point kernels in liquid water: an intra-comparison between geant4-dna and a variety of monte carlo codes. *Applied radiation and isotopes*, 83:137–141, 2014.
- [53] F Botta, Mairani, et al. Calculation of electron and isotopes dose point kernels with fluka monte carlo code for dosimetry in nuclear medicine therapy. *Medical physics*, 38(7):3944–3954, 2011.
- [54] Faiz M Khan et al. Clinical electron-beam dosimetry: report of aapm radiation therapy committee task group no. 25. *Medical physics*, 18(1):73–109, 1991.
- [55] Šefl et al. Calculation of cellular s-values using geant4-dna: the effect of cell geometry. *Applied Radiation and Isotopes*, 104:113–123, 2015.
- [56] H Fourie et al. Microdosimetry of the auger electron emitting 123i radionuclide using geant4-dna simulations. *Physics in Medicine & Biology*, 60(8):3333, 2015.
- [57] Nadia Falzone et al. Monte carlo evaluation of auger electron–emitting theranostic radionuclides. *Journal of Nuclear Medicine*, 56(9):1441–1446, 2015.
- [58] Nadia Falzone et al. Absorbed dose evaluation of auger electron-emitting radionuclides: impact of input decay spectra on dose point kernels and s-values. *Physics in Medicine & Biology*, 62(6):2239, 2017.
- [59] Al-Yasiri et al. Mangiferin functionalized radioactive gold nanoparticles (mgf-198 aumps) in prostate tumor therapy: green nanotechnology for production, in vivo tumor retention and evaluation of therapeutic efficacy. *Dalton Transactions*, 46(42):14561–14571, 2017.
- [60] Julie T-W Wang, Rebecca Klippstein, Markus Martincic, Elzbieta Pach, Robert Feldman, Martin Šefl, Yves Michel, Daniel Asker, Jane K Sosabowski, Martin Kalbac, et al. Neutron activated 153sm sealed in carbon nanocapsules for in vivo imaging and tumor radiotherapy. *ACS nano*, 14(1):129–141, 2019.
- [61] Frank Herbert Attix. *Introduction to radiological physics and radiation dosimetry*. John Wiley & Sons, 2008.
- [62] Yuting Lin et al. Biological modeling of gold nanoparticle enhanced radiotherapy for proton therapy. *Physics in Medicine & Biology*, 60(10):4149, 2015.
- [63] Wonmo Sung et al. Dependence of gold nanoparticle radiosensitization on cell geometry. *Nanoscale*, 9(18):5843–5853, 2017.

- [64] Caroline Stokke et al. Dosimetry-based treatment planning for molecular radiotherapy: a summary of the 2017 report from the internal dosimetry task force. *EJNMMI physics*, 4(1):27, 2017.
- [65] Bethesda et al. Icru, stopping powers for electrons and positrons- report 37. *International Commission on Radiation Units and Measurements*, Report 37, 1984.
- [66] Susan D Kost et al. Vida: a voxel-based dosimetry method for targeted radionuclide therapy using geant4. *Cancer Biotherapy and Radiopharmaceuticals*, 30(1):16–26, 2015.
- [67] JM Fernández-Varea et al. Cross sections for electron interactions in condensed matter. *Surface and Interface Analysis: An International Journal devoted to the development and application of techniques for the analysis of surfaces, interfaces and thin films*, 37(11):824–832, 2005.
- [68] Jintana Meesungnoen et al. Low-energy electron penetration range in liquid water. *Radiation research*, 158(5):657–660, 2002.
- [69] Baljeet Seniwal, Mario A Bernal, and Telma CF Fonseca. Microdosimetric calculations for radionuclides emitting β and α particles and auger electrons. *Applied Radiation and Isotopes*, page 109302, 2020.
- [70] Maher O El-Ghossain. Calculations of stopping power, and range of electrons interaction with different material and human body parts. *Calculations Of Stopping Power, And Range Of Electrons Interaction With Different Material And Human Body Parts*, 6(ISSUE 01), 2017.
- [71] Leonhard Karsch et al. Towards ion beam therapy based on laser plasma accelerators. *Acta Oncologica*, 56(11):1359–1366, 2017.
- [72] Colette J Shen et al. Auger radiopharmaceutical therapy targeting prostate-specific membrane antigen in a micrometastatic model of prostate cancer. *Theranostics*, 10(7):2888, 2020.
- [73] Dimitris Emfietzoglou et al. Inelastic cross sections for low-energy electrons in liquid water: exchange and correlation effects. *Radiation research*, 180(5):499–513, 2013.
- [74] NIST. Estar: Stopping powers and ranges for electrons. national institute of standards and technology, 2020. <https://physics.nist.gov/PhysRefData/Star/Text/ESTAR.html>.
- [75] MATLAB 9.7.0.1190202 (R2019b). Natick, massachusetts: The mathworks inc., 2018. <http://www.mathworks.com>.
- [76] Johan Blakkisrud. Tumor dosimetry in a phase i study of lu (177)-dota-hh1 (betalutin)-how hard does the magic bullet strike? Master’s thesis, NTNU, 2015.
- [77] Helena Uusijärvi et al. Comparison of electron dose-point kernels in water generated by the monte carlo codes, penelope, geant4, mcnp, and etran. *Cancer biotherapy and radiopharmaceuticals*, 24(4):461–467, 2009.

- [78] Francesc Salvat et al. Penelope-2006: A code system for monte carlo simulation of electron and photon transport. In *Workshop proceedings*, volume 4, page 7. Nuclear Energy Agency, Organization for Economic Co-operation and . . . , 2006.
- [79] Stephen M Seltzer. Electron-photon monte carlo calculations: the etran code. *International Journal of Radiation Applications and Instrumentation. Part A. Applied Radiation and Isotopes*, 42(10):917–941, 1991.
- [80] Sea Agostinelli et al. Geant4—a simulation toolkit. *Nuclear instruments and methods in physics research section A: Accelerators, Spectrometers, Detectors and Associated Equipment*, 506(3):250–303, 2003.
- [81] Laurie S Waters et al. Mcnpx user’s manual. *Los Alamos National Laboratory*, 2002.
- [82] Wesley E Bolch et al. Mird pamphlet no. 17: the dosimetry of nonuniform activity distributions—radionuclide s values at the voxel level. *Journal of Nuclear Medicine*, 40(1):11S–36S, 1999.
- [83] M Terrissol and A Beaudre. Simulation of space and time evolution of radiolytic species induced by electrons in water. *Radiation Protection Dosimetry*, 31(1-4):175–177, 1990.
- [84] A. Ferrari et al. *FLUKA: a multi-particle transport code*. CERN, 2005.
- [85] G. Battistoni et al. The fluka code: Description and benchmarking. *AIP. Conf. Proc.*, 896:31–49, 2006.
- [86] Dale L Bailey and JL Humm. *Nuclear medicine physics: a handbook for teachers and students*. Iaea, 2014.
- [87] Gopal B. Saha. *Physics and Radiobiology of Nuclear Medicine*. Springer-Verlag, New York, 4 edition, 2013.
- [88] Hum B Giap, Daniel J Macey, John E Bayouth, and Arthur L Boyer. Validation of a dose-point kernel convolution technique for internal dosimetry. *Physics in Medicine & Biology*, 40(3):365, 1995.
- [89] J Vedelago, D Chacón Obando, F Malano, R Conejeros, R Figueroa, D Garcia, G González, M Romero, M Santibañez, Miriam Cristina Strumia, et al. Fricke and polymer gel 2d dosimetry validation using monte carlo simulation. *Radiation Measurements*, 91:54–64, 2016.
- [90] R Loevinger and M Berman. A revised schema for calculating the absorbed dose from biologically distributed radionuclides (new york: Society of nuclear medicine) medical internal radiation dose committee pamphlet 1, 1976.
- [91] Francesc Salvat et al. Penelope-2001: A code system for monte carlo simulation of electron and photon transport. In *Workshop Proceedings*, volume 4, page 7, 2001.
- [92] Denise B Pelowitz et al. Mcnp6™ user’s manual version 1.0 (la-cp-13-00634, rev. 0). *Los Alamos National Laboratory, Los Alamos*, 2013.

- [93] Daniel A Low, William B Harms, Sasa Mutic, and James A Purdy. A technique for the quantitative evaluation of dose distributions. *Medical physics*, 25(5):656–661, 1998.
- [94] J Vedelago, D Chacón Obando, F Malano, R Conejeros, R Figueroa, D Garcia, G González, M Romero, M Santibañez, Miriam Cristina Strumia, et al. Fricke and polymer gel 2d dosimetry validation using monte carlo simulation. *Radiation Measurements*, 91:54–64, 2016.
- [95] M. A. General et al. Volume i: Overview and theory x-5 monte carlo team. *Los Alamos National Laboratory, Los Alamos*, 2008.
- [96] Rodolphe Antoni and Laurent Bourgois. Evaluation of the new electron-transport algorithm in mcnp6. 1 for the simulation of dose point kernel in water. *Nuclear Instruments and Methods in Physics Research Section B: Beam Interactions with Materials and Atoms*, 412:102–108, 2017.
- [97] A. Ferrari et al. An improved multiple scattering model for charged particle transport. *Nucl. Instrum. Meth. B*, 71:412–426, 1992.
- [98] G. Molière. Theorie der streuung schneller geladener teilchen ii - mehrfach und vielfachstreuung. *Z. Naturforsch.*, 3a:78–97, 1948.
- [99] G. Molière. Theorie der streuung schneller geladener teilchen iiic - die vielfachstreuung von bahnsuren unter beruecksichtigung der statis- tischen kopplung. *Z. Naturforsch.*, 10a:177–211, 1955.
- [100] D. Cullen et al. *EPDL97: The Evaluated Photon Data Library. UCRL-LR-50400*, volume 10a. Wiley Online Library, 1955.
- [101] G. Santa Cruz. Microdosimetry: Principles and applications. *Reports of Practical Oncology and Radiotherapy*, 21(2):135–139, 2016.
- [102] Taku Inaniwa, Takuji Furukawa, Yuki Kase, Naruhiro Matsufuji, Toshiyuki Toshito, Yoshitaka Matsumoto, Yoshiya Furusawa, and Koji Noda. Treatment planning for a scanned carbon beam with a modified microdosimetric kinetic model. *Physics in Medicine & Biology*, 55(22):6721, 2010.
- [103] Piotr Zygmanski, Bo Liu, Panagiotis Tsiamas, Fulya Cifter, Markus Petersheim, Jürgen Hesser, and Erno Sajo. Dependence of monte carlo microdosimetric computations on the simulation geometry of gold nanoparticles. *Physics in Medicine & Biology*, 58(22):7961, 2013.
- [104] Facundo Mattea, José Vedelago, Francisco Malano, Cesar Gomez, Miriam C Strumia, and Mauro Valente. Silver nanoparticles in x-ray biomedical applications. *Radiation Physics and Chemistry*, 130:442–450, 2017.
- [105] W. Li et al. Intercomparison of dose enhancement ratio and secondary electron spectra for gold nanoparticles irradiated by x-rays calculated using multiple monte carlo simulation codes. *European Journal of Medical Physics*, 69(22):147–163, 2020.

- [106] Sergey V Gudkov, Natalya Yu Shilyagina, Vladimir A Vodeneev, and Andrei V Zvyagin. Targeted radionuclide therapy of human tumors. *International journal of molecular sciences*, 17(1):33, 2016.
- [107] Abdollah Khorshidi, Marjan Ahmadinejad, and S Hamed Hosseini. Evaluation of a proposed biodegradable ¹⁸⁸Re source for brachytherapy application: a review of dosimetric parameters. *Medicine*, 94(28), 2015.
- [108] Tarcisio Passos Ribeiro de Campos, Luciana Batista Nogueira, Bruno Trindade, and Ethel Mizrahy Cuperschmid. Dosimetric intercomparison of permanent ¹⁰⁶Rh seed's implants and ¹⁹²Ir brachytherapy in breast cancer. *Reports of Practical Oncology & Radiotherapy*, 21(3):240–249, 2016.
- [109] Marcelo Tatit Sapienza and José Willegaignon. Radionuclide therapy: current status and prospects for internal dosimetry in individualized therapeutic planning. *Clinics*, 74, 2019.
- [110] Janelle M Wheat, Geoffrey M Currie, Robert Davidson, and Hosen Kiat. Radionuclide therapy. *Radiographer*, 58(3):53–59, 2011.
- [111] Jongho Jeon. Review of therapeutic applications of radiolabeled functional nanomaterials. *International journal of molecular sciences*, 20(9):2323, 2019.
- [112] Tiantian Li, Edwin CI Ao, Bieke Lambert, Boudewijn Brans, Stefaan Vandenberghe, and Greta SP Mok. Quantitative imaging for targeted radionuclide therapy dosimetry-technical review. *Theranostics*, 7(18):4551, 2017.
- [113] Julie Tzu-Wen Wang, Cinzia Spinato, Rebecca Klippstein, Pedro Miguel Costa, Markus Martincic, Elzbieta Pach, Aritz Perez Ruiz de Garibay, Cécilia Ménard-Moyon, Robert Feldman, Yves Michel, et al. Neutron-irradiated antibody-functionalised carbon nanocapsules for targeted cancer radiotherapy. *Carbon*, 2020.
- [114] C Bousis, D Emfietzoglou, P Hadjidoukas, and H Nikjoo. Monte carlo single-cell dosimetry of auger-electron emitting radionuclides. *Physics in Medicine & Biology*, 55(9):2555, 2010.
- [115] Cecilia Hindorf, Dimitris Emfietzoglou, Ola Lindén, Christos Bousis, Andreas Fotopoulos, Kostas Kostarelos, and Glenn D Flux. Single-cell dosimetry for radioimmunotherapy of b-cell lymphoma patients with special reference to leukemic spread. *Cancer biotherapy & radiopharmaceuticals*, 22(3):357–366, 2007.
- [116] Cecilia Hindorf, Dimitris Emfietzoglou, Ola Lindén, Kostas Kostarelos, and Sven-Erik Strand. Internal microdosimetry for single cells in radioimmunotherapy of b-cell lymphoma. *Cancer biotherapy & radiopharmaceuticals*, 20(2):224–230, 2005.
- [117] AM Syme, C Kirkby, TA Riauka, BG Fallone, and SA McQuarrie. Monte carlo investigation of single cell beta dosimetry for intraperitoneal radionuclide therapy. *Physics in Medicine & Biology*, 49(10):1959, 2004.
- [118] Wanderley dos Santos Roberto, Marivalda Magalhães Pereira, and Tarcísio Passos Ribeiro de Campos. Analysis of bioactive glasses obtained by sol-gel processing for radioactive implants. *Materials research*, 6(2):123–127, 2003.

- [119] Wanderley S Roberto, Marivalda M Pereira, and Tarcísio PR Campos. Structure and dosimetric analysis of biodegradable glasses for prostate cancer treatment. *Artificial organs*, 27(5):432–436, 2003.
- [120] Marzieh Anjomrouz, Mo K Bakht, and Mahdi Sadeghi. Feasibility study of fluka monte carlo simulation for a beta-emitting brachytherapy source: dosimetric parameters of 142 pr glass seed. *Journal of Radioanalytical and Nuclear Chemistry*, 309(3):947–953, 2016.
- [121] R Calandrino, A Del Vecchio, S Todde, and F Fazio. Measurement and control of the air contamination generated in a medical cyclotron facility for pet radiopharmaceuticals. *Health physics*, 92(5):S70–S77, 2007.
- [122] Asghar Hadadi, Mahdi Sadeghi, Dariush Sardari, Alireza Khanchi, and Alireza Shirazi. Monte carlo characterization of biocompatible beta-emitting glass seed incorporated with the radionuclide as a spect marker for brachytherapy applications. *Journal of applied clinical medical physics*, 14(5):90–103, 2013.
- [123] Jae Won Jung and Warren Daniel Reece. Dosimetric characterization of 142pr glass seeds for brachytherapy. *Applied Radiation and Isotopes*, 66(4):441–449, 2008.
- [124] Tatsuhiko Sato, Koji Niita, Norihiro Matsuda, Shintaro Hashimoto, Yosuke Iwamoto, Takuya Furuta, Shusaku Noda, Tatsuhiko Ogawa, Hiroshi Iwase, Hiroshi Nakashima, et al. Overview of particle and heavy ion transport code system phits. In *SNA+ MC 2013-Joint International Conference on Supercomputing in Nuclear Applications+ Monte Carlo*, page 06018. EDP Sciences, 2014.
- [125] B Pelowitz Denise. Mcnpx user’s manual, version 2.7. 0. Technical report, April LA-CP-11-00438, 2011.
- [126] Nick Reynaert, Hugo Palmans, Hubert Thierens, and R Jeraj. Parameter dependence of the mcnp electron transport in determining dose distributions. *Medical physics*, 29(10):2446–2454, 2002.
- [127] C Bousis, D Emfietzoglou, P Hadjidoukas, and H Nikjoo. A monte carlo study of absorbed dose distributions in both the vapor and liquid phases of water by intermediate energy electrons based on different condensed-history transport schemes. *Physics in Medicine & Biology*, 53(14):3739, 2008.
- [128] Ioanna Kyriakou, V Ivanchenko, Dosatsu Sakata, MC Bordage, Susanna Guatelli, Sebastien Incerti, and Dimitris Emfietzoglou. Influence of track structure and condensed history physics models of geant4 to nanoscale electron transport in liquid water. *Physica Medica*, 58:149–154, 2019.
- [129] L Maigne, Y Perrot, DR Schaart, D Donnarieix, and Vincent Breton. Comparison of gate/geant4 with egsnrc and mcnp for electron dose calculations at energies between 15 kev and 20 mev. *Physics in Medicine & Biology*, 56(3):811, 2011.
- [130] M Stabin, J Siegel, J Hunt, R Sparks, J Lipsztein, and K Eckerman. Radar: the radiation dose assessment resource—an online source of dose information for nuclear medicine and occupational radiation safety. *J Nucl Med*, 42(5):243P, 2001.

- [131] H Grady Hughes III. Recent developments in low-energy electron/photon transport for mcnp6. Technical report, Los Alamos National Lab.(LANL), Los Alamos, NM (United States), 2012.
- [132] Josep Sempau, Andreu Badal, and Lorenzo Brualla. A penelope-based system for the automated monte carlo simulation of clinacs and voxelized geometries—application to far-from-axis fields. *Medical physics*, 38(11):5887–5895, 2011.
- [133] Baljeet Seniwala et al. Monte-carlo modelling for evaluation of two different calculation algorithms. *Brazilian Journal of Radiation Sciences*, 7(1), 2019.
- [134] Andrius Poškus. Evaluation of computational models and cross sections used by mcnp6 for simulation of electron backscattering. *Nuclear Instruments and Methods in Physics Research Section B: Beam Interactions with Materials and Atoms*, 368:15–27, 2016.
- [135] J Wu, YL Liu, SJ Chang, MM Chao, SY Tsai, and DE Huang. Dose point kernel simulation for monoenergetic electrons and radionuclides using monte carlo techniques. *Radiation protection dosimetry*, 152(1-3):119–124, 2012.
- [136] I Kyriakou, M Šefl, V Nourry, and S Incerti. The impact of new geant4-dna cross section models on electron track structure simulations in liquid water. *Journal of Applied Physics*, 119(19):194902, 2016.
- [137] Sung-Hyun Kim. Is radioimmunotherapy a ‘magic bullet’? *The Korean journal of hematology*, 47(2):85, 2012.
- [138] JA O’donoghue and TE Wheldon. Targeted radiotherapy using auger electron emitters. *Physics in Medicine & Biology*, 41(10):1973, 1996.
- [139] Michael R McDevitt et al. Radioimmunotherapy with alpha-emitting nuclides. *European journal of nuclear medicine*, 25(9):1341–1351, 1998.
- [140] WA Volkert et al. Therapeutic radionuclides: production and decay property considerations. *Journal of nuclear medicine: official publication, Society of Nuclear Medicine*, 32(1):174–185, 1991.
- [141] AI Kassis, SJ Adelstein, C Haydock, KSR Sastry, KD McElvany, and MJ Welch. Lethality of auger electrons from the decay of bromine-77 in the dna of mammalian cells. *Radiation research*, 90(2):362–373, 1982.
- [142] Kandula SR Sastry. Biological effects of the auger emitter iodine-125: A review. report no. 1 of aapm nuclear medicine task group no. 6. *Medical physics*, 19(6):1361–1370, 1992.
- [143] Jean-Francois Chatal and Cornelis A Hoefnagel. Radionuclide therapy. *The Lancet*, 354(9182):931 – 935, 1999.
- [144] GM Makrigiorgos et al. Dna damage produced in v79 cells by dna-incorporated iodine-123: A comparison with iodine-125. *Radiation research*, 129(3):309–314, 1992.

- [145] G Mike Makrigiorgos et al. Inhomogeneous deposition of radiopharmaceuticals at the cellular level: experimental evidence and dosimetric implications. *Journal of Nuclear Medicine*, 31(8):1358–1363, 1990.
- [146] Jörgen Carlsson et al. Therapy with radiopharmaceuticals. *Acta oncologica*, 41(7-8):623–628, 2002.
- [147] S Murty Goddu et al. Mird cellular s values. Reston, VA: Society of Nuclear Medicine, 1997.
- [148] Rajendrakumar Santhosh Kalash et al. Theranostics. In *Biomaterials Nanoarchitectonics*, pages 197–215. Elsevier, 2016.
- [149] K Eckerman et al. Icrp publication 107. nuclear decay data for dosimetric calculations. *Annals of the ICRP*, 38(3):7–96, 2008.
- [150] Boon Q Lee et al. Atomic radiations in the decay of medical radioisotopes: A physics perspective. *Computational and mathematical methods in medicine*, 2012, 2012.
- [151] Roger W Howell. Radiation spectra for auger-electron emitting radionuclides: Report no. 2 of aapm nuclear medicine task group no. 6. *Medical physics*, 19(6):1371–1383, 1992.
- [152] Thierry André et al. Comparison of geant4-dna simulation of s-values with other monte carlo codes. *Nuclear Instruments and Methods in Physics Research Section B: Beam Interactions with Materials and Atoms*, 319:87–94, 2014.
- [153] WS Snyder. "s-absorbed dose per unit cumulated activity for selected radionuclides and organs". *MIRD Pamphlet no. 11*, 1975.
- [154] Wesley E Bolch et al. Mird pamphlet no. 21: a generalized schema for radiopharmaceutical dosimetry—standardization of nomenclature. *Journal of Nuclear Medicine*, 50(3):477–484, 2009.
- [155] Behrooz Vaziri et al. Mird pamphlet no. 25: Mirdcell v2. 0 software tool for dosimetric analysis of biologic response of multicellular populations. *Journal of Nuclear Medicine*, 55(9):1557–1564, 2014.
- [156] S Murty Goddu et al. Cellular dosimetry: absorbed fractions for monoenergetic electron and alpha particle sources and s-values for radionuclides uniformly distributed in different cell compartments. *Journal of nuclear medicine: official publication, Society of Nuclear Medicine*, 35(2):303–316, 1994.
- [157] ICRP. *Radionuclide transformations: energy and intensity of emissions*, volume 11. Pergamon, 1983.
- [158] Guosheng Song, Liang Cheng, Yu Chao, Kai Yang, and Zhuang Liu. Emerging nanotechnology and advanced materials for cancer radiation therapy. *Advanced materials*, 29(32):1700996, 2017.
- [159] Aranda-Lara et al. Radiolabeled liposomes and lipoproteins as lipidic nanoparticles for imaging and therapy. *Chemistry and Physics of Lipids*, page 104934, 2020.

- [160] Schuemann et al. Roadmap for metal nanoparticles in radiation therapy: current status, translational challenges, and future directions. *Physics in Medicine & Biology*, 2020.
- [161] Li et al. Intercomparison of dose enhancement ratio and secondary electron spectra for gold nanoparticles irradiated by x-rays calculated using multiple monte carlo simulation codes. *Physica Medica*, 69:147–163, 2020.
- [162] Ngwa et al. Gold nanoparticle-aided brachytherapy with vascular dose painting: Estimation of dose enhancement to the tumor endothelial cell nucleus. *Medical physics*, 39(1):392–398, 2012.
- [163] Ngwa et al. In vitro radiosensitization by gold nanoparticles during continuous low-dose-rate gamma irradiation with i-125 brachytherapy seeds. *Nanomedicine: Nanotechnology, Biology and Medicine*, 9(1):25–27, 2013.
- [164] Sinha et al. Brachytherapy application with in situ dose painting administered by gold nanoparticle eluters. *International Journal of Radiation Oncology* Biology* Physics*, 91(2):385–392, 2015.
- [165] Martinov et al. Heterogeneous multiscale monte carlo simulations for gold nanoparticle radiosensitization. *Medical physics*, 44(2):644–653, 2017.
- [166] Meyer et al. Peer-based credentialing for brachytherapy: Application in permanent seed implant. *Brachytherapy*, 2020.
- [167] Su et al. Radionuclide-labeled gold nanoparticles for nuclei-targeting internal radio-immunity therapy. *Materials Horizons*, 7(4):1115–1125, 2020.
- [168] Yaser H Gholami et al. A chelate-free nano-platform for incorporation of diagnostic and therapeutic isotopes. *International Journal of Nanomedicine*, 15:31, 2020.
- [169] Shukla et al. Laminin receptor specific therapeutic gold nanoparticles (198aunp-egcg) show efficacy in treating prostate cancer. *Proceedings of the National Academy of Sciences*, 109(31):12426–12431, 2012.
- [170] Moeendarbari et al. Theranostic nanoseeds for efficacious internal radiation therapy of unresectable solid tumors. *Scientific reports*, 6(1):1–9, 2016.
- [171] Stephen Joseph McMahon. The linear quadratic model: usage, interpretation and challenges. *Physics in Medicine & Biology*, 64(1):01TR01, 2018.
- [172] DE Lea and DG Catcheside. The mechanism of the induction by radiation of chromosome aberrations intradescantia. *Journal of genetics*, 44(2-3):216–245, 1942.
- [173] David J Brenner. The linear-quadratic model is an appropriate methodology for determining isoeffective doses at large doses per fraction. In *Seminars in radiation oncology*, volume 18, pages 234–239. Elsevier, 2008.
- [174] Roger G Dale. The application of the linear-quadratic dose-effect equation to fractionated and protracted radiotherapy. *The British journal of radiology*, 58(690):515–528, 1985.

- [175] TE Wheldon and JA O'donoghue. The radiobiology of targeted radiotherapy. *International journal of radiation biology*, 58(1):1–21, 1990.
- [176] TE Wheldon et al. The curability of tumours of differing size by targeted radiotherapy using ^{131}I or ^{90}Y . *Radiotherapy and Oncology*, 21(2):91–99, 1991.
- [177] O'Donoghue. The impact of tumor cell proliferation in radioimmunotherapy. *Cancer*, 73(S3):974–980, 1994.
- [178] Roger Dale and Alejandro Carabe-Fernandez. The radiobiology of conventional radiotherapy and its application to radionuclide therapy. *Cancer biotherapy & radiopharmaceuticals*, 20(1):47–51, 2005.
- [179] TCF Fonseca, PCG Antunes, MCL Belo, F Bastos, TP Campos, JM Geraldo, AM Mendes, BM Mendes, L Paixão, PC Santana, et al. Mcmeg: Intercomparison exercise on prostate radiotherapy dose assessment. *Radiation Physics and Chemistry*, 167:108295, 2020.
- [180] Šefl et al. Impact of cell repopulation and radionuclide uptake phase on cell survival. *Medical Physics*, 43(6Part1):2715–2720, 2016.
- [181] Baljeet Seniwai et al. Microdosimetric calculations for radionuclides emitting β and α particles and auger electrons. *Applied Radiation and Isotopes*, page 109302, 2020.
- [182] Martin. Nuclear data sheets for $a=152$. *Nuclear Data Sheets*, 114(11):1497–1847, 2013.
- [183] Evaluated Nuclear Structure Data File ENSDF. Maintained by the national nuclear data center at brookhaven national lab. *Online document at www.nndc.bnl.gov/ensdf* Accessed on March, 17, 2018.
- [184] Dale et al. *Radiobiological modelling in radiation oncology*. British Inst of Radiology, 2007.
- [185] Elgqvist et al. Radiosensitivity of prostate cancer cell lines for irradiation from beta particle-emitting radionuclide ^{177}Lu compared to alpha particles and gamma rays. *Anticancer research*, 36(1):103–109, 2016.
- [186] Van Leeuwen et al. The alfa and beta of tumours: a review of parameters of the linear-quadratic model, derived from clinical radiotherapy studies. *Radiation oncology*, 13(1):1–11, 2018.
- [187] NNDC. National nuclear data center, 2020.
- [188] Cho et al. Determination of the tissue attenuation factor along two major axes of a high dose rate (hdr) source. *Medical physics*, 26(8):1492–1497, 1999.
- [189] Rivard et al. Supplement 2 for the 2004 update of the aapm task group no. 43 report: joint recommendations by the aapm and gec-estro. *Medical physics*, 44(9):e297–e338, 2017.

- [190] E Lechtman et al. Implications on clinical scenario of gold nanoparticle radiosensitization in regards to photon energy, nanoparticle size, concentration and location. *Physics in Medicine & Biology*, 56(15):4631, 2011.
- [191] MJ Jackson et al. International inter-comparison exercise on sm-153. *Journal of Radioanalytical and Nuclear Chemistry*, 318(1):107–115, 2018.
- [192] DS Moreira et al. Determination of 198au x-rays emission probabilities. *Applied Radiation and Isotopes*, 68(7-8):1566–1570, 2010.
- [193] Christiane Ferradini and Jean-Paul Jay-Gerin. La radiolyse de l'eau et des solutions aqueuses: historique et actualité. *Canadian Journal of Chemistry*, 77(9):1542–1575, 1999.
- [194] Nathanael Lampe et al. Mechanistic dna damage simulations in geant4-dna part 2: Electron and proton damage in a bacterial cell. *Physica Medica*, 48:146–155, 2018.
- [195] Dousatsu Sakata et al. Evaluation of early radiation dna damage in a fractal cell nucleus model using geant4-dna. *Physica Medica*, 62:152–157, 2019.
- [196] Dousatsu Sakata et al. Fully integrated monte carlo simulation for evaluating radiation induced dna damage and subsequent repair using geant4-dna. *Scientific reports*, 10(1):1–13, 2020.
- [197] Zhu et al. Cellular response to proton irradiation: A simulation study with topas-nbio. *Radiation Research*, pages 000–000, 2020.
- [198] Ianik Plante et al. Monte carlo simulation of the radiolysis of the ceric sulfate dosimeter by low linear energy transfer radiation. *Canadian Journal of Chemistry*, 90(9):717–723, 2012.
- [199] Leila Mirsaleh Kohan et al. Effect of temperature on the low-linear energy transfer radiolysis of the ceric-cerous sulfate dosimeter: a monte carlo simulation study. *Radiation research*, 181(5):495–502, 2014.
- [200] Narongchai Autsavapromporn et al. Monte carlo simulation study of the effects of acidity and let on the primary free-radical and molecular yields of water radiolysis—application to the fricke dosimeter. *Canadian journal of chemistry*, 85(3):214–229, 2007.
- [201] Akihiro Hiroki et al. Hydrogen peroxide production in the radiolysis of water with high radical scavenger concentrations. *The Journal of Physical Chemistry A*, 106(40):9352–9358, 2002.
- [202] A Colliaux et al. O₂ and glutathione effects on water radiolysis: a simulation study. *Journal of Physics: Conference Series*, 261:012007, jan 2011.
- [203] Louis Harold Gray et al. The concentration of oxygen dissolved in tissues at the time of irradiation as a factor in radiotherapy. *The British journal of radiology*, 26(312):638–648, 1953.

- [204] J Aikens and TA Dix. Perohydroxyl radical (hoo.) initiated lipid peroxidation. the role of fatty acid hydroperoxides. *Journal of Biological Chemistry*, 266(23):15091–15098, 1991.
- [205] Sara Goldstein and Gidon Czapski. The reaction of no· with o₂⁻ and ho₂⁻: A pulse radiolysis study. *Free Radical Biology and Medicine*, 19(4):505–510, 1995.
- [206] Aubrey DNJ de Grey. HO₂: The forgotten radical. *DNA and cell biology*, 21(4):251–257, 2002.
- [207] Ross B Mikkelsen and Peter Wardman. Biological chemistry of reactive oxygen and nitrogen and radiation-induced signal transduction mechanisms. *Oncogene*, 22(37):5734–5754, 2003.
- [208] DELATTRE Jacques et al. *Radicaux libres et stress oxydant: Aspects biologiques et pathologiques (broché)*. Lavoisier, 2007.
- [209] NJB Green et al. Stochastic modeling of fast kinetics in a radiation track. *Journal of Physical Chemistry*, 94(1):251–258, 1990.
- [210] Simon M Pimblott et al. Stochastic models of spur kinetics in water. *International Journal of Radiation Applications and Instrumentation. Part C. Radiation Physics and Chemistry*, 37(3):377–388, 1991.
- [211] Simon M Pimblott and Jay A LaVerne. Stochastic simulation of the electron radiolysis of water and aqueous solutions. *The Journal of Physical Chemistry A*, 101(33):5828–5838, 1997.
- [212] Ianik Plante and Luc Devroye. Considerations for the independent reaction times and step-by-step methods for radiation chemistry simulations. *Radiation Physics and Chemistry*, 139:157–172, 2017.
- [213] F Ballarini et al. Stochastic aspects and uncertainties in the prechemical and chemical stages of electron tracks in liquid water: a quantitative analysis based on monte carlo simulations. *Radiation and Environmental Biophysics*, 39(3):179–188, 2000.
- [214] Maximilian S Kreipl et al. Time-and space-resolved monte carlo study of water radiolysis for photon, electron and ion irradiation. *Radiation and environmental biophysics*, 48(1):11, 2009.
- [215] Ianik Plante and Francis A Cucinotta. Monte-carlo simulation of ionizing radiation tracks. *Application of Monte Carlo methods in biology, medicine and other fields of science. InTech, Rijeka, Croatia*, pages 315–356, 2011.
- [216] Sebastien Incerti et al. Review of geant4-dna applications for micro and nanoscale simulations. *Physica Medica*, 32(10):1187–1200, 2016.
- [217] D. Boscolo et al. Trax-chem: A pre-chemical and chemical stage extension of the particle track structure code trax in water targets. *Chemical Physics Letters*, 698:11 – 18, 2018.

- [218] Bruce Faddegon et al. The topas tool for particle simulation, a monte carlo simulation tool for physics, biology and clinical research. *Physica Medica*, 72:114–121, 2020.
- [219] J. Allison et al. Recent developments in geant4. *Nuclear Instruments and Methods in Physics Research Section A: Accelerators, Spectrometers, Detectors and Associated Equipment*, 835:186 – 225, 2016.
- [220] J Schuemann et al. Topas-nbio: an extension to the topas simulation toolkit for cellular and sub-cellular radiobiology. *Radiation research*, 191(2):125–138, 2019.
- [221] J Ramos-Méndez et al. Monte carlo simulation of chemistry following radiolysis with topas-nbio. *Physics in Medicine & Biology*, 63(10):105014, 2018.
- [222] Aimee McNamara et al. Validation of the radiobiology toolkit topas-nbio in simple dna geometries. *Physica Medica*, 33:207–215, 2017.
- [223] Aimee L McNamara et al. Geometrical structures for radiation biology research as implemented in the topas-nbio toolkit. *Physics in Medicine & Biology*, 63(17):175018, 2018.
- [224] José Ramos-Méndez et al. Flagged uniform particle splitting for variance reduction in proton and carbon ion track-structure simulations. *Physics in Medicine & Biology*, 62(15):5908, 2017.
- [225] J Shin et al. A modular method to handle multiple time-dependent quantities in monte carlo simulations. *Physics in Medicine & Biology*, 57(11):3295, 2012.
- [226] Xin Dong et al. Creating and improving multi-threaded geant4. In *J. Phys.: Conf. Ser.*, volume 396, page 052029, 2012.
- [227] Milton Burton. Radiation chemistry. *Annual Review of Physical Chemistry*, 1(1):113–132, 1950.
- [228] Ioannis Sechopoulos, David WO Rogers, Magdalena Bazalova-Carter, Wesley E Bolch, Emily C Heath, Michael F McNitt-Gray, Josep Sempau, and Jeffrey F Williamson. Records: improved reporting of monte carlo radiation transport studies: report of the aapm research committee task group 268. *Medical physics*, 45(1):e1–e5, 2018.

Appendix A

Other Publications, Book Chapter and Events

A.1 Publications

1. **Seniwal B**, Fonseca TC, Singh R. Monte-carlo modelling for evaluation of two different calculation algorithms. Brazilian Journal of Radiation Sciences. 2019 Jan 28;7(1).
Modeling of linac head (VARIAN Trilogy) for 6 MeV photon beam was performed using BEAMnrc code package (BEAMnrc 2017). The DOSXYZnrc code was used to determine the percentage depth dose (PDD profiles) and beam profiles for different symmetric square field sizes, ie, 5cm X 5cm; and 40cm X 40cm. The DICOM images of Alderson Radiation Therapy (ART) RANDO Phantom was used. Four field 3D-CRT treatment plans were generated using AAA, PBC, and Monte-Carlo (MC). It was found that nominal energy of 5.7 MeV with FWHM of 1.2 mm provides best matching of modelled and working linac. All three 3D-CRT plans calculated with AAA, PBC and MC on a Pelvic Rando phantom, were compared using CERR (Computational Environment for Radiotherapy Research) and MATLAB 2013b. It was found that AAA and PBC have comparable results, although in case of tissue interfaces and inhomogeneous media AAA provides better accuracy in comparison to PBC. It can also be observed that AAA and PBC underestimate doses in comparison to MC in the soft muscle tissue which includes OARs such as bladder, bowel bag, and PTV TOTAL. It was found that both AAA and PBC fails to account for tissue air interface accurately and shows variation of 30-40% whereas for surface dose variation of +/-10% was observed. In homogeneous media (muscle tissue) AAA and PBC underestimate doses in comparison to MC. These commercially available algorithms

overestimates and underestimates dose values as compared to MC based dose calculation for low and high dose regions specially.

2. Donya H, **Seniwal B**, Darwesh R, Fonseca TC. Prospective Monte Carlo Simulation for Choosing High Efficient Detectors for Small-Field Dosimetry. In Theory, Application, and Implementation of Monte Carlo Method in Science and Technology 2019 Nov 11. IntechOpen.

In this chapter, a detailed study on physics and methodology of small field dosimetry are reported. It introduces talking about how small radiation fields came into existence and the importance of accurate small-field dosimetry. In addition, it discusses small and long cavity theories for evaluating accurate dose response. It sheds the spot on pencil beam algorithms for evaluating dose response and uses Monte Carlo (MC) simulation in categorizing primary and scattering components of the radiotherapeutic photon beam. Moreover, it summarizes all commercial dosimeters used in small-field dosimetry. It gives good knowledge about detectors and equipment like ionization chambers for reference dosimetry in small and nonreference fields and different types of solid-state detector. The importance and applications of Monte Carlo techniques in small-field dosimetry and radiotherapeutic treatment methods based on small field are reported. For this purpose, different commonly used Monte Carlo codes are handled like Electron Gamma Shower (EGSnrc), Geant4, PENELOPE, and Monte Carlo N-Particle (MCNP). A review on the recent studies of using Monte Carlo simulation particularly on the small-field dosimetric studies is also reported. This chapter also discusses the recommendations of the code of practices (COPs) for dosimetry of small radiation fields. It mentions all recommendations provided by TRS-483 for accurate beam data collection and accurate dosimetric measurements. It gives good knowledge to the user for selecting a suitable dosimeter in small-field dosimetry through investigation of different practical methods and Monte Carlo simulations.

3. Fonseca TC, Antunes PC, Belo MC, Bastos F, Campos TP, Geraldo JM, Mendes AM, Mendes BM, Paixão L, Santana PC, **Seniwal B**, PL Squair, H Yoriyaz MCMEG: Inter-comparison exercise on prostate radiotherapy dose assessment. Radiation Physics and Chemistry. 2020 Feb 1;167:108295.

The improvement of the Monte Carlo (MC) community skills on computational simulations in Medical Physics is crucial to the field of radiotherapy as well as radiology. The Monte Carlo Modelling Expert Group (MCMEG) is an expert network specialized in MC radiation transport modelling and simulation applied to the radiation protection and dosimetry research fields. The MCMEG addressed a multigroup dosimetric intercomparison exercise for modelling and simulating a case of prostate radiation therapy (RT) protocol. This

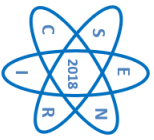
intercomparison was launched in order to obtain the dose distribution in the prostate target volume and in the neighboring organs. Dose assessments were achieved by using TLDs. A protocol using two pair of parallel-opposed fields were planned and performed with Alderson-Rando Pelvic Phantom. The assessed organs at risk were the urinary bladder, rectum and right and left femur heads. The RT simulations were performed using the MCNPx, MCNP6 and egs++ and BEAMnrc/DOSXYZnrc modules of EGSnrc Monte Carlo codes. The dose to the target volume, mean doses and standard deviation in the organs at risk, and dose volume data were computed. A comparison between the simulated results and the experimental values obtained from TLD measurements was made. In some cases the results obtained using MC simulations showed large deviations in comparison to the results obtained from the TLD measurements and these variations can be explained by the difficulties in the modelling of the geometry, selection of MC parameters required for the simulations and the statistical errors and inaccuracies in experimental measurements. Even though, the exercise has been a great opportunity for the MC groups to learn and share the main difficulties found during the modelling and the analysis of the results. Concerned to the obtained variations, the MCMEG team consider that this was expected for the level of complexity of the exercise and must be studied by the MC groups.

4. **Seniwal B**, Bhatt CP, Fonseca TC. Comparison of dosimetric accuracy of acuros XB and analytical anisotropic algorithm against Monte Carlo technique. *Biomedical Physics & Engineering Express*. 2020 Jan 31;6(1):015035.

This study reports the comparison between two dose calculation algorithms, Acuros XB 13.5 (AXB) and Analytical Anisotropic Algorithm (AAA) against Monte Carlo (MC) simulations for 3D-Conformal Radiation Therapy (3D-CRT) using a female pelvic rando phantom. 3D-CRT treatment plans were generated on the CT images of rando phantom using AXB and AAA with Source to Axis Distance (SAD) technique. Doses obtained using two algorithms and MC results were compared using MATLAB based software CERR. In house MATLAB code was developed to calculate the gamma dose distribution comparison in terms of dose difference (DD) and distance to agreement distribution (DTA). The results showed that the Dmean in the PTV TOTAL (PTV) volume for AXB and AAA was equal to the mean dose calculated by MC simulations. The gamma passing rates for AXB were more accurate in comparison to AAA with reference to MC for PTV, Bladder and Femoral Heads region. After analysing the dose comparison specially for the PTV, femoral heads, also the analysis of dose volume histogram (DVH) and gamma dose distribution comparison for PTV, femoral heads and bladder, it can be concluded that AXB is more accurate in comparison to AAA. It can be said that AXB is well suited for dose calculation in clinical setup when compared to MC calculations.

A.2 Events

1. IV SENCIR, Monte-Carlo modeling for evaluation of two different calculation algorithms, Week of Nuclear Engineering and Radiation Sciences, Department of Nuclear Engg., UFMG, BH, MG, Brazil. 2018 (Poster presentation).
2. 14th International Symposium on Radiation Physics, MCMEG : Intercomparison Exercise On Prostate Radiation Therapy Dose Assessment, 14th International Symposium on Radiation Physics, Cordoba, Argentina. 2018 (Poster Presentation).
3. XXIII CBFM, A Comparison Between Monte-Carlo Computations and Experimental Results Obtained With TLD Dosimetry for ART RANDO Pelvic Phantom A Case of Prostate Cancer and 3D-Conformal Radiation Therapy, XXIII Congresso Brasileiro de Fisica Medica, IX Encontro Gaucha de Fisica Medica e IV Simposio Sul Brasileiro de Fisica Medica realizado no Centro de Convencoes Barra Shopping Sul, Porto Alegre, RS, Brasil. 2018 (Poster presentation).
4. IDOS-2019, Microdosimetric calculations for I-123 using Geant4-DNA, International Symposium on Standards, Application and Quality Assurance in Medical Radiation Dosimetry (IDOS-2019), Vienna, Austria. (Oral Presentation: Presented by Prof. Telma C.F. Fonseca).
5. IDOS-2019, Study of the electrons range in soft tissue with the energy of 50keV, International Symposium on Standards, Application and Quality Assurance in Medical Radiation Dosimetry (IDOS-2019), Vienna, Austria. (Oral Presentation: Presented by Dr. Georgia Santos Joana).
6. Radiation Biology Summer School, Hokkaido University, Sapporo, Japan, Radiation Biology Summer School. 2019. (Workshop).
7. XIX ISSSD, Microdosimetric calculations for Iodine radioisotopes using Geant4-DNA. XIX International Symposium on Solid State Dosimetry, 2019 at Zacatecas, Zac., México. (Poster Presentation).
8. M3HPCST-2020, Modern Mathematical Methods and High Performance Computing in Science and Technology, Inderprastha Engineering College, Gaziabad, India. (Invited talk).
9. PANNANO2, Radio-biological calculations for Au-198 and Au-199 radioactive nanoparticles, The Second Pan American Nanotechnology Conference (PANNANO 2020), Aguas de Lindoia, SP, Brazil. (Oral Presentation).



Quarta Semana de Engenharia Nuclear e Ciências das Radiações
Belo Horizonte, 6 a 8 de novembro de 2018
Escola de Engenharia – Universidade Federal de Minas Gerais

CERTIFICADO

Certificamos que Baljeet Seniwal participou da IV SENCIR ocorrida entre os dias 6 e 8 de novembro de 2018 em Belo Horizonte e organizada pelo Departamento de Engenharia Nuclear e pelo Programa de Pós-graduação em Ciências e Técnicas Nucleares da Universidade Federal de Minas Gerais, tendo apresentado o trabalho MONTE-CARLO MODELLING FOR EVALUATION OF TWO DIFFERENT CALCULATION ALGORITHMS de autoria de Baljeet Seniwal, Telma C. F. Fonseca, Ranjit Singh, na Sessão de Pôsteres em 07/11/2018.

Antonella Lombardi Costa
Chefe do Dep. de Eng. Nuclear da UFMG
Coordenadora Geral da IV SENCIR

Clarysson Alberto Mello da Silva
Coordenador do Programa de Pós-graduação em
Ciências e Técnicas Nucleares da UFMG

Nº do registro: AR-021 em 12/11/2018



The Mexican Society of Irradiation and Dosimetry

CERTIFIES THAT

Baljeet Seniwai & Telma CF Fonseca

Presented the paper Microdosimetric calculations for Iodine radioisotopes using Geant4-DNA during the XIX International Symposium on Solid State Dosimetry held, from October 7th to 11th, 2019 at Zacatecas, Zac., México.


Dr. Hector R. Vega-Carrillo
Scientific committee chairperson



**The second Pan-American
Nanotechnology Conference**
Aguas de Lindoia, SP, Brazil - March 04 - 07, 2020

CERTIFICATE

03-007

We hereby certify that **Seniwal, B; Katti, K.V; Lugao, A.B; Fonseca, T** are authors of the paper entitled **Radio-biological calculations for Au-198 and Au-199 radioactive nanoparticles** presented by **Baljeet Seniwal** during The Second Pan-American Nanotechnology Conference (PANNANO 2020) held in Aguas de Lindoia, SP, Brazil - March 04 - 07, 2020.

Jointly organized by



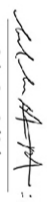
HOUSTON
UNIVERSITY
OF TEXAS

UNIVERSITY
OF KENTUCKY

THE
UNIVERSITY
OF TEXAS

Realization




Carlos Cesar Rod Bufon
CHAIR PANNANO 2020


Ademar Benvenoh Lugao
CHAIR PANNANO 2020

22/10/2018

cred30.siscone.com.br/Comprovantes/Emissao.aspx

**CERTIFICADO DE APRESENTAÇÃO DE TRABALHO**

Certificamos que o trabalho de autoria de: **Maria Angelina Mendes; Baljeet Senival; Priscila do Carmo Santana; Lucas Paixão Reis; Bruno Melo Mendes; Peterson Lima Squair; Marco Aurélio de Sousa Lacerda; Jony Marques Geraldo; Fernanda Martins Bastos; Luiz Claudio Meira-Belo; Telma Fonseca**

Título do trabalho: **A COMPARISON BETWEEN MONTE-CARLO COMPUTATIONS AND EXPERIMENTAL RESULTS OBTAINED WITH TLD DOSIMETRY FOR ART RANDO PELVIC PHANTOM A CASE OF PROSTATE CANCER AND 3D- CONFORMAL RADIATION THERAPY**

foi apresentado na forma **Apresentação Poster** em **XXIII Congresso Brasileiro de Física Médica, IX Encontro Gaúcho de Física Médica e IV Simpósio Sul Brasileiro de Física Médica** realizado no Centro de Convenções Barra Shopping Sul, Porto Alegre, RS, Brasil de 06 a 08 de setembro de 2018.

Porto Alegre, 08 de setembro de 2018

Comitê Científico
XXIII Congresso Brasileiro de Física Médica
IX Encontro Gaúcho de Física Médica
IV Simpósio Sul Brasileiro de Física Médica

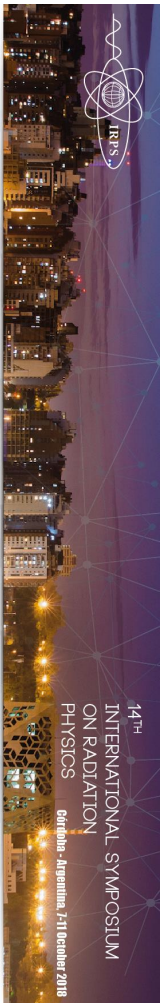
Autenticação: 27868447667898144

A autenticidade deste documento pode ser confirmada em: <http://cred30.siscone.com.br/Comprovantes/ValidarCertificado.aspx?Param=1615>

www.cbfm2018.com.br

<http://cred30.siscone.com.br/Comprovantes/Emissao.aspx>

1/1




Peterson Lima Squair

has attended and presented the work “*MCMEG: InterComparison exercise on radiotherapy assessment prostate dose*” *Fonseca T. C. F., Senival B., Mendes A. M., Belo M. C. L., Lacerda M. A. S., Mendes M. B., Paixão R. L., Joana G. S., Santana P., Marques J., Squair L. P., Antunes P., Yoriyaz H., Bastos F.*, as **poster** in the **14th International Symposium on Radiation Physics ISRP-14**, on October 7th-11th, 2018.

Córdoba, Argentina, October 11th, 2018.



Marcelo Ribbo
ISRP-14 Chairman



Carlos Walter Robledo
Minister of Science and Technology
Government of Córdoba



Christopher Thomas Chantler
President
International Radiation Physics Society



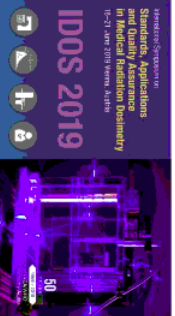




International Symposium...

18-21 June 2019
International Symposium on Standards, Applications and Quality Assurance in Medical Radiation Dosimetry (IDOS-2019)
 Conference

Standards, Applications and Quality Assurance in Medical Radiation Dosimetry
 18-21 June 2019, Bonn, Austria



Profile

Telma C.F. Fonseca
 Departamento de Engenharia Nuclear UFMG

Profile

Georgia Santos Joana
 National Nuclear Energy Commission (CNEA)

Organisation: Departamento de Engenharia Nuclear UFMG

Organisation: National Nuclear Energy Commission (CNEA)

Sessions

4:30 PM
Microdosimetric calculations for I-123 using Geant4-DNA

4:00 PM
Study of the electrons range in soft tissue with the energy of 50 keV

Programme

Microdosimetric calculations for I-123 using Geant4-DNA
 09:41:15 PM 4:30 PM ● Fonseca

Study of the electrons range in soft tissue with the energy of 50 keV
 04:00 PM 4:15 PM ● Topical

Speakers

Speaker
Telma C.F. Fonseca
 Departamento de Engenharia Nuclear UFMG

Speaker
Georgia Santos Joana
 National Nuclear Energy Commission (CNEA)

Participants

Cooperating Organizations

Exhibitors

Announcements

Floorplans

Exhibitor Area

Conference Information

Appendix B

Validation of IRT based extension to TOPAS in terms of impact of variable concentration of scavengers on radiochemistry of water

Baljeet Seniwal¹, Jose Ramos-Méndez³, Jan Schuemann², Telma C.F. Fonseca¹

¹Departamento de Engenharia Nuclear (DEN/UFMG) & Programa de Pós-graduação em Ciências e Técnicas Nucleares (PCTN) - Universidade Federal de Minas Gerais (UFMG), Av. Antônio Carlos, 6627, Pampulha, 31270-901, Belo Horizonte, MG, Brazil

²Department of Radiation Oncology, Massachusetts General Hospital and Harvard Medical School, Boston, MA, United States of America

³Department of Radiation Oncology, University of California San Francisco, San Francisco, CA, United States of America

Note: Unpublished article.

Abstract

In this study we validate the new independent reaction time (IRT) based, under development, new extension of TOPAS. It is capable of simulating the radiochemistry of water post radiation exposure. Here we present the simulation results investigating the impact of the presence of several scavengers: O₂, glutathione, CH₃OH, NaNO₃ and Na₂SO₄, in variable concentration, on the radiolysis of water. The G-value, representing the

number of chemical species formed per 100 eV of energy transfer, for production (or consumption) of reactive species was estimated. The calculated G-values were found in good agreement with literature. For O₂, glutathione, CH₃OH, and NaNO₃ all discrepancies were found less than 10%. The observed differences were attributed to the difference in the physics models used by different Monte Carlo codes. The largest differences, ≈35%, were observed in the yield of H₂O₂, when Na₂SO₄ was used as scavenger to scavenge hydrated electrons and its precursors. These differences were maybe the consequence of not considering second order reactions in the simulation. In order to resolve this issue we proposed a mixed approach. It uses both Monte Carlo calculated yield and analytical solution, and circumvents the issue of large differences.

Keywords: Radiochemistry of water, TOPAS, Independent reaction time, scavengers, G-value.

B.1 Introduction

The interaction of ionizing radiation with biological tissues results in excitation or ionization of its water molecules, which consequently creates reactive species for instance e_{aq}⁻, H[•], [•]OH, H₂O₂ and H₂ [193]. The reactive radiolytic species are formed just after, within a few picosecond (ps), the radiation exposure, followed by the diffusion within the surrounding medium and chemical reactions with the neighbouring molecule occurs. The reaction of these reactive species with the DNA molecules at nuclear level is termed as indirect effect of radiation [194, 194–197]. Also, such chemical reactions are basis of chemical dosimeters for instance ceramic sulphate [198, 199] and Fricke dosimeters [200]. Therefore the radiation chemistry of water is of great importance in both chemical dosimetry and radiobiology.

The radiochemistry of water is reported to be effected by several factors. One such factor is presence of scavengers [201, 202]. For instance the presence of oxygen improves the radiosensitivity of tumor cells towards low-LET ionizing radiation [203]. Colliaux et al. used Monte Carlo methods to investigate the impact of presence of oxygen and an antioxidant, glutathione (GSH), in different concentrations on radiochemistry of water [202]. The effect of presence of O₂/GSH was quantified by estimating the yield of HO₂[•]/O₂^{-•} radicals. As, the O₂/GSH scavenges H[•] and e_{aq}⁻ and leads to production of HO₂[•]/O₂^{-•} radicals. Also, the presence of these radicals, is reported to enhance the toxicity of radiation within the biological tissue [204–208]. The scavengers, in different concentrations, are also used to understand the radiochemistry of water, and pathway of formation of one particular reactive species. For instance, Hiroshi et al. used both experimental and diffusion kinetic modeling methods to investigate the time dependent yield of H₂O₂ [201]. Authors used methanol (CH₃H/MeOH)

to scavenge $\cdot\text{OH}$ radical and its precursor, and NaNO_3 or Na_2SeO_4 to scavenge e_{aq}^- and its precursors. The yield of H_2O_2 as a function of scavenging capacity of MeOH.

There are two main stochastic methods reported in literature, which can be used to simulate the radiolysis of water. The first one is the step by step method (SBS), it simulates the detailed evolution of the track structure by following the particle trajectories in detail and has been reported as the accurate representation of kinetics. The other method is, independent reaction time (IRT) method is an approximate Monte Carlo method, makes use of independent pairs approximation and is much faster than SBS method. It can be used to simulate the radiochemistry of water in terms of reaction times without simulating and following the trajectory of diffusing reactive species. The detailed description of these methods can be found else where [209–212]. In the recent years, either one or both of these methods have been implemented to several Monte Carlo codes, namely PARTRAC [213, 214], RI-TRACK [215, 212], GEANT4-DNA [216], and TRAX [217].

In this article we present the validation of IRT based extension to TOPAS [38, 218] Monte Carlo software. We simulated the impact of 5 scavengers: O_2 , MeOH, GSH, NaNO_3 and Na_2SeO_4 on the radiochemistry of water in terms of G-value. The computed results were compared with the literature [201, 202]. The current implementation simulates first order kinetics only. However, some of the considered scavengers have second order reactions as well. In order to solve the issue of second order kinetics, we proposed a mixed approach. The mixed approach considers computed G-value and uses a simple mathematical relation to estimate the net yield of the chemical species.

B.2 Material and Methods

B.2.1 Monte Carlo code: TOPAS

The TOPAS Monte Carlo tool [38, 218] extends and wraps GEANT4 [219] Monte Carlo toolkit. It allows the users to model complex radiotherapy applications without knowledge of computer programming. Also, the TOPAS Extension Framework allows the expert user to write their own extensions to TOPAS. The TOPAS-nBio [220], extension to TOPAS, allows user to perform track structure simulations. It provides interface to the physics and chemistry processes of Geant4-DNA [40]. The radiochemistry of water post radiation exposure [221] and complex radiobiological geometries [222, 223] can be simulated and radiobiological quantities can be calculated. It also allows user to use advanced computational tools like: variance reduction techniques [224], 4D simulations [225], and multithreading [226].

B.2.2 Simulation of radiolysis of water and simulation setup:

The simulation of radiochemistry of water post radiation exposure is divided into three stages. The first stage is known as physical stage, lasts for $< 10^{-15}s$, where primary and secondary ionizing particles interact with water molecules. In this stage the ionization, excitation and vibrational excitation of water molecules are simulated. The second stage is known as physicochemical stage, which lasts between $10^{-15}s$ to $10^{-12}s$. In this stage the thermalized electrons were solvated, and excited (H_2O^*) and ionized water (H_2O^+) molecules were simulated. The third stage is known as chemical stage, it lasts between $10^{-12}s$ to $10^{-6}s$. In this stage the diffusion and chemical reactions among chemical species, produced in physicochemical stage, are simulated. It results in production of new chemical products and reduction in the number of old reactive species. For simplicity, it is generally assumed that all chemical reactions occur during the chemical stage and after $10^{-6}s$ all chemical products are homogeneously distributed.

In this work the physical stage was simulated using TsEmDNAPhysics physics constructor. The physicochemical stage was simulated using TsEmDNAChemistry constructor, which includes revised chemistry parameters. Also, the branching ratios and dissociation schemes used in this work were same as used by Ref. [221], in the development of chemical module of TOPAS-nBio. The last stage, chemical stage, was simulated using the under development TOPAS extension, based on independent reaction time (IRT) technique. IRT technique has been extensively described in the literature [211]. The chemical reactions considered in the radiolysis of deaerated water, involving: hydrated electron (e^-_{aq}), hydroxy ($\cdot OH$) and hydrogen ($H\cdot$) free radical, hydronium ion (H_3O^+) and hydrogen peroxide (H_2O_2), are reported in Table B.1. The TOPAS extension was built over Topas_3_2_p2 version of TOPAS, contains pre-build versions of Geant4 10.5.p01. All simulations were performed on intel core i5 CPU with 8 Giga bites of RAM.

Table B.1 List of chemical reactions, for radiolysis of deaerated water, and their reaction rate constants (k) used in this work

	Reaction	k ($10^{10} .M^{-1} .s^{-1}$)
R1	$e_{aq}^- + e_{aq}^- \longrightarrow H_2 + 2 OH^-$	0.636
R2	$e_{aq}^- + \cdot OH \longrightarrow OH^-$	2.95
R3	$e_{aq}^- + H\cdot \longrightarrow H_2 + OH^-$	2.5
R4	$e_{aq}^- + H_3O^+ \longrightarrow H\cdot$	2.11
R5	$e_{aq}^- + H_2O_2 \longrightarrow \cdot OH + OH^-$	1.10
R6	$\cdot OH + \cdot OH \longrightarrow H_2O_2$	0.55
R7	$H\cdot + \cdot OH \longrightarrow H_2O$	1.55
R8	$H\cdot + H\cdot \longrightarrow H_2$	0.503
R9	$H_3O^+ + OH^- \longrightarrow H_2O$	11.3

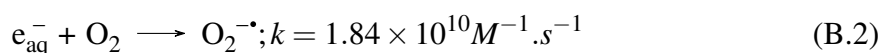
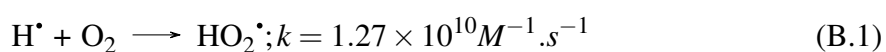
The estimated kinetics reported in this study were obtained by irradiating cubical water (*G4_WATER*) phantom of size 1 km X 1 km X 1 km with monoenergetic, isotropic and point electron source with initial energy of 1 MeV, placed at the center of the phantom. The size of the phantom was large enough to stop all the secondary particles generated by the primary electrons. Also, only a segment, first 10 keV, of the physical track generated by 1 MeV electron was simulated. That is, the primary track of electron was terminated once the accumulated energy along the electron track gets higher than 10 keV and all generated secondaries were simulated. The production (or consumption) of chemical species at specific time, between $10^{-12}s$ to $10^{-6}s$ (or) $10^{-5}s$, per 100 eV of deposited energy, also known as G-value [227], was estimated. The number of particles simulated was such that the statistical uncertainty was less than 1%.

B.2.3 Scavengers and their reaction kinetics

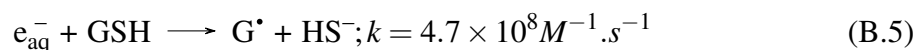
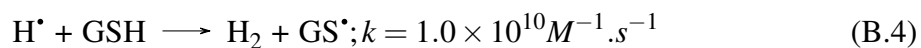
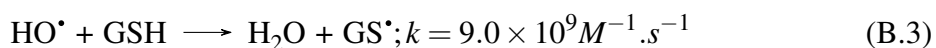
The new, under development, IRT based TOPAS extension was validated using five scavengers: Oxygen (O_2), Glutathione (GSH), Sodium nitrate ($NaNO_3$), Sodium selenate decahydrate (Na_2SeO_4), and Methanol (MeOH). In the simulation of these kinetics, no effect of pH or temprature were considered. Only first order kinetics was simulated, that is once the products were obtained no further reactions of produced products was considered. The added scavengers were considered as continuum and it was also assumed that the scavenging molecules do not get effected by the radiation exposure.

Different concentrations of O_2 , GSH were used to investigate the impact of different concentration of scavengers on radiochemistry of water post irradiation. Also, for O_2 and GSH, the

results published by Ref. [202] were used as reference. The considered chemical reactions and reaction rate for O_2 are presented in chemical Equation B.1 and Equation B.2, where O_2 reacts with H^\bullet and yields HO_2^\bullet , and with e_{aq}^- to produce $O_2^{\bullet-}$. The different concentration of O_2 ($[O_2]$) dissolved in was related to the partial pressure of O_2 in air at standard pressure conditions. The partial pressure of O_2 and its concentration were related using Henry law, with Henry constant of $1.3 \times 10^{-3} \text{ Mol.l}^{-1} \text{ bar}^{-1}$, which is the $[O_2]$ in water at 298 K. Using Henry law, it can be found that $[O_2] = 0.27 \text{ mM}$ corresponds to 160 mmHg partial pressure of O_2 . Reactions of O_2 :

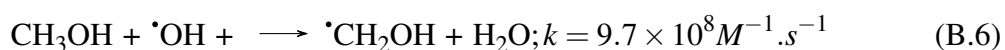


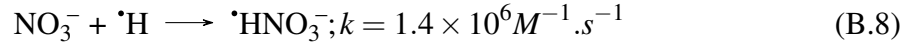
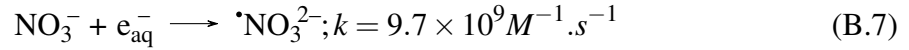
Whereas, three concentrations for GSH were considered: 0, 1 and 10 mM. The chemical reactions involved with GSH are presented in chemical Equation B.3, B.4 and B.5. Reactions of GSH (antioxidant):



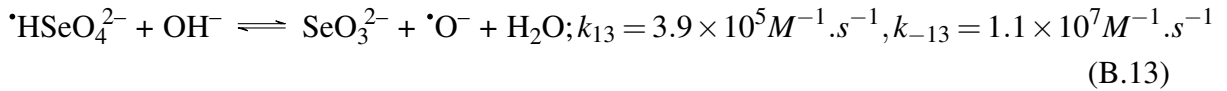
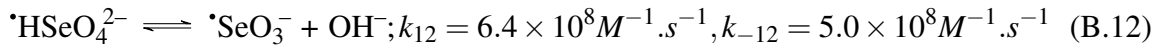
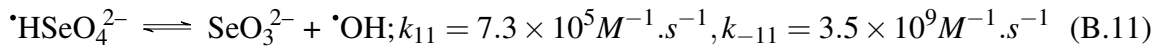
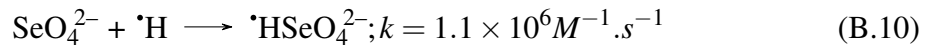
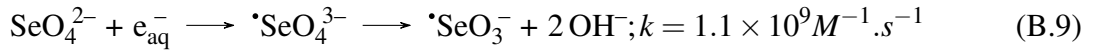
For O_2 , the obtained results are presented in terms of production of $HO_2^\bullet + O_2^{\bullet-}$ per 100 eV for variable partial pressure of O_2 . Whereas, for GSH, it is presented in terms of consumption of e_{aq}^- and H^\bullet per 100 eV for variable time interval and different GSH concentrations ($[GSH]$). Ref. [201], used variable concentrations of scavengers: MeOH, $NaNO_3$ and Na_2SeO_4 , in order to understand the pathways of radiolysis of water and formation of H_2O_2 . In this work we used their published results as reference. Where, MeOH scavenges $^\bullet OH$ and its precursors and both $NaNO_3$ and Na_2SeO_4 scavenge $^\bullet H$ and e_{aq}^- . The chemical reactions and reaction rates considered are presented in Equation B.6 - B.10. The results are presented in terms of production of H_2O_2 as a function of product of reaction rate constant for MeOH (see Equation B.6) and $[MeOH]$. The $[MeOH]$ was varied from $1.0 \times 10^{-06} \text{ M}$ to 1.0 M; the $[NaNO_3]$ was varied from 0.25 mM to 0.25 M; and the $[Na_2SeO_4]$ was varied from 2.5 mM to 0.25 M.

Reactions to estimate $G(H_2O_2)$ as a function of scavenging capacity of MeOH for different $[NO_3^-]$:





Reactions to estimate $G(\text{H}_2\text{O}_2)$ as a function of scavenging capacity of MeOH for different $[\text{SeO}_4^{2-}]$:



B.2.4 Analytical approach

As it is mentioned above that only first order kinetics were simulated. However, it can be observed from chemical reaction Equation B.11, B.12 and B.13 that $\cdot\text{HSeO}_4^{2-}$ can decompose and produce $\cdot\text{OH}$ or OH^- . Which we consequently can result in increase in production of H_2O_2 . Hence, a hit and trial based analytical method was designed to consider the contribution of $\cdot\text{HSeO}_4^{2-}$ to the yield of H_2O_2 .

The analytical method was applied in two step: (i) the yield of H_2O_2 ($G(\text{H}_2\text{O}_2)$) and $\cdot\text{HSeO}_4^{2-}$ ($G(\cdot\text{HSeO}_4^{2-})$) at $10 \mu\text{s}$ was obtained, using the methodology discussed in subsection 2.3, for different $[\text{SeO}_4^{2-}]$ and different scavenging capacities of MeOH. (ii) $\cdot\text{HSeO}_4^{2-}$ was expected to decompose to $\cdot\text{OH}$, and consequently form H_2O_2 (see Table B.1). The net yield of H_2O_2 (Net $G(\text{H}_2\text{O}_2)$) was estimated as follows :

$$\text{Net}G(\text{H}_2\text{O}_2) = G(\text{H}_2\text{O}_2) + A \times G(\cdot\text{HSeO}_4^{2-}) \quad (\text{B.14})$$

Where, A is the fraction of $\cdot\text{HSeO}_4^{2-}$ converts to H_2O_2 . In the text the obtained Net $G(\text{H}_2\text{O}_2)$ is denoted by IRT + Analytical (see Figure B.4 and B.5).

B.3 Results

In this work we validated the new under development radiochemistry based extension to TOPAS, using independent reaction time technique (IRT). The radiochemistry of water was

studied in the presence of several scavengers: O_2 , GSH, MeOH, $NaNO_3$, and Na_2SeO_4 . The validation was performed by comparing the predicted G-value, number of reactive species produced (or consumed) per 100 keV of deposited energy, with the literature. The G-value was calculated for 1 MeV monoenergetic, isotropic electron source placed at the center of cubical phantom of dimensions $1 \times 1 \times 1 \text{ km}^3$. The first 10 keV of primary track and its secondaries were simulated in this work.

From Equation B.4 and Equation B.5, it can be observed that the presence of an antioxidant (GSH), increases the consumption of both hydrated electron and hydrogen free radical. Figure B.1 reports the consumption of hydrated electron (e_{aq}^-) and hydrogen free radical (H^\bullet) from 1 ps to 1 μs for variable concentration of GSH: 0, 1, and 10 mM. The calculations were performed using the methodology described in subsection 2.2 and 2.3. The obtained results were compared against the results published by Ref. [202]. For $G(e_{aq}^-)$ (see Figure B.1 (A)), our calculated consumption was underestimated by about 8% for all concentration of GSH in comparison to the literature. This underestimation reduced to less than 5% after 100 ps. Whereas for $G(H^\bullet)$ (Figure B.1 (B)) nearly complete overlap of estimated kinetics and literature was observed. All the differences were less than 5%.

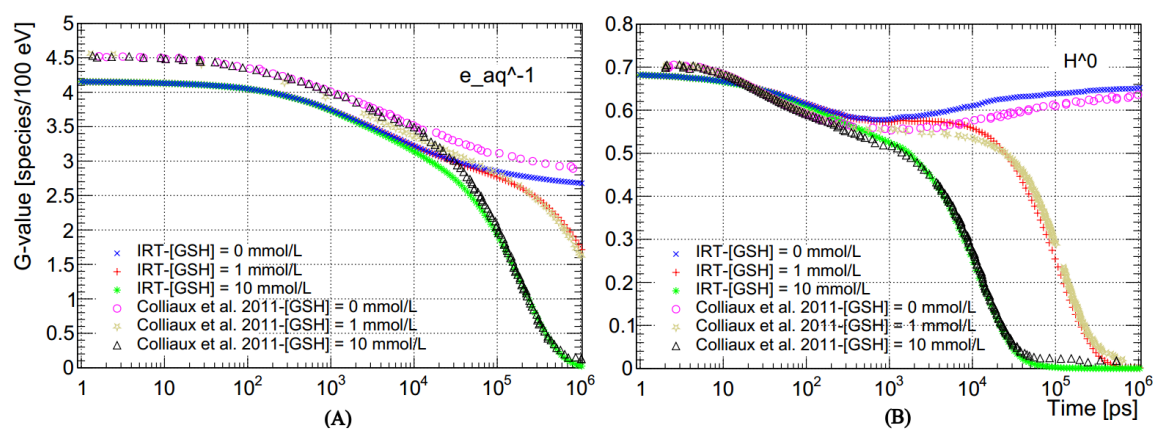


Figure B.1 $G(e_{aq}^-)$ and $G(H^\bullet)$ as a function of time generated first 10 keV of 1 MeV electron source in water with [GSH] of 0, 1, 10 mM.

As it is evident from Equation B.1 and Equation B.2 that O_2 reacts with e_{aq}^- (yields HO_2^\bullet) and H^\bullet (yields $O_2^{\bullet-}$). Hence, combined yield of $HO_2^\bullet + O_2^{\bullet-}$, $G(HO_2^\bullet + O_2^{\bullet-})$, was estimated for different partial pressure of O_2 in air. Figure B.2 reports $G(HO_2^\bullet + O_2^{\bullet-})$ as a function of partial pressure of O_2 . In Figure B.2 (A) the reaction kinetics were simulated from 1 ps to 1 μs . Whereas, in case of Figure B.2 (B) the kinetics was simulated from 1 ps to 10 μs . Also, the estimated yield of $HO_2^\bullet + O_2^{\bullet-}$ in the presence of GSH = 1 mM, for variable O_2 partial pressure is presented in Figure B.2(C), simulating kinetics up to 10 μs .

The combined effect of Equation B.1, B.2, B.4 and B.5 is expected in the last case. Where, the yield $\text{HO}_2^\bullet + \text{O}_2^{-\bullet}$ is increased due to the presence of O_2 and decrease due to the presence of GSH.

From the results it was observed that for Figure B.2 (A), the differences were less than 7% between our calculated $G(\text{HO}_2^\bullet + \text{O}_2^{-\bullet})$ and literature, for O_2 partial pressure ranging from 0 to 200 mmHg. Whereas, when the output of same kinetics was obtained at $10 \mu\text{s}$, Figure B.2 (B), complete overlap of estimated and published G-values was observed up to 15 mmHg pressure of O_2 . After 15 mmHg, the difference between estimated and published G-values increases. Similar to the observation of Figure B.2 (B), in the presence of 1 mM GSH for variable partial pressure of O_2 almost complete overlap of estimated G-value curve and the curve reported by Ref. [202] was observed up to 30 mmHg. After 30 mmHg partial pressure there the increase in differences between the two curves with increase in partial pressure of O_2 was observed ($\approx 15\%$).

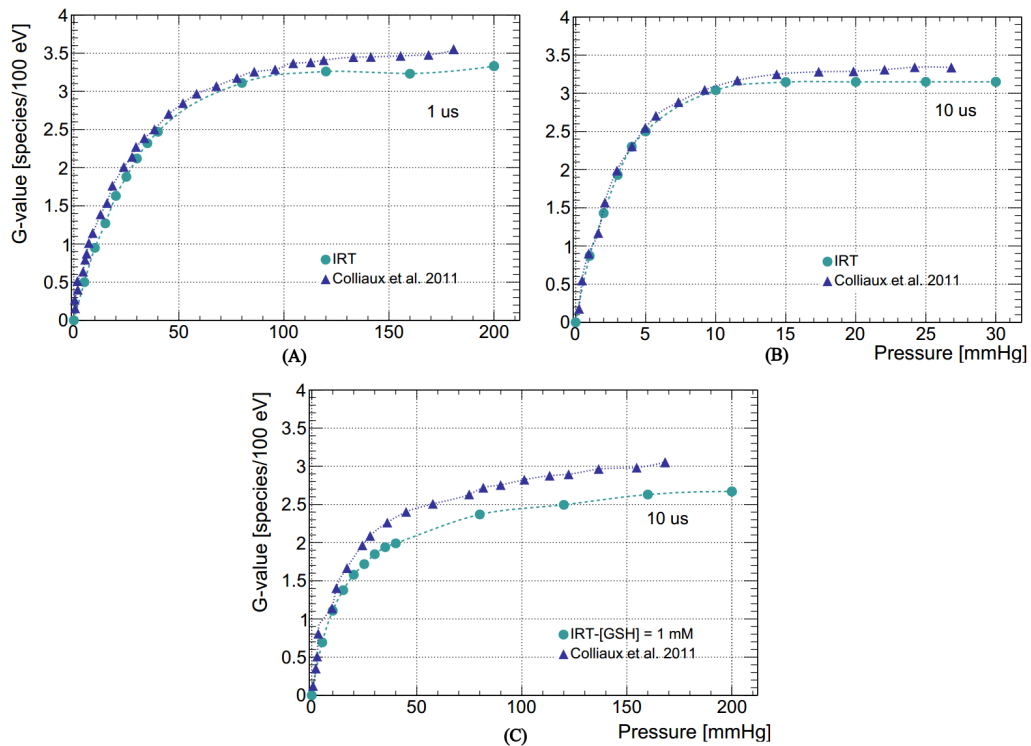


Figure B.2 $G(\text{HO}_2^\bullet + \text{O}_2^{-\bullet})$ as a function of partial pressure of O_2 in air as a function of time generated from first 10 keV of 1 MeV electron source in water: (A) at $1 \mu\text{s}$, (B) at $10 \mu\text{s}$, and (C) at $10 \mu\text{s}$ with $[\text{GSH}] = 1 \text{ mM}$.

Overall good agreement between the literature and IRT calculated G-value as function of scavenging capacity was observed. Here the observed differences in most of the cases were

less than 10%. These differences can be attributed to the differences in the physical models used in Geant4-DNA and TRAX Monte Carlo code [217], used by Ref. [202].

Hiroki et al. [201], used scavengers to scavenge $\cdot\text{OH}$ and e_{aq}^{-1} , and their precursors, with a aim to understand the pathway of formation of H_2O_2 in radiochemistry of water. Where, methanol (CH_3OH) was selected to scavenge O_2 and its precursors. Also, NaNO_3 or Na_2SeO_4 were used as scavengers to scavenge e_{aq}^{-1} and its precursors (see Equation B.6 to Equation B.10). In this work we reproduced the results published by Ref. [201] using new IRT based extension of TOPAS. Figure B.3 reports yield of H_2O_2 ($G(\text{H}_2\text{O}_2)$) as a function of scavenging capacity of CH_3OH , (MeOH), where scavenging capacity = reaction rate constant X $[\text{MeOH}]$. The concentration of NaNO_3 ($[\text{NO}_3^-]$) considered were: 0.25 mM (Figure B.3 (A)), 2.5 mM (Figure B.3 (B)), 25 mM (Figure B.3 (C)) and 0.25 M (Figure B.3 (D)). The overestimation of up to $\approx 20\%$ in the consumption of H_2O_2 was observed for $[\text{NO}_3^-] = 0.25$ mM. However, for other concentrations, the differences were less than 5%.

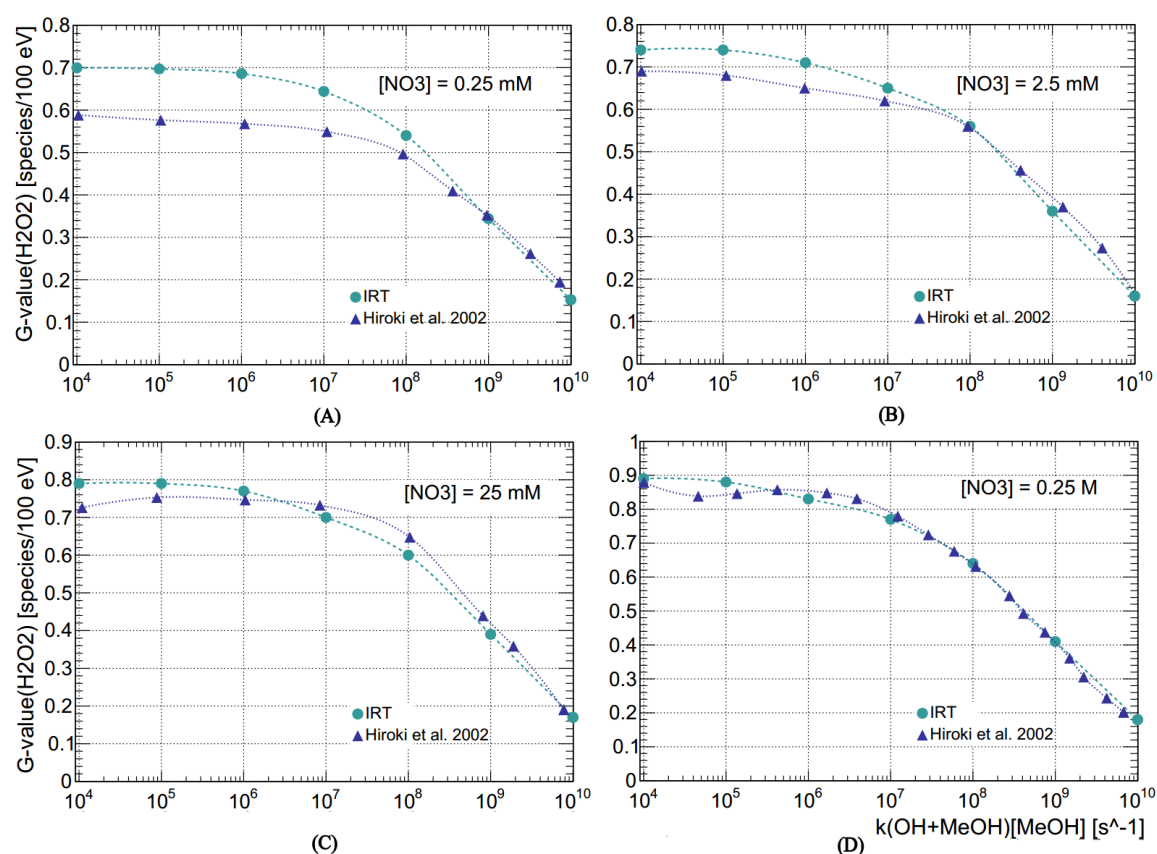


Figure B.3 $G(\text{H}_2\text{O}_2)$ in the gamma-radiolysis of water (1 MeV electron source (simulating first 10 keV)) as function of the scavenging capacity of MeOH for $[\text{NO}_3^-] = 0.25, 2.5, 25$ mM, and 0.25 M

This overestimation of $G(\text{H}_2\text{O}_2)$ at low scavenging capacities of MeOH for $[\text{NO}_3^-] = 0.25$ mM can be due to: (a) at low scavenging capacities MeOH is not able to scavenge all H_2O_2 molecules, (b) H_2O_2 due to low concentration of NO_3^- , e_{aq}^- are also not completely removed, and (c) the R5 in Table B.1 can take place and increase the amount of OH^\bullet (as well as H_2O_2). Also, the comparison of calculated consumption of Na_2SeO_4 (or SeO_4^{2-}) is reported in Figure B.4, for $[\text{Na}_2\text{SeO}_4] = 2.5$ mM, 25 mM and 0.25 M as a function of scavenging capacity of MeOH. The IRT computed yield of H_2O_2 was found underestimated by: 13% for 2.5 mM, 15% for 25 mM and 35% for 0.25 M. This underestimation was higher at low scavenging capacities of MeOH (between 10^4 s^{-1} to 10^6 s^{-1}). It maybe because the computations performed using IRT (explained in subsection 2.3) considers only first order kinetics. That is, the contribution of equilibrium chemical reactions mentioned in Equation B.11, B.12 and B.13 in the regeneration of OH^\bullet (consequently increase in yield of H_2O_2) from HSeO_4^{2-} was not considered. In order to consider this contribution we used mixed approach (described in subsection 2.4), which considers both IRT calculated G-values and fraction of HSeO_4^{2-} that converts to H_2O_2 . The results obtained using mixed approach are presented as "IRT+Analytical". The G-value(H_2O_2) obtained using mixed approach were more consistent with the literature. It was found that almost 100% of HSeO_4^{2-} dissociated to OH^\bullet . This resulted in high G-value(H_2O_2), specially for low scavenging capacity of MeOH (between $1\text{E}+04$ to $1\text{E}+06$). However, at high MeOH with high scavenging capacity is capable of scavenging all the OH^\bullet , consequently preventing the formation of H_2O_2 .

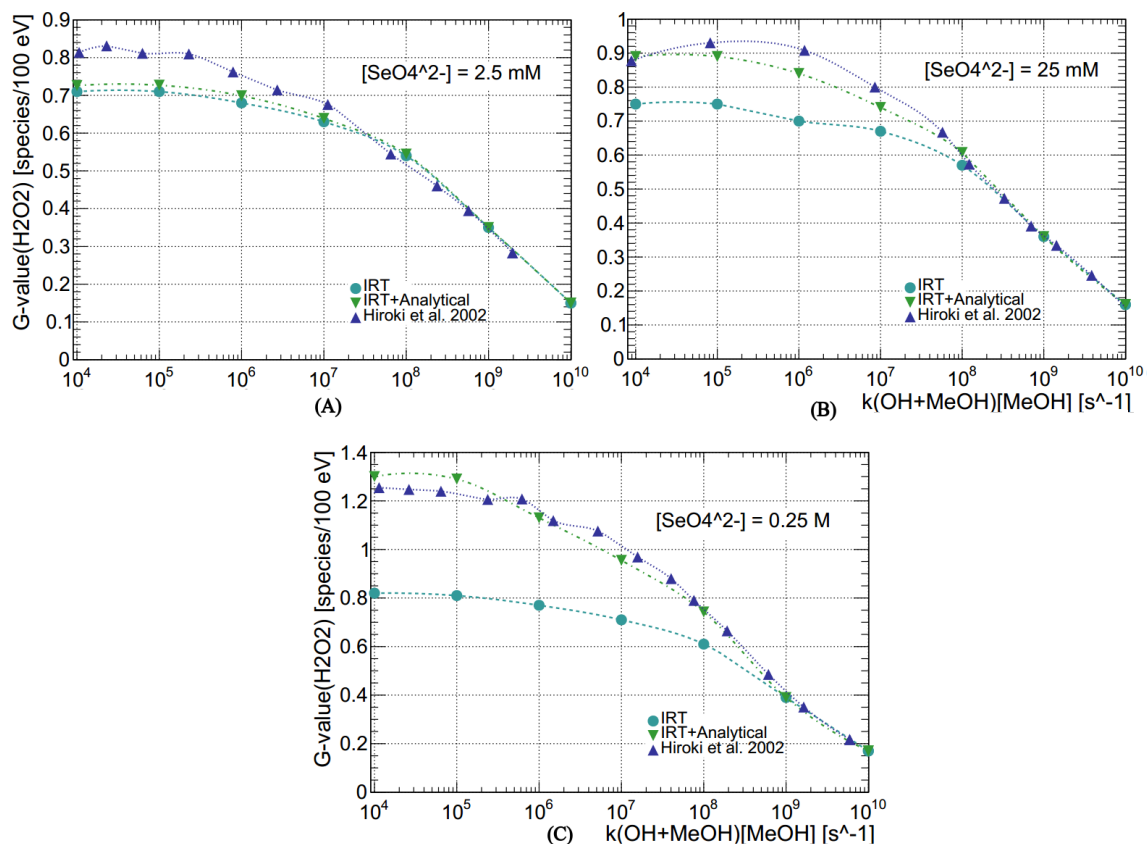


Figure B.4 G(H₂O₂) in the gamma-radiolysis of water (1 MeV electron source (simulating first 10 keV)) as function of the scavenging capacity of MeOH for [SeO₄²⁻] = 2.5, 25 mM, and 0.25 M

In Figure B.5 we present the comparison of the G-value(H₂O₂), when [NaNO₃] = [Na₂SeO₄] is used (Figure B.5(A)) or when [Na₂SeO₄] = 10 X [NaNO₃] (Figure B.5(B)), as a function of scavenging capacity of MeOH. The computed results were compared with the literature [201]. From the Figure B.5, it can be observed that the calculated G-value(H₂O₂) for NO₃⁻ match very well with published data, all differences less than 5%, and change in concentration do not impact the H₂O₂. Other important finding that needs attention is the yield of H₂O₂ for SeO₄²⁻, calculated using IRT, it almost overlaps the yield obtained with NO₃⁻. It maybe because the reaction rates constants of chemical reactions mentioned in Equation B.7 and B.8, and Equation B.9 and B.10 are approximately equal. Also, the IRT calculated G-value(H₂O₂) curve was found deviating by ≈35% from the literature. However, the G-value curve estimated using the mixed approach matched very well with literature [201]. It suggests the importance of considering second order reactions in modeling the second order kinetics while studying the radiolysis of water.

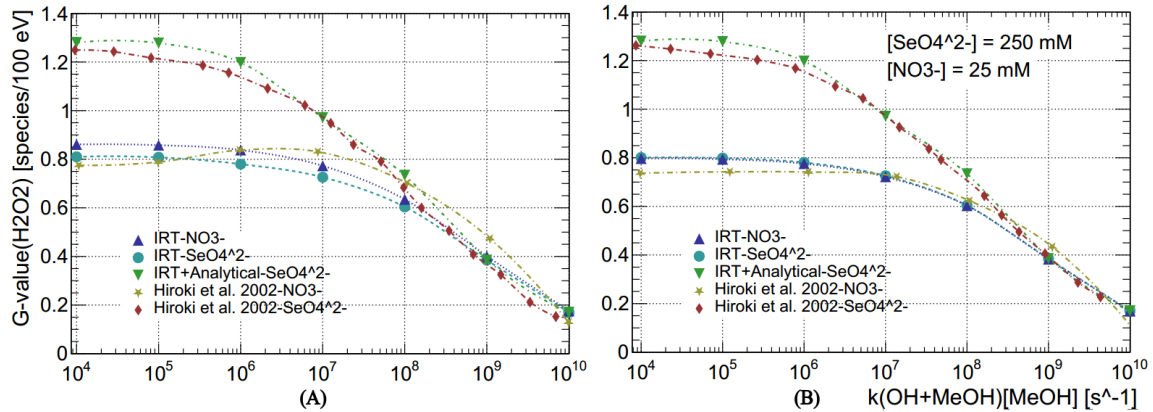


Figure B.5 $G(\text{H}_2\text{O}_2)$ in the gamma-radiolysis of water (1 MeV electron source (simulating first 10 keV)) as function of the scavenging capacity of MeOH for $[\text{SeO}_4^{2-}] = [\text{NO}_3^-] = 250$ mM and $[\text{SeO}_4^{2-}] = 250$ mM and $[\text{NO}_3^-] = 25$ mM.

From above presented results it can be suggested that the IRT based implementation in TOPAS, in order to model the radiochemistry of water post irradiation, is well implemented. The discrepancies observed are mainly caused by (i) the differences in the physics models used by different Monte Carlo codes, or (ii) no considering the second order kinetics.

B.4 Conclusion

In this article we presented the validation of new independent reaction time (IRT) based extension, underdevelopment, of TOPAS, which can be used to simulate the radiochemistry of water following radiation exposure. We calculated the yield of several reactive species in terms of, number of reactive species produced per 100 keV of energy deposited, termed as G-value. The simulation setup consisted of cubical water phantom of 1 km side width. Monoenergetic, isotropic, point electron source with initial energy 1 MeV was placed at the center of this phantom. In order to simulate the radiochemistry of water first 10 keV the primary track, of 1 MeV, and its secondaries were simulated. The calculated G-values were compared against the data published in literature. Here 5 scavengers: O_2 , glutathione, NaNO_3 , Na_2SeO_4 , and CH_3OH , were considered and their effect on the radiolysis of water was computed in terms of G-values. It was found that in most of the cases the calculated G-value curves matched very well with the literature, with discrepancies less than 10%. Largest discrepancies, $\approx 35\%$, were observed in the case of Na_2SeO_4 . It maybe attributed to the limitation of current version of Monte Carlo code implementation, as it only considers first order kinetics. In order to resolve this we proposed a mixed approach, which considers

the contribution from both Monte Carlo calculated and analytically estimated G-values. From the obtained results it was concluded that the IRT based Monte Carlo extension is well implemented and the observed differences are caused by the differences in (i) physics models used to simulate the tracks, (ii) not considering second order kinetics in the simulation. One simple solution to the later will be to use a mixed approach, because implementing second order kinetics is a challenge because in most of the cases the second order kinetics and their reaction constants are unknown.

Appendix C

Monte Carlo settings used

Here Monte Carlo settings used in each study reported in this PhD thesis are reported. The recommendations given by AAPM Research Committee Task Group 268 [228] were considered in this reporting.

C.1 Chapter 2: Monte Carlo Assessment of Low Energy Electron Range in Liquid Water and Dosimetry Effects

C.1.1 EGSnrc

Table C.1 Monte Carlo methods table: EGSnrc.

S. No.	Item name	Description
1	Code, version/release date	EGSnrc-2020 release
2	Validation	Intercomparison with several MC codes in terms of sDPK
3	Timing	0.30 to 1.36 hours
4	Source description	Isotropic, Monoenergetic and Point electron source with $E_0 = 1$ keV to 50 keV
5	Cross-sections	Moller cross sections for e^-e^- and Bhabha cross sections for e^-e^+ interactions
6	Transport parameters	BCA = EXACT algorithm; skin depth for BCA = 3 Global AP = Global PCUT = 1 keV; and Global AE = Global ECUT = 512 keV
7	VRT and/or AEIT	No VRT or AEIT
8	Scored quantities	Energy deposited in each surrounding spherical shell
9	#histories/statistical uncertainty	$1E+07/<1\%$
10	Statistical methods	History by history method
11	Postprocessing	Energy deposited information was used to estimate sDPK

C.1.2 Geant4-DNA

Table C.2 Monte Carlo methods table: Geant4-DNA.

S. No.	Item name	Description
1	Code, version/release date	geant4.10.05.p01
2	Validation	Intercomparison with several MC codes in terms of sDPK
3	Timing	0.77 to 30.14 hours
4	Source description	Isotropic, Monoenergetic and Point electron source with $E_0 = 1$ keV to 50 keV
5	Cross-sections	uses complex dielectric response function to estimate cross-sections (see Ref. [40])
6	Transport parameters	G4EmDNAPhysics-option2 (see Ref. [40]) Energy cut of 100 eV for $E_0 = 1$ keV and 1 keV for $E_0 = 5$ keV to 50 keV
7	VRT and/or AEIT	No VRT or AEIT
8	Scored quantities	Energy deposited in each surrounding spherical shell
9	#histories/statistical uncertainty	$1E+05 < 1\%$
10	Statistical methods	Standard deviation was used to estimate statistical error
11	Postprocessing	Energy deposited information was used to estimate sDPK

C.2 Chapter 3: Calculation of dose point kernel values for monoenergetic electrons and beta emitting radionuclides: intercomparison of Monte Carlo codes

C.2.1 EGSnrc

Table C.3 Monte Carlo methods table: EGSnrc.

S. No.	Item name	Description
1	Code, version/release date	EGSnrc-2020 release
2	Validation	Intercomparison with several MC codes in terms of DPK and electron fluence
3	Timing	1.36 to 10 hours
4	Source description	Isotropic, Monoenergetic and Point electron source with $E_0 = 50$ keV to 3 MeV Interpolated emission spectrum was utilized for several beta emitters
5	Cross-sections	Moller cross sections for $e^- - e^-$ and Bhabha cross sections for $e^- - e^+$ interactions
6	Transport parameters	BCA = EXACT algorithm; skin depth for BCA = 3 Global AP = Global PCUT = 1 keV; and Global AE = Global ECUT = 512 keV
7	VRT and/or AEIT	No VRT or AEIT
8	Scored quantities	Energy deposited in each surrounding spherical shell electron fluence for monoenergetic electron sources were also estimated
9	#histories/statistical uncertainty	$1E+07 < 1\%$
10	Statistical methods	History by history method
11	Postprocessing	Energy deposited information was used to estimate sDPK

C.3 Chapter 4: Microdosimetric calculations for radionuclides emitting β and α particles and Auger electrons

C.3.1 EGSnrc

Table C.4 Monte Carlo methods table: EGSnrc.

S. No.	Item name	Description
1	Code, version/release date	EGSnrc-2020 release
2	Validation	Intercomparison with several MC codes in terms of cellular S-value
3	Timing	5-10 minutes for β -emitters 5-10 minutes for Auger-emitters
4	Source description	isotropic, point radioactive source sampled uniformly in the source region the normalized probability distribution function is given in section 4.2.4 either emission spectrum added manually or decay of radionuclide was simulated using <i>egs_isotropic_source</i> library
5	Cross-sections	Moller cross sections for e^-e^- and Bhabha cross sections for e^-e^+ interactions
6	Transport parameters	BCA = EXACT algorithm; skin depth for BCA = 3 AE = ECUT = AP = PCUT = 1 keV
7	VRT and/or AEIT	No VRT or AEIT
8	Scored quantities	Product of mean emitted energy per decay of radionuclide and absorbed fraction of energy emitted from r_s that is absorbed in r_t Absorbed dose per activity within the r_t due to activity present in r_s (S-value)
9	#histories/statistical uncertainty	1E+07/<1%
10	Statistical methods	History by history method
11	Postprocessing	Product of mean emitted energy per decay of radionuclide and absorbed fraction of energy emitted from r_s that is absorbed in r_t was normalized with the square of the radius of the spherical shell to obtain radial energy profiles

C.3.2 Geant4-DNA

Table C.5 Monte Carlo methods table: Geant4-DNA.

S. No.	Item name	Description
1	Code, version/release date	geant4.10.05.p01
2	Validation	Intercomparison with several MC codes in terms of cellular S-value
3	Timing	3-4 hours for β -emitters 3-4 hours for Auger-emitters 1-3 days for α -emitters
4	Source description	isotropic, point radioactive source sampled uniformly in the source region the normalized probability distribution function is given in section 4.2.4 either emission spectrum added manually or decay of radionuclide was simulated using G4RadioactiveDecay() physics constructor
5	Cross-sections	uses complex dielectric response function to estimate cross-sections (see Ref. [40])
6	Transport parameters	G4EmDNAPhysics() G4RadioactiveDecay() energy cut of 7.4 eV Auger cascade and fluorescence emission enabled
7	VRT and/or AEIT	No VRT or AEIT
8	Scored quantities	Product of mean emitted energy per decay of radionuclide and absorbed fraction of energy emitted from r_s that is absorbed in r_t Absorbed dose per activity within the r_t due to activity present in r_s (S-value)
9	#histories/statistical uncertainty	β -emitters: $1E+05/<1\%$ Auger-emitters: $1E+05/<1\%$ α -emitters: $5E+04/<1\%$
10	Statistical methods	Statistical error was estimated in terms of standard deviation of the mean
11	Postprocessing	Product of mean emitted energy per decay of radionuclide and absorbed fraction of energy emitted from r_s that is absorbed in r_t was normalized with the square of the radius of the spherical shell to obtain radial energy profiles

C.4 Chapter 5: *In silico* dosimetry of low-dose rate brachytherapy using radioactive nanoparticles

C.4.1 EGSnrc

Table C.6 Monte Carlo methods table: EGSnrc.

S. No.	Item name	Description
1	Code, version/release date	EGSnrc-2020 release
2	Validation	Already validated in chapter 2, 3, and 4
3	Timing	1-2 hours
4	Source description	Isotropic, point radioactive source sampled uniformly in the source region the normalized probability distribution function is given in section 4.2.4 and the decay of radionuclide was simulated using <i>egs_isotropic_source</i> library
5	Cross-sections	Moller cross sections for e^-e^- and Bhabha cross sections for e^-e^+ interactions
6	Transport parameters	BCA = EXACT algorithm; skin depth for BCA = 3 AE = ECUT = AP = PCUT = 1 keV
7	VRT and/or AEIT	No VRT or AEIT
8	Scored quantities	Absorbed dose per activity within the r_t due to activity present in r_s (S-value)
9	#histories/statistical uncertainty	1E+07/<1%
10	Statistical methods	History by history method
11	Postprocessing	S-value was used in estimation of cell survival curves

C.4.2 MIRDcell dosimetry tool

Table C.7 MIRDcell dosimetry tool settings.

S. No.	Item name	Description
1	Code, version/release date	MIRDcell V2.1 release
2	Validation	Provided by MIRD
3	Timing	1-2 minute
4	Source description	Isotropic, point radioactive source sampled uniformly in the source region full emission spectrum of predefined MIRD radionuclides: Pd-103, Sm-153 and Au-198 was used
5	Scored quantities	Absorbed dose per activity within the r_t due to activity present in r_s (S-value)